A LOW-COST CUSTOM KNEE BRACE VIA SMARTPHONE PHOTOGRAMMETRY

Olivier Miguel

A thesis submitted to the Faculty of Graduate and Postdoctoral Studies in partial fulfillment of the requirements for the degree of

MASTER OF APPLIED SCIENCE

in Biomedical Engineering

Ottawa-Carleton Institute for Biomedical Engineering
University of Ottawa
Ottawa, Canada

January 2019

Table of Contents

List of Abbreviations

3D:	Three-Dimensional
3DP:	3-Dimensional Printing
ABS:	Acrylonitrile Butadiene Styrene
AFO:	Ankle-Foot Orthotic
AM:	Additive Manufacturing
Ant-Post:	Anterior-Posterior
BBox:	Bounding Box
CAD:	Computer Assisted Design or Canadian Dollar
CC:	Calf Cuff
DoF:	Degree of Freedom
FDM:	Fused Deposition Modelling
FO:	Foot Orthotic
HD:	Hausdorff Distance
ICR:	Instantaneous Center of Rotation
KJC:	Knee Joint Center
Med-Lat:	Medial-Lateral
MP:	Megapixels
O&P:	Orthotics & Prosthetics
PA:	Polyamide
PEEK:	Polyether Ether Ketone
PEI:	Polyetherimide
PETG:	Polyethylene Terephthalate
PLA:	Polylactic Acid
Prox-Dist:	Proximal-Distal
SLS:	Selective Laser Sintering
STL:	Stereolithography
TC:	Thigh Cuff
TPU:	Thermoplastic Polyurethane

List of Figures

List of Tables

Abstract

This thesis provided the foundational work for a low-cost three-dimensional (3D) printed custom knee brace. Specifically, the objective was to research, develop and implement a novel workflow aimed to be easy to use and available to anyone who has access to a smartphone camera and 3D printing services. The developed workflow was used to manufacture two prototypes which proved valuable in the design iterations. As a result, an improved hinge was designed which has increased mechanical strength. Additionally, a smartphone photogrammetry validation study was included which provided preliminary results on the accuracy and precision. This novel measurement method has the potential to require little training and could be disseminated through video instructions posted online. The intention is to enable the patient to collect their own "3D scan" with the help of a friend or family member, effectively removing the need to book an appointment simply for collecting custom measurements. Lastly, it would allow the clinician to focus all their time on clinically relevant design tasks such as checking alignment, fit and comfort, which could all potentially be improved by adopting such digital methods. The ultimate vision for this work is to enable manufacturing of better custom knee braces at a reduce cost which are easily accessible for low-income populations.

1 Introduction

1.1 Background/Motivation

Sports-related knee injuries are increasing and have reached an epidemic level in children [1], [2]. The knee is one of the more commonly injured joints of the body. In fact it is reported to be the most commonly injured joint for youth participating in sports [3] and is often more severe than other joint injuries of the body [4]. They typically require surgery or extensive rehabilitation before the knee joint can function at pre-injury levels. Interestingly, many are non-contact in nature, and occur during activities such as rapid decelerations and side-cuts [5]. Unfortunately, regardless of whether the patient seeks non-operative or operative rehabilitations, these injuries are associated with long-term health consequences such as the increased likelihood (up to 71%) of developing knee osteoarthritis (OA) [6]–[9] and a 12-24% chance of re-injury [10]–[13]. Together these lasting consequences result in low return to pre-injury activity levels, and ultimately reduce quality of life [6], [14].

In Canada the current protocol for pediatric knee injuries is physiotherapy and prescribing a functional knee brace. The decision of the latter is left to the physician's discretion [15]. A functional knee brace is prescribed to facilitate rehabilitation of the joint. Despite their use, the benefits associated with knee braces are still unclear [16]–[21]. Knee braces have been linked to increased hamstring and decreased quadriceps muscle activity [16], thigh muscle atrophy [17], decreased hamstring activity [22], and premature muscle fatigue [19]. A hypothesis is that the muscle impairments are a result of the brace straps creating external compression on the muscles which can decrease blood flow and result in poor oxygenation [19].

On the positive side, knee braces have been shown to 1) prevent excessive loading [20], 2) increase joint proprioception [20] and 3) improve confidence of the wearer [21]. The first is currently addressed with joint designs having a hyper-extension lock (see Types of Joint Designs). Increased proprioception or kinesthesia is helpful in preventing bad joint positions and injury [23], [24]. This kinesthesia could be enabled via increased activity of the

proprioceptive sensors around the knee (e.g. mechanoreceptors on the skin) caused by forces due to the weight, inertia and restricted motion (flexion/extension) of the brace.

Among this controversy over the effectiveness of bracing, their cost creates even more unease in their use. A custom knee brace cost approximately 1500 CAD [25]. This cost is prohibitive for many, unless it is covered partially or completely by third party insurance policies. In fact, a Canadian survey discovered that 26% of patients who received a functional knee brace prescription did not end up purchasing one [26]. The reported effects of knee braces are therefore not convincing enough for the high cost especially in pediatrics cases where the patient may require multiple braces as he/she grows.

This high cost of custom knee braces primarily comes from the custom manufacturing process. The current manufacturing models of the large knee brace companies is to mass produce in a central location [27]. This works well for prefabricated braces but is not as effective for mass customization. A decentralized manufacturing model is more flexible and effective for mass production of customized products [28], [29].

Additive manufacturing (AM) commonly known as three-dimensional printing (3DP) has enabled many businesses to adopt a decentralized manufacturing model for mass customization. The first invention was patented in 1984 [30] however it is the recent low-cost desktop 3D printers that brought AM into mainstream knowledge. Desktop 3D printers range from 200CAD – 8000CAD making this approach more accessible than ever for individuals and small businesses [31], [32].

A key advantage of AM is that it opens design possibilities. In other words, it enables design freedom. Design freedom means that any shape can now be manufactured without additional cost attributed to manufacturing complexity. This is the reason why this technology has gained attention in medicine. The promise of using 3DP in medicine is that it will enable a new level of patient-specific healthcare and as a result, it has gained attention in the prosthetics and orthotics field. What is less known however, is that 3DP of orthotic devices has been a focus of medical and rehabilitation research for more than 25 years [33]. People have created prosthetic hands, prosthetic sockets, foot orthotics, ankle-foot-orthotics and more (see Orthotics Additive Manufacturing). The projects involved the development of new methods that can manufacture medical devices at a reduce cost. Additionally, by shifting manufacturing from a manual to a digital process (i.e.: 3D printers), novel devices have the

potential for an improved fit and comfort. A leader in this space is Nia technologies which is working with three clinical partners in different developing countries to increase clinician productivity by facilitating the adoption of these new digital methods for manufacturing orthotics and prosthetics (O&P) [34]. Another, "Enabling The Future" successfully decentralized manufacturing which enabled the provision of medical devices to individuals who previously did not have access [35]. The common vision: to make medical devices more accessible and affordable. With the easy deployment of low-cost desktop 3D printers, these technologies became vastly more accessible.

AM was not the sole reason why the accessibility of these devices increased. A change in the customization process more specifically the measurement taking method was also necessary. The traditional measurement method for custom knee braces employs a measuring tape which is cheap, simple, and accurate; however, the inter- and intra-rater reliability is poor [36]. Similarly, Enabling The Future's measurement method is a series of pictures of the limb of interest with a reference scale [37]. These pictures are used to remotely measure anatomical dimensions and scale the prosthetic parametric designs, however; it is not optimal since it cannot be used for all O&P. For example, prosthetic sockets (and ankle-foot-orthotics) require the full limb geometry to create a high quality and properly functioning device. Traditionally this is achieved with the plaster and molding technique. This is a tedious and repetitive manual labour process and is not the most time effective. Fortunately, the full limb geometry can be acquired digitally with 3D scanning.

Some clinics now use high-end 3D scanners which provide an accurate and reliable way to digitize the shape of the leg [38], [39]. This approach enables higher customization and more design possibilities however; their high cost makes them inaccessible to many practitioners. More recently, there has been the development of low-cost 3D scanners like the iSense sensor (3D Systems, Rock Hill, South Carolina, United States) which uses a depth sensor mounted on an iPad (Apple, Cupertino, California, United States). These devices are more affordable and accessible and have recently been demonstrated to provide good accuracy and reliability (ICC = 0.99) [38]. However, all of these measurement methodologies are still performed by the practitioner who needs additional training to use them. The practitioner's time is too valuable. Ideally, the practitioner does not need to perform any manufacturing tasks

and instead focuses all their efforts on clinically relevant tasks such as checking alignment, fit and comfort.

There exists a method which has the potential to enable 3D scanning using only a camera and internet connection: cloud-based photogrammetry. Photogrammetry has been around since the mid 19th century [40] but with the recent technological advancements in computer vision, pattern recognition, processing power, and world-wide internet access, every camera now has the potential to be used as a 3D scanner. Additionally, video instructions could be followed requiring little training allowing anyone with a camera (i.e.: the patient) to digitize the shape of the leg. This could enable the patient to collect their own "3D scan" with the help of a friend or family member and send it wirelessly effectively removing the need to book an appointment just for collecting anatomical measurements. Ultimately, the brace could be self-fitting and fit verification could also be done via video training. Consequently, we believe that smartphone photogrammetry combined with 3DP could be a viable low-cost approach for manufacturing O&P specifically custom knee braces.

1.2 Purpose, Research Objective and Significance

The purpose of this thesis is to provide the foundational work for a low-cost 3D printed custom knee brace. Specifically, the research, development and implementation of a novel workflow aimed to be easy to use and available to anyone who has access to a smartphone camera and 3D printing services.

The objectives of this thesis are to 1) establish a workflow to manufacture a low-cost 3D printed custom knee brace targeted to pediatric populations and 2) begin the validation process of this workflow. To the best of our knowledge, there hasn't been any study investigating smartphone photogrammetry for digitizing the knee, in particular digitizing with the goal of providing a useful map for knee brace customization. Therefore, to begin the validation, the accuracy and precision (validity and reliability) of the smartphone photogrammetry method will be assessed using an accurate and reliable 3D scanner (iSense sensor) as the criterion.

This workflow is a bootstrap approach to manufacture and prototype custom knee braces. It can enable clinicians, engineers, researchers and biomechanists to manufacture

prototypes at a low-cost, as well as improve the future of custom knee brace manufacturing. A 3D printed custom knee brace can have significant impact for the pediatric population since multiple braces need to be manufactured as the patient grows (cost savings are multiplied).

1.3 Design Requirements

A possible solution to the problem detailed above was discussed with a focus group. The focus group included Dr. Daniel Benoit, who is an expert in clinical biomechanics and Dr. Sasha Carsen an orthopaedic surgeon from the Children's Hospital of Eastern Ontario. The following functional and non-functional requirements were established for the envisioned solution. The focus of this thesis was on the functional requirements. The non-functional requirements were not fully met by the current state of the development however they have guided the technology choices for the steps in the workflow.

1.3.1 Functional requirements

1. Generate 3D scan of the full leg
2. Generate a digital custom knee brace which
    a. Has a knee extension limit to prevent hyper-extension
    b. Has bilateral uprights to meet multiple knee brace categories
    c. Has a polycentric hinge to follow proper knee joint biomechanics (see Types of Joint Designs)
    d. Has a large skin contact surface to
        i. Cover EMG sensor placements for instrumentation
        ii. Provide better comfort/fit by distributing the forces over a large surface
3. Determine preliminary 3D printing parameters

1.3.2 Non-functional requirements

1. Usability

a. End user may have low expertise level and can follow an online instructional video to scan the knee and fit the brace. The brace is self-fitted.

2. Accessibility
    a. Scanning of the knee is done by anybody with a smartphone camera
    b. Use free and/or open-source software
    c. Low-cost production targeting low-income families and countries.
        i. Material cost is low by using 3D printed plastics.
        ii. The labour cost is low by automating the computer-aided design (CAD) process
    d. Initial target market is for pediatrics.
3. Scalability
    a. Global scale through a decentralized manufacturing business model
4. Reliability
    a. Output of the workflow is consistent for the same individual. Scanning method and the orthopaedic alignment are arguably the most important for assessing the reliability.
        i. Multiple 3D scans for the same leg should be consistent with a maximum Hausdorff Distance $\leq$ 2cm. Based on sizing charts for currently available custom knee brace products the smallest measurement range is 2cm [41]–[44]. Padding can be added to reduce gaps.
        ii. The feature extraction of the anatomical alignment should be consistent with a maximum error of 5mm to ensure proper hinge placement [45].
    b. The 3D printed brace can be used in high impact scenarios such as during sports

1.4 Contributions

This thesis focused on establishing the foundation of a novel approach for a low-cost 3D printed custom knee brace workflow. The functional requirements were identified and a

design which fulfills these was researched, designed and implemented. The contributions are the research, development, and implementation of

1) a smartphone photogrammetry method for digitizing the knee (see Smartphone Photogrammetry Method)
2) a computer assisted design (CAD) method for a functional knee brace (see Computer Assisted Design)
3) additive manufacturing preliminary optimal parameters (see 3D Printing Method)

Additionally, two functional prototypes were built and tested which led to the design and implementation of

4) an improved 3D printed polycentric hinge (see Prototype 1)
    a. Designed by Hilal Edrogen and Olivier Miguel.
    b. Manufactured by Olivier Miguel.
5) an EMG instrumented knee brace prototype (see Prototype 2)
    a. The electronic prototype was created by Ahmed Jaber an undergraduate student from University of Ottawa
    b. The instrumented brace prototype was designed by Olivier Miguel

Finally, to begin validating the workflow a systematic/quantitative contribution is included:

6) validation study of the smartphone photogrammetry method for digitizing the knee (see Validation Study – Smartphone Photogrammetry)

2 Literature Review

2.1 Knee Biomechanics

The knee is a six degree of freedom (DoF) joint with its primary motion being flexion/extension in the sagittal plane. It is often compared to a hinge with a constantly changing centre of rotation [46]. The instantaneous centre of rotation follows a spiral-like path [46], which is called polycentric rotation and occurs due to an anatomical phenomenon called *femoral rollback*. Femoral rollback is the rolling and sliding of the femoral condyles on the tibia plateau (Figure 25.1 in [47]). When the knee begins flexion from full extension, rolling of the femoral condyles begins with minimal sliding. As the flexion angle deepens the sliding motion increases and eventually becomes predominant [47].

The knee also undergoes axial rotation termed the *screw home* mechanism [48] where in the last few degrees of extension, the tibia externally rotates relative to the femur. This motion occurs due to the different shapes of the tibial plateau surfaces. The medial surface is slightly concave anteriorly while the lateral surface is convex also anteriorly. The concavity on the medial surface stops the rolling medial femoral condyle while the convex slope of the lateral surface allows the lateral femoral condyle to continue forward. The resulting motion is a medial rotation of the femoral shaft [49].

There are four ligaments which provide passive mechanical constraints to the six DoF knee joint: the anterior cruciate ligament (ACL), the posterior cruciate ligament (PCL), the medial collateral ligament (MCL) and the lateral collateral ligament (LCL). Accordingly, the ACL and PCL primarily restrain anterior and posterior translation of the tibia relative to the femur. The MCL and LCL primarily prevent excessive valgus and varus motion respectively [50]. As a result of these mechanical constraints, the path of the knee instantaneous centre of rotation (ICR) has been compared to a spiral in the sagittal plane [46].

2.2 Types of knee braces/Knee brace designs

Knee braces are designed to transfer loads while allowing normal knee motion. Longer knee braces can apply more leverage to the limb [51] and where the leverage is applied depends on the objective of the knee brace. A rigid brace is designed to act like a 3-point bending protection/reinforcement for the knee. The energy from a lateral impact is absorbed

by the brace into material deformation. As the elastic deformation springs back, it applies distributed forces onto the limb higher on the thigh and lower on the shank. Material deformation is largest at the load site and attachments points are the most mechanically susceptible for deformation (i.e.: hinges are the most susceptible to break) [47].

Currently there is an abundance of knee brace categories on the market; however, three main categories emerge from the literature: 1) Functional and/or Prophylactic, 2) Osteoarthritis off-loader and 3) Patellofemoral [47]. Most categories are available in soft or rigid material and custom or prefabricated designs.

The functional/prophylactic knee brace was the chosen design to demonstrate the process of a 3D printed custom knee brace. It was chosen since: 1) it is currently prescribed for pediatric sport injuries, 2) a 3D printed custom knee brace can have significant impact for the pediatric population since multiple braces need to be manufactured as the patient grows (cost savings are multiplied) and 3) the available desktop 3D printers for the project have build platforms which were too small for large thighs (e.g. osteoarthritis patients).

2.2.1 Prophylactic vs Functional Knee braces

Prophylactic knee braces are used to protect the knee from injury. Athletes playing in sports with high risk of the knee injury (i.e. football, soccer) wear them as a preventative measure [52]. The designs use polycentric hinges in a unilateral/single-hinge arrangement or bilateral uprights arrangement [47]. These apply leverage on the thigh and shank keeping the knee from excessive valgus and the MCL from overstraining [47]. If the brace is impacted on the hinge or close to the knee, the brace transfers the load away from the knee joint to a larger, more distal and proximal region on the shank and thigh (Figure 25.3 in [47]).

Functional knee braces are prescribed to stabilize a patient's knee after suffering a knee injury such as an ACL rupture. These primarily apply leverage to prevent excessive forward translation motion of the tibia relative to the femur [53]. Their effectiveness is still debated; however, past studies have shown that it can provide increased mechanical stiffness to the knee for low physiological loads [15], [54]–[59]. These braces include polycentric hinges and bilateral uprights. All functional knee brace designs can be prescribed as a prophylactic knee brace; however, not all prophylactic knee brace designs can be prescribed

as a functional knee brace [47]. Specifically, if a knee brace has bilateral uprights it can be classified as both types [47]. The commonality between the two is that they are used to assist the knee joint's ligaments: the MCL for prophylactic braces and the ACL for functional braces [47].

2.2.2 Types of Joint Designs

The hinge design is a critical component which determines if the knee brace will function properly. Excessive motion between the brace and the limb will occur if the hinge does not recreate the natural knee motion (femoral rollback and screw-home mechanism). This motion mismatch can cause discomfort and pain to the wearer. Ultimately, the hinge and knee joint should have aligned ICRs during the whole motion for optimal brace performance [60].

Simple hinge designs do not recreate the natural knee kinematics since their instantaneous centre of rotation is stationary. It has been criticized for pre-stressing ligaments and causing chronic ligamentous laxity [47]. This type of hinge was used in the past when the complexity of the knee joint's motion was not fully taken into consideration.

Bicentric hinge designs are the most common type of polycentric hinge used in knee brace [61], [62]. As the name implies it is made of two hinges instead of one, which are typically made of two segments (femoral and tibial uprights) with gear teeth at the joining ends. The ICR is located on the midpoint of the line connecting the two hinge centers which follows only the general trend of knee kinematics. For this type of hinge, proper placement mainly depends on their alignment with the femoral condyles [60].

Another type of polycentric hinge is a design that employs grooves and sliders. Examples include simple sliders and a cam stop lever [63]–[66]. More complex designs can follow a spiral-like path similar to the knee joint sagittal ICR [67]. Some designs also consider internal/external rotation of the screw-home mechanism. Examples of these are the "Asymotion" hinge from Osskin [67] which claims to reproduce "all the natural movements of the knee". If the hinge is properly customized it could also prevent excessive internal/external rotation of the knee. The disadvantage of this type of hinge is the higher cost

due to the design and manufacturing complexity as well as a challenging customization. Disadvantages that can be nullified with AM.

The last type of polycentric hinge design is the four-bar linkage. The mechanical constraints imposed by the ACL and PCL have been compared to a four-bar linkage mechanism [68]. With proper link lengths, the ICR of the four-bar linkage can theoretically perfectly follow the knee joint's ICR in the sagittal plane (Figure 2 from [69]). As a result, many knee prosthetics have a four-bar linkage joint design and more recently knee orthotics have adopted this approach for joint designs [70]–[72] since it mimics the knee kinematics more closely than the bicentric hinge. The disadvantage of this design is it resists any internal/external rotation of the tibia and femur therefore cannot follow the screw-home mechanism. This can ultimately cause more discomfort than the more complex designs which allow some degree of internal/external rotation.

2.3 Custom vs Prefabricated Knee Braces

Most knee brace manufacturers have a prefabricated and a custom option. Prefabricated knee braces are designed based on geometrical approximations of the knee, thigh and shank segments [47]. Typically, it is broken down into thickness, depth and length measurements where the thigh and shank circumferences are approximated with a semi-circular/oval curve [41]–[44]. Fabricating these braces involve less labour cost since much of the manufacturing is central and large scale therefore they are less expensive than custom knee braces [47]. The patient is required to try on multiple knee braces to see which one fits their limb the best (like a pair of shoes). The orthotist assesses the function, alignment and fit which is often only visual and subjective to the practitioner [47].

Custom knee braces are traditionally either cast molded or leg traced from a foam carving to precisely conform to the thigh, calf and knee geometry. Theoretically they can more accurately recreate normal knee motion and effectively transfer loads due to better skin contact. Their labour-intensive process makes their cost significantly higher than their prefabricated versions [47].

Many practitioners believe that custom knee braces have a better performance than the prefabricated ones. Typically, they believe it has better fit, better comfort, better joint alignment and less brace migration, however these beliefs have not been substantiated in the

scientific literature. When the geometry of the brace matches the limbs then both prefabricated and custom braces have been shown to be effective [73]. Studies which evaluated custom vs prefabricated knee braces demonstrated little to no differences showing no advantages to the more expensive option [73]–[75]. On the other hand, the level of fitness of O&P have been reported to be the most important factor for user satisfaction [76], [77]. This could be the driving reason for the greater use of custom orthotics.

The O&P community is faced with several options regarding the future of knee braces: 1) stop making custom knee braces to avoid the financial burden on patients and healthcare systems, 2) find a new method for making custom knee braces at a lower-cost or at a cost comparable to prefabricated knee braces, or 3) continue the research on custom vs prefabricated knee braces. Perhaps the confusion on custom vs prefabricated knee braces is caused by the confusion on the effectiveness of all knee braces. Due to market demands, the rising prevalence of ACL injuries and the long-term health consequences, the first option is unlikely to happen. The second option has already begun and is motivated by the use of AM of orthotics in general. AM unlocks freedom of design and could allow previously unimagined knee braces which shed a light on the effectiveness of custom knee braces. The third option will continue to exist so long as the confusion on the effectiveness of knee braces remains.

2.4 Orthotics Additive Manufacturing Evolution

This section summarizes research that has inspired the workflow developed in this thesis. It points out important/notable manufacturing approaches and how they have evolved towards additive manufacturing techniques for orthopaedic devices of the lower limb.

For lower limbs the different types of orthotic devices are foot orthoses (FO), ankle-foot orthoses (AFO), knee orthoses (KO), knee-ankle-foot orthoses (KAFO), hip orthoses (HpO) and hip-knee-ankle-foot orthoses (HKAFO). The majority of research on 3D printed orthotics was done on FO, AFO and lower limb prosthetic sockets. Since the focus of this thesis is on the development of a 3D printed custom knee brace which is a lower limb orthotic, the review will cover FO and AFO and lower limb prosthetic sockets in separate sections and an additional section will cover other notable types of 3D printed O&P such as wrist splints, prosthetic hands and prosthetic feet and ear prosthetics.

2.4.1 Knee Orthotics

There is little public information on AM of KO [78]. Online images reveal a KAFO 3DP design but not manufactured [79], a downloadable parametrized 3D printed knee brace design [80] and a case study article [81]. This shows that efforts for custom 3D printed knee braces have already begun with only one currently on the market. Osskin (Montréal, Québec, Canada) [82] is currently the only manufacturer of a 3D printed custom knee brace. Their product is targeted to osteoarthritis patients and is manufactured with a selective-laser-sintering (SLS) 3D printer. Their solution is not a low-cost approach therefore it does not meet the objectives of this thesis. However, it is a good example of how additive manufacturing can be used to improve custom knee braces.

Although there are no technical/scientific publications for AM of custom KO, the process for AM of other O&P devices is similar and can be generalized to design a KO. The manufacturing process for different custom orthotic devices has slight differences, however for any custom fabricated orthotics there are typically three main steps: 1) acquire 3D geometry of the limb, 2) device design, and 3) device manufacturing. The specifics of the three main steps for each orthotic device will be explained in each section. Each section will cover the traditional method, followed by the 3DP method and finish with examples of notable research that have used a 3DP method.

2.4.2 Foot Orthotics

There are 3 types of foot orthotics (FO) which can be prescribed: rigid, semi-rigid and soft. They are prescribed to provide additional support to the foot, correct joint alignments and foot deformities, redistribute bodyweight more evenly and improve functional characteristic of the foot [33].

2.4.2.1 Traditional Method

Soft FOs are typical made of ethylene-vinyl and manufactured using a CNC carving machine. To acquire the geometry an impression of the patient's foot is taken using a pin-

based contact digitizer machine which records the plantar surface of the foot. With CAD software specific to FO, the digitized surface is used to generate the profile of the insole. The orthotist modifies the insole before sending it to the CNC machine. For this workflow there are three key tools required: 1) a pin-based contact digitizer machine, 2) FO-specific CAD software, and 3) a CNC machine [33].

The traditional rigid and semi-rigid FO manufacturing method is to 1) create a negative mold of the foot, 2) create a positive mold of the foot, and 3) manually shape the device. The negative mold is created by placing the patient's foot into a foam box (Figure 4 in [33]). Plaster is then placed into the negative mold to make the positive mold. This positive mold is sanded and then placed on a thermoforming vacuum table. This device heats a thermoplastic sheet and creates a negative pressure difference to draw the thermoplastic on the positive mold. This creates a part/model which mimics the plantar surface of the foot. A heel block is added, extra material is removed, and the result is sanded to have a smooth finish. This workflow requires: 1) a foam box, 2) plaster, 3) a thermoforming vacuum table, and 4) tools for cutting and sanding [33].

2.4.2.2 Additive Manufacturing Method

The 3DP method for manufacturing a FO starts with 3D scanning. A 3D scanner captures either the foam box impression or the patient's foot directly. The orthotist uses an O&P CAD software to crop the region of interest and smooth the 3D scan. The edited scan is imported into another CAD software which has a "thicken" or "offset" function. This function is required to generate a solid body which mimics the foot's plantar surface. To finish the design, a heel block is created and added to the thickened body. The finished FO model is exported to a stereolithography (STL) file and imported into the 3D printer software. In this software the parameters for the print job are chosen, a file containing the printer instructions is generated and sent to the 3D printer. This workflow requires: 1) a 3D scanner, 2) CAD software, and 3) a 3D printer. There are a variety of 3D scanners and 3D printers which can be used, and this will be explained in a later section [33].

2.4.2.3 Scientific Publications

Earlier scientific publications on 3DP of FO focused their efforts on simply demonstrating a new process for making orthotics with potential for better cost-effectiveness. Their process did not focus on low-cost solutions. One study [83] performed a cost-benefit analysis for 3DP FO using fused deposition modelling (FDM) and selective laser sintering SLS 3D printers. It was estimated that the fabrication cost was £69.45/pair and £50.55/pair using FDM and SLS systems respectively while the custom FO market were selling at £50-£200/pair. Their cost analysis considered the salary of a designer and a technician as well as the depreciation cost of the 3DP system; however, it did not consider the cost of the CAD software and of the 3D scanner. The authors discuss/argue that the cost for 3DP FO can be decreased by optimizing the design for material consumption (e.g.: topology optimization, mass optimization, shape optimization). They concluded that manufacturing cost using 3DP is not expensive relative to the market norms. These cost estimates showed that using AM does not make the devices more or less expensive; however, these estimates are not for low-cost desktop 3D printers since they did not exist at the time. The study could not demonstrate the potential to significantly reduce costs with AM.

Another study [84] investigated the feasibility of a 3DP process for custom FO. Their mass customization process began with a podiatrist performing a normal clinical assessment of the patient to obtain the FO specifications (i.e.: which type of FO does the patient require). Secondly, 3D scans of the patients' feet were taken for weight and non-weight bearing conditions using a Cobra 3D scanner (Polhemus, Colchester, VT). Third, they used the Magics CAD software package (Materialise, Leuven, Belgium) to manipulate the scans and create FO designs. Then they manufactured the designs in Nylon 12 (Duraform PA, 3D Systems Europe, Hemel Hempstead, U.K.) using a Vanguard SLS 3D printer (3D Systems, Rock Hill, SC). Custom 3D printed FO were made for seven rheumatoid arthritis patients who already owned a custom FO (small sample size). Fit and comfort were measured using a 100mm visual analogue scale (VAS) as well as gait parameters (velocity, cadence, cycle time) for 3 conditions (barefoot, owned FO, 3DP FO). The results showed no significant difference for the gait measurements and for the subjective measures of fit and comfort. The study successfully demonstrated the feasibility of 3DP FO and provides a direction of future work

to explore the possibilities of improving FO designs to exploit the design freedom of 3DP (i.e. topology optimization). The study results are limited to short-term effects. The 3D scanner, the CAD software, and the 3D printer used were all expensive; therefore, a low-cost approach still is not demonstrated.

Another study [85] evaluated the discomfort and pressure distribution of 3DP custom FO. Their manufacturing process involved a 3D laser scanner (eScan 200, 3D Digital Corp, Newtown, CT, USA) to digitize the plantar surface of the participants in a non-weight bearing position. Once the 3D scanning was completed, anthropometric measurements of the foot were taken manually. The researchers failed to capture all of the dimensions using the 3D scanner because of its bulkiness and difficulty to manipulate. To design the form-fitting FO, the scans were cropped, smoothed and then thickened by 3mm using the Magics CAD software (Materialise Group, Leuven, Belgium). Final designs were manufactured in Duraform PA (3D Systems) using an SLS 3D printer. Custom FOs for six recreational runners were manufactured to investigate discomfort and pressure distribution versus a control insole. The results showed no significant differences in the VAS discomfort between the 3D printed custom FO and control insoles. The pressure mapping data showed lower forefoot and heel pressure and higher midfoot pressure for the custom FO indicating a more even distribution of weight over the foot. The authors concluded that an investigation of medium-term use of the different insoles is necessary to provide more information on discomfort. This study successfully demonstrated another method for 3DP FO which is similar to other methods. Unfortunately, this manufacturing process still is not using low-cost solutions for every step.

The same authors of [85] did an extended study [86] to evaluate the short and medium term use of custom 3D printed insoles. The manufacturing process described in [85] was used to make custom insoles for 38 runners who were recruited using the convenience sampling method. Control insoles which were not customized and manufactured using 3DP to ensure that the two different insoles were made of the same material. Three training sessions were done over the span of three months (0, 1.5 and 3 months). During the first session, participants were given either a customized FO or a control FO. They wore the same FO for the following 3-month period and only during running. The training sessions consisted of running 5 times for 10 meters while wearing shoes with the FO and with an F-Scan Mobile (Tekscan Inc, South Boston, MA, USA) in-shoe pressure sensor. Once the five runs were completed, the

pressure sensors were removed and another five runs of 10 meters was performed while recording kinematic and kinetic data using a Vicon MX system (Oxford Metrics, Oxford, UK) and 9281CA force plates (Kistler Instrumente AG, Winterhur, Switzerland). Following the training sessions, a questionnaire was completed which included the same VAS as in [85]. The results showed lower discomfort ratings for the overall fit ($p<0.05$) and the heel area ($p<0.05$) as well as lower values for ankle dorsiflexion at footstrike ($p<0.05$), maximum ankle eversion ($p<0.05$) and heel peak mean pressure ($p<0.01$) for the custom insoles indicating a potential reduction in injury risk. The custom 3DP insoles appeared to provide the sensation of foot stabilisation and good fit; however, for both insoles the arch discomfort was intrusive indicating that the material used was too rigid. The study was successful at demonstrating that custom 3D printed FO have better medium-term performance than standard (non-custom) 3D printed FO.

So far the studies mentioned [83]–[86] did not employ an AM low-cost approach. One preliminary study [87] investigated the manufacturing of custom FO using low cost 3D scanning and 3DP. Their 3DP method used a Microsoft Kinect (Microsoft Corporation, Redmond, WA) for 3D scanning, the open-source software MeshLab (Istituto di Scienza e Tecnologie dell'Informazione, Pisa, Italy) for 3D modelling and a Makerbot desktop 3D printer (Makerbot Industries, Brooklyn, NY). A custom FO was manufactured using both 3DP and the traditional plaster casting method for one 25-year-old male participant. A Vicon system (Vicon Motion Systems Ltd, Oxford, UK) with the Nexus Plug-in-Gait and Oxford Foot Model (OFM) were used to capture the 3D motion of three gait trials (10 gait cycles each). Three conditions were tested: control (running shoe), 3D printed custom FO and traditional custom FO. The Arch Height Index (AHI) was measured post data collection using the OFM and the averages of each condition were compared. The average AHI was 21.2 mm (SD 0.83 mm), 21.4 mm (SD 0.96 mm) and 22.0 mm (SD 0.84 mm) for the control, 3D printed custom FO and the traditional custom FO respectively. The study demonstrated a low-cost technique for manufacturing custom 3D printed FO and provides preliminary evidence that low-cost methods can produce orthotics with similar characteristics as the traditional method. Unfortunately, it is not a comprehensive evaluation as the study only considers the AHI while neglecting other orthotic variables such as manufacturing cost and time.

2.4.3 Ankle-Foot Orthotics

2.4.3.1 Traditional Method

According to [33], the traditional method for manufacturing AFOs is commonly referred to as the plaster molding technique. In the first step, a clinician takes measurements of the patient's ankle and foot such as length, consecutive circumferences, and mediolateral and antero-posterior dimensions. The second step is to create a negative impression made of plaster. To do this, the patient wears a long sock which covers the leg up to the tibial plateau to protect it from the plaster. Anatomical landmarks such as bony prominences and other guiding landmarks are drawn on the sock. Then, Paris bandages or fiberglass tape is wrapped around the leg to shape the negative impression. The hardening process of this mold usually takes around 45 minutes to complete during which the ankle and foot must remain in the desired position. To remove the harden mold it has to be cut or sectioned carefully to preserve the alignment and shape of the mold. The third step is to create a positive model by pouring plaster of Paris into the sealed negative impression. The fourth step is to modify the shape of the positive model by manually adding plaster to relieve known pressure points and increase comfort. This increases the tolerance at the interface of bony landmarks and areas vulnerable to pressure ulcers. Next, the positive model is sanded to create a smooth finish. The fifth step is to wrap the positive mold with a heated thermoplastic sheet to shape the orthosis. When the thermoplastic has hardened, it is trimmed to create the orthosis and the remaining sharp edges are smoothed to finish the AFO. The AFO is fitted to the patient and several gait cycles are completed to ensure that the fit and function are suitable. This manufacturing process typically takes one week to complete in an orthotics & prosthetics production facility.

2.4.3.2 Additive Manufacturing Method

The 3DP method for manufacturing an AFO uses a 3D scanner to digitally capture the geometry of the foot, ankle and leg. Sometimes a second scan is done to capture the plantar surface of the foot. The scans are imported in a CAD software where they are aligned/merged into one. Next, the scan is cropped, smoothed and thickened to create a solid body. A sketch

is drawn and used to digitally carve out the final AFO design. The design is exported to an STL file and then imported into a slicer software where the 3D printer path, print parameters and support structures are prepared before starting the print job. The last step is to remove the support structures and fit the patient [33].

2.4.3.3 Scientific Publications

A study performed in 2014 [88] evaluated the stress and strain distribution of 3D printed AFOs. They tested three AFOs customized for one 29-year-old male participant. One of the AFOs was manufactured using the traditional plaster and mold technique with polypropylene (PP) material. The other two AFOs were manufactured using a 3DP method. One was made of acrylnitrile-butadiene-styrene (ABS) and the other was made of polyetherimide (ULTEM). The 3DP method consisted of directly 3D scanning the lower leg and 3D scanning the plantar surface of the foot from the foam impression box. There is no mention of the 3D scanner model. The two separate scans were imported in Tracer CAD (Ohio Willow Wood, Mt. Sterling, OH, USA) where they were aligned, cleaned from background noise and smoothed. Trim lines were applied to shape the AFO before exporting to an STL file. The file is imported into another CAD software Magics (Materialise, Leuven, Belgium) where a thickness of 5mm was applied to generate a solid body. Sharp edges were smoothed manually before exporting the finished design to an STL file. The file was imported into the slicer software of the Fortus 900mc (Stratasys, Eden Prairie, MN, USA) FDM 3D printer. The printing time for each AFO was 23.3 hours for a completely solid build and a 0.013" layer thickness. To quantify loading on the AFOs the participant performed three consecutive walking strides three times for each AFO. All three AFOs were instrumented with three strain gauges placed on the medial malleolus, lower calf and lateral malleolus where the highest strains were expected. A finite element model (FEM) was developed to calculate the static and dynamic loading, predict stress and strain distributions and determine the rotational stiffness to demonstrate the rigidity of the AFOs. The experimentally measured strain and the FEM predicted strain were in agreement. The maximum stress (8.28MPa) occurred at 50% of the gait cycle on the inner surface of the AFO at the medial malleolus. The PP AFO had the highest strain and the ULTEM AFO had the lowest strain for all three strain gauges. This

agrees with the Young's modulus values where PP has the lowest modulus and the ULTEM has the highest modulus. This was also reflected in the rotational stiffness results where the PP had the lowest value and the ULTEM had the highest value. The FDM AFOs were shown to be stiffer and have lower strain than the traditionally manufactured PP AFO. This work demonstrated that FDM 3DP is capable of manufacturing AFOs with sufficient strength and stiffness; however, a fatigue analysis is still required. Future work should use the FEM and the experimentally measured strain for structural optimization of the AFO design to reduce the material use and fabrication time of 3DP. This would take full advantage of the 3DP design freedom which would be unmatched by traditional methods.

Another study [89] demonstrated a design and fabrication process for a custom AFO using CT scan data for optimal joint alignment. The medical imaging software Mimics (Materialise, NV, USA) was used to segment the external and skeletal anatomy digitally in 3D for one healthy participant. The segmented models were exported to Abaqus (ABAQUS Inc.) for landmarking. The AFO components (calf band, side bars and foot plate) were designed in Solidworks 2011 (Dassault Systèmes, Solidworks Corp.). The calf band and side bars were generated by trimming and thickening the 3D scan similar to previously mentioned methods. The foot plate was a generic parametrized design which used dimensions obtained from the CT scan as inputs. An Ultimaker FDM 3D printer was used to fabricate the calf band in polylactic acid (PLA) material. The foot plate and side bars were CNC machined from Aluminium alloy 6061-T6 plate and then bent using a bending machine. A gait analysis was performed where the participant walked on a force-plate instrumented walkway six times for each condition: 1) with a custom AFO, 2) with a pre-fabricated AFO, and 3) without an AFO. The results showed better range of motion for the customized AFO vs the pre-fabricated. The pre-fabricated AFO showed a smaller range of motion and higher power generation which could be attributed to greater stiffness due to misalignment [90]. Although this custom AFO was not fully 3D printed this study demonstrated an approach for manufacturing custom AFOs using skeletal structures for optimal alignment. Optimal alignment was defined as aligning the centres of rotations of the anatomical joint and the AFO mechanical joint. Joint stiffness was measured to infer on joint alignment of the different AFOs. This was done using limb anatomy fixed in a certain position, but misalignment can still occur since joint alignment is

dynamic. A methodology improvement would be to use the personalized skeletal model with motion capture data to design and align the mechanical joint.

The papers mentioned above demonstrate similar workflows for AM of orthotic devices. However, they do not demonstrate the full capability of AM to reduce cost mainly because the 3D scanners, the CAD software and the 3D printers used were not low-cost. Additionally, many of these studies mention that the costs and printing time can be reduced by applying a shape optimization step. The shape optimization is a computer approach to reduce the mass of an object optimized for a specific loading condition. To successfully compute a shape optimization, experimental data on strain and stress of a basic orthotic design is necessary similar to [88]. Although the process for AM AFO has been demonstrated, a low-cost approach has not.

2.4.4 Lower-limb prosthetic sockets

2.4.4.1 Traditional Method

Traditionally, prosthetic socket manufacturing also employs the plaster and mold technique. A prosthetist wraps the residual limb in plaster and glass fiber bandages to create the cast. At the same time palpation is used to find and mark bony landmarks and potential pressure sensitive regions. Once the plaster has hardened, it is removed from the limb and filled with plaster mud. Once the mud has set the cast is broken revealing a solid replica of the residual limb (positive mold). A faster and more modern technique and expensive uses a 3D scanner to digitize the geometry of the residual limb. The 3D scan is processed and sent to a CNC foam carving machine to create a foam model. For both method, modification of the positive model is required by adding material to the previously identified bony landmarks and sensitive areas and by removing material from the more pressure tolerant regions. This redistributes the pressure from load bearing to the more tolerant regions for better comfort. These modifications are based on the subjective evaluation and craftsmanship of the prosthetist and can change from case to case. Next, the positive model is wrapped in an oven heated plastic sheet typically polyethylene (PE), polypropylene (PP) or PP-PE copolymer. Vacuum is applied to pull the sheet tightly around the model generating the end shape of the

socket. A more expensive option is to wrap a carbon-fiber sheet around the positive model and coat it with epoxy resin. The whole is cured creating a stronger and light-weight socket for more physically active amputees. Akin to FOs and AFOs, the traditional method for socket fabrication is labour intensive and generates significant material waste as the excess is destroyed. If inevitable changes happen to the residual limb requiring another socket the whole process needs to be reiterated.

2.4.4.2 Additive Manufacturing Method

The AM process for lower-limb prosthetics is the same as FOs and AFOs. A 3D scanner is used to capture the geometry of the limb. The 3D scan is processed in CAD software to generate a surface of the region of interest. The 3D surface is thickened to generate a solid body. Modifications (trimming, variable thickness, and adding attachments for the prosthetic) to the solid body are also done in the CAD software. The end result is exported to an STL file and then imported into a slicer software where the 3D printer path, print parameters and support structures are prepared before starting the print job. The last step is to remove the support structures and fit the patient.

2.4.4.3 Scientific Publications

There are many scientific publications on the AM of prosthetic socket and the earliest was in 1991 [91]. More recent publications have evaluated the structural integrity of a double-wall polypropylene socket which showed to have good static loading strength and completed a fatigue test of 250000 cycles with no sign of failure [92]. Multiple clinical studies have shown that 3D printed sockets had similar performance as conventional sockets [93]–[95]. Studies have also shown that good comfort can be achieved [96], with similar [97] or better results [93], [98] when compared to conventional sockets. A study described a theoretical and experimental framework which incorporated a FEM step to verify the structural integrity of the socket [99]. The predicted failure strength was within 3% of the experimental results. Some publications have leveraged the design freedom of 3DP to systematically reduce contact pressure on sensitive areas by 23-45% [100] and 10-20% [101], [102] of the prosthetic sockets

using topology optimization methods. These are good examples that show how 3DP can be used to improve custom devices in a way that was not previously possible with other methods. Employing a digital framework also allows manufacturing these devices in a more controlled, systematic and data driven way which enables to improve the current designs of custom devices.

2.4.5 Other 3D Printed Assistive Devices

Other examples of 3D printed assistive device are custom wrist brace and splints [103]–[105], prosthetic hands, prosthetic feet and prosthetic ears [106], [107]. The prosthetic hands fabricated are said to be light-weight and high-strength while also being complex enough to replicate hand functions [108], [109]. The "Cyborg Beast" was developed for children with upper-limb deformities. Using a remote-fitting method this low-cost prosthetic hand was fitted on 11 children (3 to 16 years old) demonstrating its feasibility for children in LICs [110]. Prosthetic feet and ankles were also fabricated with designs specifically for 3DP. These showed that similar mechanical properties as carbon fiber feet can be obtained using a topology optimization technique [111] and that compliant ankles could alleviate the residual limb's ground reaction forces and reduce asymmetric loading of both legs [112].

2.5 Additive Manufacturing

2.5.1 Types of 3D Printing

Due to its rise in popularity, there is a lot of information available online to learn about the various types of AM and thus, only a small summary is included here [113]–[119]. The different types are 1) Fused Deposition Modeling (FDM), 2) Stereolithography (SLA), 3) Selective-Laser-Sintering (SLS), 4) Material Jetting, and 5) Binder Jetting. The types of AM which are available as desktop 3D printers are FDM, SLA and SLS. Material Jetting and Binder Jetting are currently only available as large industrial machines which are significantly more expensive. This thesis focuses on low-cost methods therefore only a summary of FDM, SLA and SLS is included. The prototypes included in this thesis were manufactured using the

Ultimaker 2+ Extended FDM 3D printer (Ultimaker, Geldermalsen, Netherlands) therefore more details are included for the FDM type.

2.5.1.1 FDM

FDM also known as Fused Filament Fabrication (FFF) is the most commonly known type of 3DP. It works by depositing melted material along a predetermined path in a layer-by-layer fashion. It falls under the material extrusion category of additive manufacturing (AM) and has the widest variety of materials. The materials used are thermoplastic polymers and include commodity thermoplastics (e.g.: PLA, ABS and more), engineering thermoplastics (e.g.: PA, TPU, PETG and more) and high-performance thermoplastics (e.g.: PEEK and PEI). High-end industrial and low-cost desktop FDM 3D printers are available on the market. The industrial machines typically include environment-controlled chambers and calibration algorithms/procedures to minimize/eliminate any deformities (i.e.: warping). They used to have higher accuracies (± 0.2mm) than the desktop counterparts; however, now desktop 3D printers exist which have similar accuracy as the industrial machines [32]. Industrial machines use to be the only ones with dual extrusion allowing for water-soluble support material; however, desktop 3D printers now include this feature as well [114]. This feature facilitates the post-processing support material removal step, which enables more complex geometries and full assemblies to be printed. For example, a full knee brace could now be printed fully assembled with water soluble support material in a dual-extruder desktop FDM 3D printer. The machine cost for industrial and desktop FDM 3D printers are 50000+ USD and 500-8000 USD respectively [116].

2.5.1.2 SLA

SLA falls under the vat polymerization 3DP category and was the first type of 3DP invented back in 1984 [30]. An ultraviolet laser beam selectively cures a liquid thermoset polymer resin layer-by-layer to create the model. It creates parts with very high accuracy (± 0.010 – 0.250 mm) [116], smooth surface finish as well as isotropic mechanical properties. The materials available are currently more brittle than what is available with FDM 3D printers therefore SLA parts are not typically used for functional purposes. Additionally, leaving the

parts exposed to excess UV light (i.e.: the sun) will have detrimental effects and make them even more brittle. The machine cost for industrial and desktop SLA 3D printers are 15000+ USD and 2000-15000 USD respectively [116].

2.5.1.3 SLS

SLS belongs to the powder bed fusion category of AM. A laser selectively sinters particles of a thermoplastic polymer or metal powder fusing them together layer-by-layer. Typically, a SLS machine can either use thermoplastic polymers or metal materials but not both. The laser required, and the temperatures needed for sintering are too different to practically combine in one machine. The SLS machine for thermoplastic polymers does not require support structures to be built since the powder bed already supports the model. The metal SLS machines require support structures to mitigate warping and distortions caused by the high melting temperatures and rapid cooling. The dimensional accuracy of metal SLS machines can reach ± 0.1mm [117] and ± 0.3 mm for the thermoplastic polymer machines. Both types of SLS are used for functional and end-product parts.

2.5.2 FDM Model Parameters

An important and often overlooked ability of AM is the large variety of model parameter choices. There exist many options and one can easily get confused on which is most important to change. For FDM 3DP, three specific parameters have emerged from online sources [113], [115], [120]–[125] as the most important/effective to alter mechanical properties of the printed model: 1) infill percentage, 2) shell thickness, and 3) orientation.

2.5.2.1 Infill

FDM 3D printed models are typically printed hollow on the inside to reduce material consumption and weight. The infill structures can have various shapes (e.g.: squares, honeycomb, lines, waves and more) which will affect the anisotropic properties of the model.

The infill percentage parameter determines how material is inside the model as well as its strength. Typically, the default setting is at 20% and provides enough strength for most applications. The highest mechanical strength of a model is achieved with 100% infill however the increase in strength diminishes as infill increases [120], [124], [125] therefore, always printing at 100% infill would be wasteful for most applications.

2.5.2.2 Shell thickness

As the name implies the shell (or wall) thickness determines the thickness of the exterior shell of the model. This can be controlled either by prescribing a thickness in millimetres or a wall line count. It is good practice to always keep the shell/wall thickness at a multiple of the nozzle diameter to avoid any gaps. Typically, this is around 1.2mm or 3 walls thick (0.4mm nozzle diameter).

Increasing the wall thickness also increases the strength of the model. From mechanics theory, most forces applied on a part can cause axial, shear and bending stress. Failures typically occurs due to the bending stress. Beam bending theory (which drives the FEM algorithms) demonstrates that the stress distribution across the beam cross-section is under tension on one side, under compression on the opposite side and in the middle there is a neutral axis along the beam where the bending stress is null [121]. Therefore, the material which contributes most to the strength of the beam is located close to the edges or walls. For 3D printed models this means that the stress is primarily distributed along the shell and secondly through the infill structure. An optimal material distribution would have a completely hollow core (no infill) with a minimal wall thickness calculated based on the stress distribution.

Previous pilot testing has shown that the shell thickness was a better parameter for increasing the strength of the model. A thicker shell had increased strength with minimal increase in the model rigidity while a higher infill percentage increased the strength with a significant increase in the rigidity of the model.

The infill structures create more connections within the model akin to cross-linked polymer chains. The shell thickness adds material following the contour of the model similarly to aligning fibers (or polymer chains). More lines of material (fibers) means a more distributed force across the lines (fibers) therefore a stronger model. This is also analogous to ligament

tissue. The stress-strain curve of ligaments has three distinct regions: 1) toe region, 2) linear region, and 3) failure region. In the toe region a strain-hardening behavior is visible and is caused by the collagen fibers being pulled and straightened in the direction of the applied force [126]. This demonstrates that when the fibers are aligned, the modulus of elasticity is higher. Therefore, depositing material aligned with the contour of the model is theoretically a better method for increasing the modulus of elasticity.

2.5.2.3 Orientation

FDM parts have anisotropic mechanical properties due to the material deposition process. When the material is deposited its high temperature slightly melts the surface of the previous layer which allows the layers to bond. This bond between layers always has lower mechanical tensile strength than the material itself. In other words, the strength of a part in the Z-axis is always weaker than its strength in the XY plane (where the XY plane defines the build plate surface). Acrylonitrile butadiene styrene (ABS) tensile test specimens have been investigate for a vertical and horizontal print orientation [122]. The vertical (Z-axis) orientation specimens had a third of the tensile strength and 5-10 times less elongation at break than the horizontal specimens (XY plane). Therefore, part orientation is an important parameter to consider and is usually the first one chosen. For a knee brace hinge the components should be printed horizontally or flat on the print bed to ensure maximal strength.

2.6 Types of 3D Scanning

Three dimensional scanners have been shown to capture highly accurate anthropometric data with less measurement error and less time when compared to the traditional measuring tape method [127]. Previous studies showed that 3D scanning is an effective method for collecting anthropometric measurements of the human body [87], [128] and could be beneficial to the design and manufacturing process in various fields [129], [130].

High-cost mobile 3D scanners were available before the low-cost 3D scanners. The prices are for the high-cost category are around 20000USD (max accuracy = 0.1 mm) and less than 1000USD (max accuracy = 0.5mm) for the low-cost 3D scanners respectively [131].

2.6.1 High-cost Scanners

The Artec Eva (Artec Group, Luxembourg, Luxembourg) is a high-end 3D scanner which has been validated for human applications [38], [39], [132]–[134]. It works with a transmitter and receiver of structured light. A study [39] evaluated the validity and reliability of the Artec Eva scanner measuring the volume, shape and size of transfemoral and transtibial residual limb models. Ten models (5 transfemoral and 5 transtibial) were scanned by three different observers on separate instances. The Romer scanner (Romer scanner, CMS108, Hexagon, UK) was used as the criterion for validation. The results showed that the Artec Eva had a mean percentage error (validity) of 1.4% of the criterion volumes and high intraclass coefficients (ICC > 0.9).

Dessery and Pallari [38] evaluated the measurement agreement between the Artec Eva 3D scanner and manual measurement with a tape measure for the surface geometry of the lower limb (knee). They scanned the dominant leg (kicking leg) of 14 healthy participants (95% CI = age 27.4 – 30.4 years, BMI: 23.0 – 27.4 kgm^{-2}). The Artec Eva showed better coefficients of repeatability than the measuring tape, and the ICC between methods was near to 1 (95% confidence interval = 0.99 - 1.0; $p<0.001$). This demonstrated that the Artec Eva is a good method to capture the 3D geometry of the lower limbs.

2.6.2 Low-cost Scanners

The same study [38] also evaluated the measurement agreement between the Artec Eva scanner and the iSense (3D Systems, Rock Hill, SC, USA) low-cost 3D scanner. The ICC between methods was 0.99 (95%CI = 0.7 – 1.0; $p<0.001$) and the Artec Eva had better coefficients of repeatability. The iSense scanner had a consistent mean bias of 13mm (0.88%) overestimating circumference measurements of the leg. This shows that although the Artec Eva is a more reliable option, the low-cost 3D scanner can be used to digitize the knee. The 13mm overestimation could be compensated when smoothing the mesh (smoothing has a shrinking effect), by finding an optimal mesh offset and by adding padding on the inside of the knee brace.

The accuracy and precision of the Xbox Kinect (Microsoft, Redmond, Washington, United States) has been evaluated for 3D scanning applications. The random error of depth measurements was shown to be less than 2mm at 0.5m distance, 2mm at 1m distance and around 4cm at a 5m distance [135]. Also when compared to the FAROLS880 laser 3D scanner, the discrepancies between the 3D point clouds was very near to zero [135]. This is the most cited study (1472 citations according to Google scholar) for referencing the accuracy of the Xbox Kinect [136]–[140]. Another study [137] compared the Xbox Kinect and the Artec 3D scanner for extracting the shape of the patella and concluded that the Kinect is an adequate substitute for expensive high resolution 3D scanner. Unfortunately, the authors did not include any values relating to the accuracy and precision for this application.

2.6.3 Photogrammetry/Structure from motion

Photogrammetry is the science of taking measurements from photos. More specifically stereophotogrammetry involves estimating 3D coordinates of points on an object using a set (2 or more) of images taken from different views. With the advancements in computer vision, we have the ability to create 3D models from 2D images (only RGB image-based 3D reconstruction).

The fundamental principle for the 3D reconstruction is triangulation. Image features (points) are extracted and matched using computer vision algorithms. For each image, a line of sight (ray) going from the camera location to the point identified on the object is constructed. The intersection of the rays determines the 3D location of the point. The 3D coordinates are then written into a point cloud (points in 3D space) which is used in surface reconstruction algorithms to generate a triangle mesh surface.

Room size photogrammetry rigs are currently used in the clothing/fashion and CGI industries to recreate realistic 3D models of human bodies. The clothing industry uses them to digitize custom fitting measurements [141], [142] and the CGI uses them to create video game characters [143], digital doubles [142] and even full 3D environments [144]. This method has good accuracy for custom clothing when compared to tailor tape circumference measurements for the arms, legs waist and chest (difference < 1cm, percentage difference = 0.97%) [141]. The cinematic industry also uses them to 3D print custom props for actors

[145]–[147]. The rigs consist of a number of high-resolution cameras (DSLR) mounted on a tower frame (Figure 1) and focused on a capture volume in the center. Each camera takes one photo simultaneously, controlled by a computer. The images are immediately sent to the computer where the 3D reconstruction processing occurs.

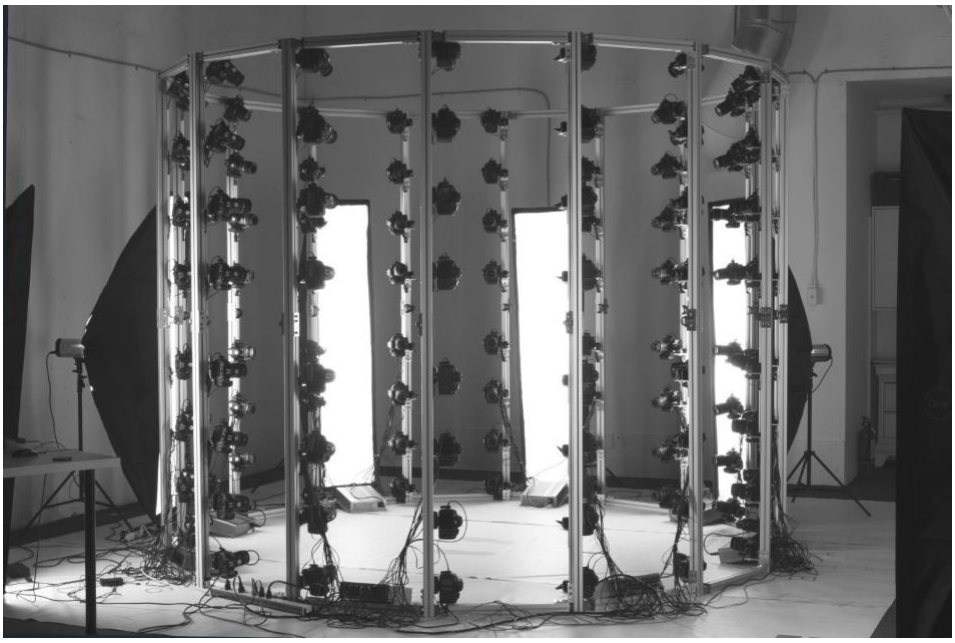

Figure 1 - Photogrammetry DSLR tower frame

Digital photogrammetry can also be done using only one camera. To do so the photographer needs to take pictures following a 360-degree path around the object. In other words, pictures all around the object are taken. The single camera method is significantly more affordable and could be possible with a smartphone camera, however there are additional considerations required. The scanned individual (object) is required to be completely immobile for the duration of the process like all other 3D scanners. Second, when using a single camera, the image features can have temporal differences. For example, if someone walks in the background the 3D reconstruction algorithm may be thrown off. Also, if changes in lighting occur, it will be reflected in the image features and distort the results. Therefore, the scene and the object both need to be unchanged for the duration of the process. Currently, the main difference between the photogrammetry rigs and smartphone photogrammetry is the camera resolution.

Smartphone camera resolution has been improving. One of the highest resolution cameras on a smartphone is 23 megapixels (MP) (ASUS ZenFone AR, ASUSTek Computer

Inc., Taipei, Taiwan). Combining this higher resolution with increasing processing power, local smartphone photogrammetry is well on its way and has already been done for android phones [148]. Many new smartphones also have dual cameras which allow for depth focus/perception and doubles their sampling rate. Photogrammetry algorithms which are optimized for dual camera could be implemented in a smartphone app and potentially have better accuracy than single camera smartphones. Also, there has been a lot of advancements in computer vision for 3D reconstruction using a dual camera set-up and this technology is now more accessible than ever [149].

There is little research studying the accuracy and precision of smartphone photogrammetry let alone for human anatomy application. Two studies were found which evaluated the accuracy of a single camera photogrammetry method for medical applications [150], [151]. One study evaluated the accuracy of a smartphone photogrammetry process versus manual tape measurements and concluded that it was a viable method for digitizing the inside of a prosthetic socket (accuracy = 2 mm) [150]. The study only had one observer perform the photo shoot, and thus no inter-rater reliability information could be provided. Inter-rater reliability is crucial information to validate that the method is consistent when used by different individuals. The other study [151] evaluated a photogrammetry process for prosthetics and orthotics on a residual limb model using a single DSLR camera (Canon EOS Rebel 500D 15.1 MP) and estimated the theoretical accuracy to be 0.05 mm. However, no measurement comparisons with a criterion method (laser scanner, high-end scanner or low-end scanner) was made, therefore the practical accuracy was not determined. A third study [136] included a preliminary evaluation of a photogrammetric approach vs a laser scanner. The photogrammetry approach used an iPhone 6S and the Photoscan software (Agisoft LLC, St. Petersburg, Russia). The average standard deviation between the two methods was around 2mm. Other publications demonstrated the use of photogrammetry in medicine and qualitatively assessed that “good 3D meshes” of the face [152]–[157], lower body [152], [158], upper body [152], [158]–[160] and ear models [152], [161] were constructed. The applications were for craniofacial surgery archives [153], [155] , dentistry planning [154], O&P [156], medical rehabilitation measurements [159]–[161] and hobbyist [156].

3 Methods - Workflow Development

The workflow developed for producing three-dimensional (3D) printed custom knee braces (Figure 2) comprises of four steps with specific outputs. First is the smartphone photogrammetry method, second is the mesh processing (i.e.: mesh/data cleanup) third is the computer-assisted-design method (CAD) and last is the AM method. Each step uses a free software available to anyone with a Wi-Fi connection and has the potential for complete automation: 1) Autodesk Recap (Autodesk, San Rafael, U.S.) which outputs the 3D digital limb geometry (mesh), 2) Blender (Blender Foundation, Amsterdam, Netherlands) which outputs the cleaned up mesh, 3) Fusion 360 (Autodesk, San Rafael, U.S.) which outputs the brace design and 4) Cura (Ultimaker, David Braam) which outputs the 3D printer instructions. The following subsections describe the development done for each step. The last subsection describes two prototypes manufactured with the workflow.

Figure 2 – Workflow. A smartphone was used for the data collection. Recap receives the data as input then outputs the cropped mesh to Blender. Blender further processes the mesh and outputs to Fusion 360. Fusion 360 outputs the custom brace design to Cura. The 3D printer instructions are generated by Cura.

3.1 Smartphone Photogrammetry Method

3.1.1 Data collection

The data collection was performed with an iPhone 6S 12MP camera, however other smartphones with similar or better camera resolution may also be appropriate. The photogrammetry process relies on image feature detection algorithms, therefore multiple influential factors need to be considered to ensure an optimal scanning procedure. The factors that were considered are number of image features, scanning pose, camera path, and lightning conditions.

3.1.1.1 Image features

The camera was set to portrait view to ensure that the entire limb of interest was captured at all times. Camera tilt and position was adjusted to maximize the size of the limb of interest in the camera view. This maximizes the limb features in the image therefore provides optimal image features.

Additionally, through the addition of image features, such as a pattern on the object of interest, the output from the photogrammetry process can be improved [150], [162]–[164]. Therefore, anatomical landmarks were identified on the participant and outlined with a marker to add more unique image features to the limb of interest (Figure 3). The following anatomical landmarks were identified and marked: fibula head, knee joint space, patella, tibial plateau, patellar tendon, and medial/lateral malleoli of the ankle. Following the electromyography (EMG) SENIAM guidelines [165] seven muscles of the lower extremity were outlined and marked with "X"s on the belly of the muscle: three quadriceps muscles (rectus femoris, vastus medialis and vastus lateralis), two hamstring muscles (bicep femoris and semitendinosis) and two shank muscles (gastrocnemius medialis and lateralis. These muscle locations were also used in digitally determining the locations of EMG sensor positions on the knee brace. These muscles were chosen because the control of the knee joint is part of their roles and current knee braces usually cover them making it harder to quantify the muscle's activations with the presence of a knee brace. Through pilot testing, it appeared that the outlined landmarks vastly

improved the 3D reconstruction of the 2D images as there were several unique features that could facilitate the feature detection between overlapping images.

3.1.1.2 Participant's scanning pose

During the initial pilot testing the standard anatomical position was used however there were complications with the resulting 3D meshes. The 3D reconstruction algorithms generated a mesh with the medial thighs merged together making it difficult to design a brace. Furthermore, the knee was fully extended when in the anatomical position and therefore insufficient geometry of knee flexion was available. To overcome these challenges, participants were asked to stand in a forward lunge with their front leg at approximately 50 of knee flexion. The participant's front foot was on a sheet of A4 paper (279mm x 216mm) taped to the floor to provide a scaling reference, and the shank was perpendicular to the ground/foot with the ankle at 90º flexion. The back leg was straight with the foot planted and externally rotated at a 45º angle in the transverse plane. Hands were placed above the hips and the hips were squared forward. The participant being scanned was asked not to move and maintain this position for the duration of the scanning process. This pose isolated the leg from the rest of the body, minimizing the merging of the medial thighs. Additionally, it enabled capturing medial/lateral alignment of the knee joint during weight-bearing conditions which is when a brace is relied upon by its user. This position is similar to the warrior pose in yoga which has been used in yoga exercise interventions for treating symptoms of osteoarthritis of the knee by training proper knee alignment and muscle strength [166], [167].

3.1.1.3 Camera path

The camera path for the video recording was determined following a fundamental engineering drawing principle: a 3D drawing of an object can be determined using only three orthogonal two-dimensional (2D) drawings. Typically, these are the front (or back), right (or left) and top (or bottom) views of the object. Therefore, the camera path captured the following sequence of views for a left leg: lateral, anterior, medial, posterior and lateral (Figure 3). For a right leg the camera path was: medial, anterior, lateral, posterior and medial. The scanner

moved to each view by slowly walking around the leg with the whole limb taking as much screen space as possible in the camera view.

Additionally, at each view, the camera's path traveled up (proximal) and down (distal), with respect to the participant's hip, to emulate the various camera positions that are present in a photogrammetry camera rig (Figure 4). A camera rig can capture a large variety of views of the real object scene at one moment in time, however it is not always accessible nor practical for a clinical setting. A single camera was used in this workflow to make it accessible to a larger population as a result it was required that the participant does not move during the recording.

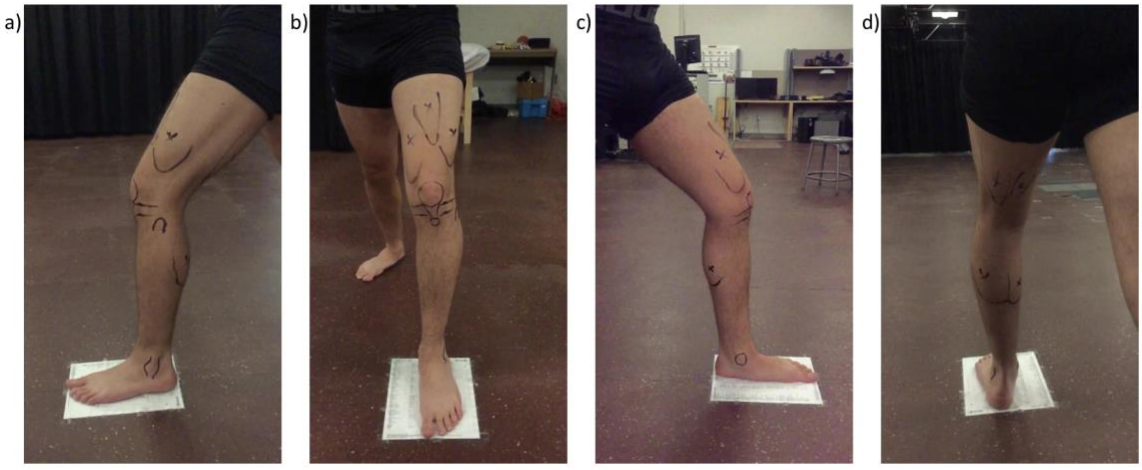

Figure 3 – a) Lateral, b) anterior, c) medial, and d) posterior views of the left lower extremity captured from the smartphone video.

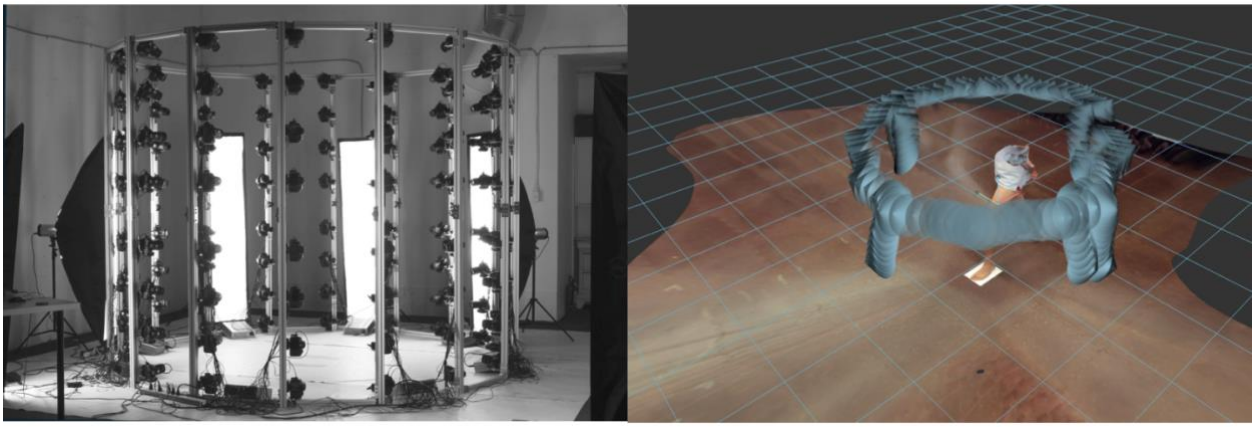

Figure 4 – Left, typical photogrammetry camera tower rig. Right, smartphone camera path chosen to emulate the camera tower rig as best as possible while ensuring optimal recordings.

3.1.1.4 Lighting conditions

Light conditions can greatly affect the quality of the generated 3D mesh. Diffused lighting, which occurs naturally outside on a cloudy day, is ideal as it creates even lighting with no contrasts or shadows however it is not always accessible for everyone. Additionally, shadows are not wanted as they hide image features which can result in distortions in the 3D mesh. The scanning was performed indoors with ceiling lights surrounding the participant from above to make the lighting as even as possible. These lighting conditions are not optimal since the posterior side of the leg contains shadows, however pilot testing revealed visually successful reconstructions.

3.2 Mesh Processing

Once the video recording was completed, Autodesk Recap was used to generate a mesh directly from the captured frames. The images were uploaded to the cloud server where the 3D reconstruction was performed. The free version of Recap was used (respecting the design requirement to use free software), limiting the number of images to 100, therefore 100 evenly distributed frames were extracted and uploaded. The finished mesh was downloaded and opened to visually confirm proper reconstruction of the leg's geometry. To determine if the overall geometry was captured the orbit and zoom view tools were used to visually inspect for mesh imperfections i.e: holes, bumps and surface deformations. Once it was determined that the overall geometry of the leg was captured the next step was to prepare the mesh for design.

The mesh was cropped to the geometry of interest: the A4 paper, the foot and as much of the test leg as possible. This was done with five plane cuts: one plane cut for each side of the A4 paper and one plane cut at the top of the thigh (Figure 5). The exact location of the thigh's plane cut was visually perpendicular to the thigh axis and immediately distal to where the femur inserts on the pelvis. The mesh was then scaled using the A4 paper as reference. The longest side of the A4 paper was measured first and then the appropriate scaling factor was applied using the scaling tool. Both sides of the A4 paper were measured to verify that the scale was correct (Figure 6). Once the mesh was properly scaled an OBJ (quads) mesh (mesh1) was exported.

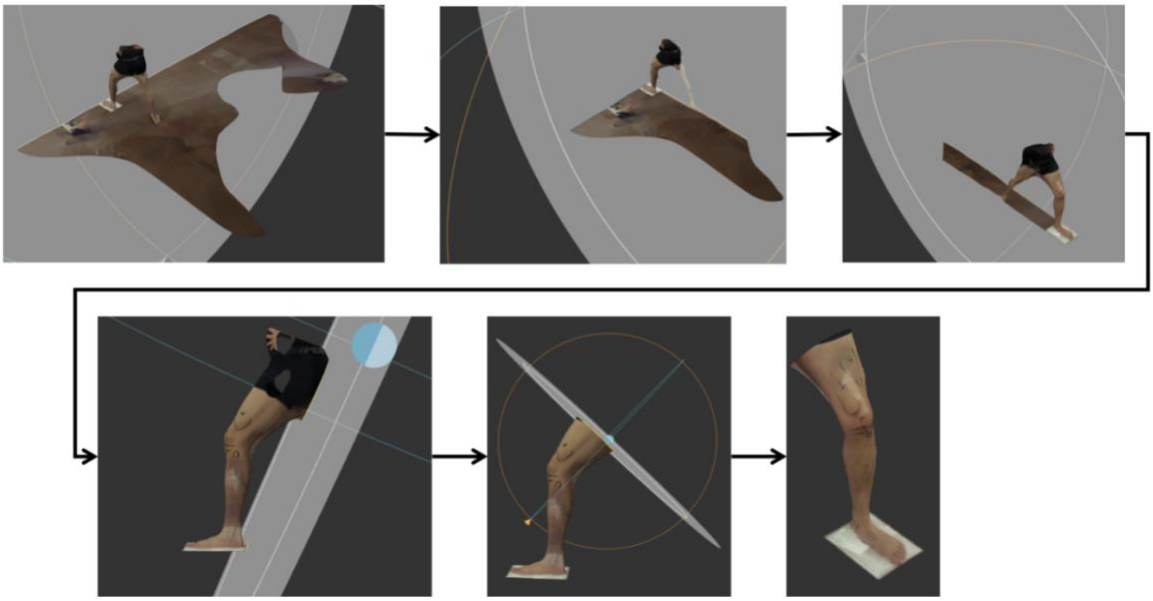

Figure 5 - Five plane cut sequence with end result. The first four are plane cuts around the A4 paper perimeter and the fifth plane cut is perpendicular to the thigh axis. The end result only contains the lower extremity of interest.

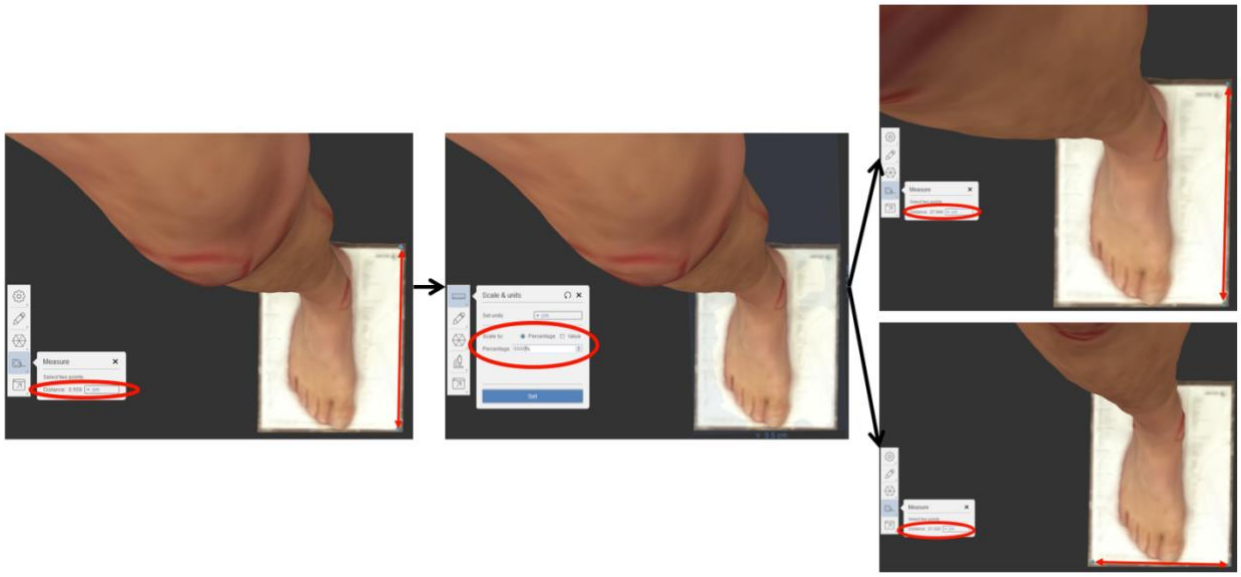

Figure 6 - Measuring, scaling and verifying the scale of the A4 paper. The first measurement, taken from the longest side of the A4 paper is 0.559 cm. It should measure 27.9 cm which is 5000% bigger. After applying a scaling factor of 5000% the long side of the A4 paper measured 27.94 cm.

The working mesh was cropped once more with a plane cut parallel to the ground and located above the medial malleoli at the smallest circumference of the shank (Figure 7). This removed the foot and A4 paper from the mesh. This mesh was exported as an OBJ (quads)

mesh and labelled mesh2 and then imported into the software Blender where a duplicate was created and used for the following steps. To reduce noise a laplacian smoothing modifier [168] was applied with the following parameters (Repeat=20, Factor=1, Border=1) (Figure 8). This modifier is a filter which reduces the noise on a mesh's surface and is necessary to use the mesh for the design of the brace. These parameters were chosen using trial and error until the mesh had a smooth looking surface (Factor=1) and borders that curved inwards (Border=1) (Figure 8). The raw mesh contained a lot of artefact which created a non-continuous surface between vertices, in other words there were "sharp/abrupt" changes in the surface gradient. If the mesh is not smoothed prior to designing, then computational issues occur in future operations (i.e.: mesh conversions and the thickening) which cause software crashes.

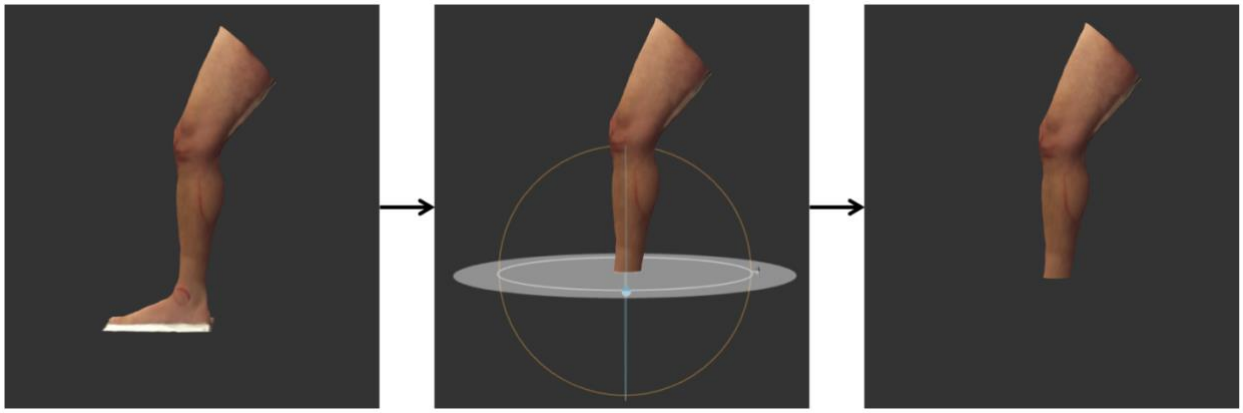

Figure 7 – Mesh1 plane cut removing A4 paper and foot to create Mesh2

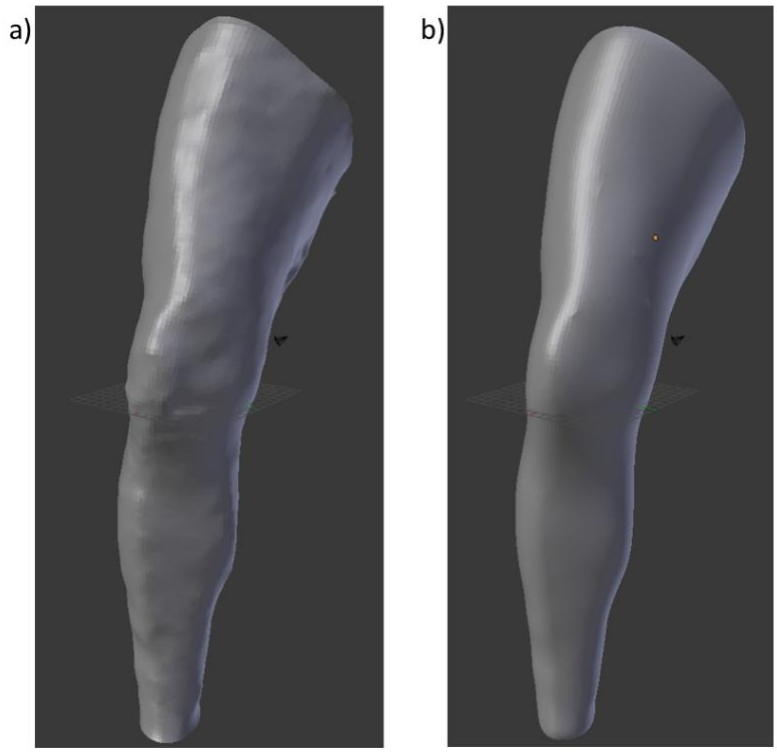

Figure 8 - a) Mesh2 before smoothing b) Mesh3 after applying a laplacian smoothing modifier

Once the mesh was smoothed it was exported as an OBJ file and labelled mesh3. It was important that mesh1, mesh2 and mesh3 are saved as OBJ files since this file type can be converted into T-Spline bodies in Fusion 360. T-spline body conversion was an important step in the Digital Alignment & Brace Cuff Design section which allowed the creation of the knee brace cuffs that follow the natural curvature of the leg. Once these three meshes were saved the next step was to start the computer assisted design (CAD) of the brace.

3.3 Computer Assisted Design Method

3.3.1 Rational for FDM 3D printed knee brace hinges

A common belief when discussing 3D printed custom knee brace with other individuals is that the hinge should be off-the-shelf, made of metal and then be assembled with the other printed components. This belief seems to be rooted by two main assumptions: 1) 3D printed hinges won't have the mechanical strength required to withstand the cyclical loading involved in knee braces resulting in early fatigue failure, and 2) off-the-shelf hinges

are not an expensive component therefore 3D printing will not provide significant advantages. This leads many individuals to believe that 3D printing the hinge is “not worth it”. Contrarily we believe that the hinge should also be 3D printed.

Firstly, materials for FDM desktop 3D printers have seen a recent surge in their variety. There are countless of materials available and many material manufacturers are creating stronger/reinforced plastics to keep up with the demand of stronger materials for end product use [169], [170]. The reality is that a 3D printed plastic polycentric knee brace hinge has never been investigated before, therefore we see this as an opportunity to contribute to the body of scientific knowledge. Testing the mechanical strength is not within the scope of this thesis, however pilot testing and prototyping revealed the potential for strong designs (see Design 1 - Simple hinge). Consequently, it was concluded that a sufficiently strong plastic knee brace hinge can be designed and manufactured using 3D printing. Design considerations for such a hinge are the anisotropic properties of 3D printed parts, layer orientation, material choice and stress concentrations.

Secondly, although the manufacturing cost may not be high, the accessibility of off-the-shelf hinges may not be as good as a 3D printed hinge for remote locations. The off-the-shelf hinges require a centralized manufacturing model which then ships them to the various locations. Shipping could add significant cost to the off-the-shelf hinge especially since some communities are very remote (Canadian North) and do not have an easy delivery method. A decentralized manufacturing business model which involves having 3D printers in multiple communities would be more appropriate.

Lastly, 3D printing can enable mass customization of not just the brace but also of the hinge itself. Knee joint biomechanics are complex and manufacturing a hinge which mimics the motion is challenging. Some knee brace hinges have groove designs (see Types of Joint Designs) which attempt to recreate this. 3D printing enables complete design freedom therefore it is perfectly suited to make both static and dynamic personalized hinges. This is not possible with off-the-shelves designs. Ultimately, a custom knee brace could be 3D printed pre-assembled with water soluble support material requiring no assembly.

3.3.2 Development of Hinge Design

For this project a generic bicentric hinge design was created to enable manufacturing of a full prototype. The bicentric hinge design was chosen because it is currently being used on existing custom knee braces. It is also improving on what is currently openly available for FDM 3D printing (see Design 1 - Simple hinge) of knee brace hinges. A custom hinge design (see Types of Joint Designs) was beyond the scope of this thesis and the focus of a future project.

3.3.2.1 Design 1 - Simple hinge

The first 3D printed hinge that was investigated was downloaded from a knee brace design on Thingiverse.com [80]. The whole brace design was printed with PLA on an Ultimaker Extended 2+. The design consisted of 10 parts that are assembled through a combination of plastic cement (or glue) and heated press-fit. The hinges included a female part and a male part. They were assembled by heating the female part (boiled water) and press-fitting the male part into it. The rest of the brace was assembled by filling the female attachments with plastic cement and pressing the male connectors together holding them in place until the cement had solidified.

The biggest disadvantage of this design is that it is a simple hinge. As mentioned earlier simple hinges should not be used in knee braces (see Types of Joint Designs). Another disadvantage was the assembly method. The brace design had a high number of parts to assemble which all require plastic cement. In general, for any assembly, the region close to attachments (screws, bolts, cement, glue etc…) are typically the first to fail under stress. Plastic cement is not a proper end-product assembly method for a knee brace since the bond failed quickly from fatigue due to the various loads. This would require much maintenance adding cost and negatively impacting the user experience.

On the other hand, the design was a good example of a strong 3D printed hinge. Although it was not mechanically tested, once assembled it was impossible to manually disassemble it. Ultimately, this design guided the choice for the dimensions of the brace cuffs and the second hinge design described below.

3.3.2.2 Design 2: Polycentric 1 – Spur Gears

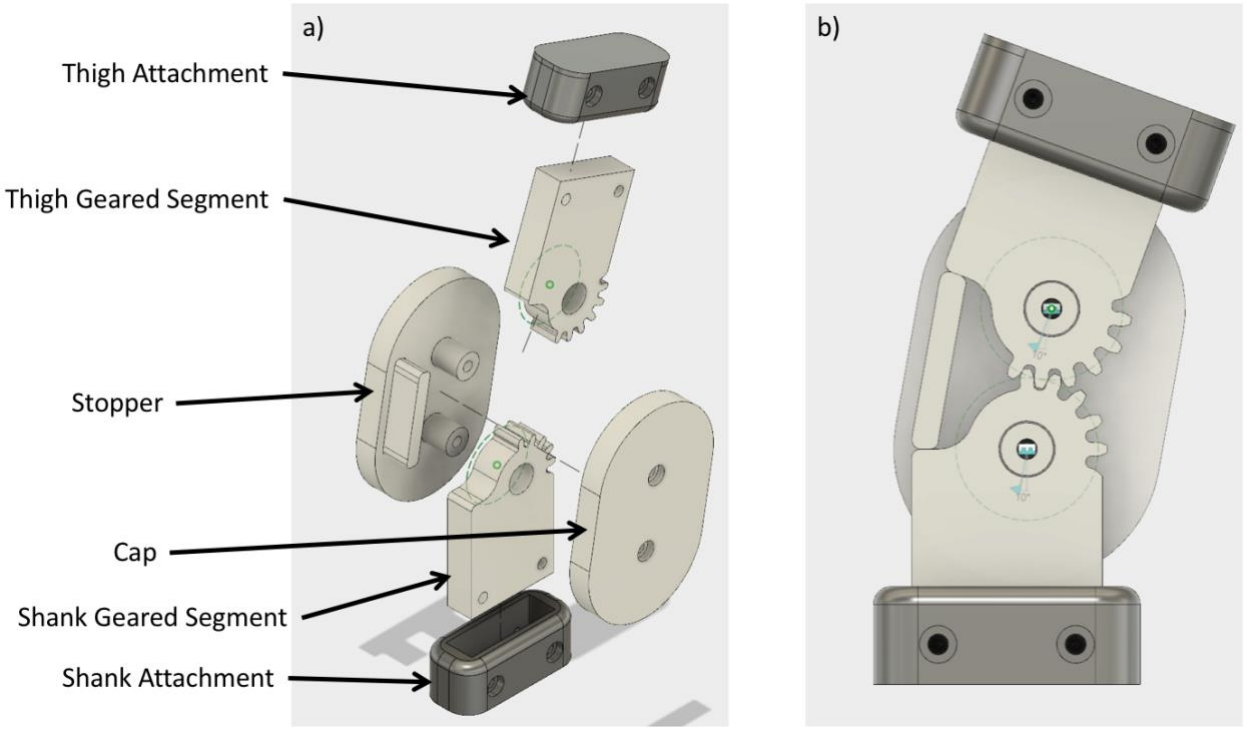

Figure 9 - a) Exploded view of the bicentric hinge design. b) Full extension side view without the Cap.

This hinge design was inspired from common knee brace bicentric hinges. The design is bicentric because its motion is described by two centers of rotations. It consists of two segments with gear teeth constrained by the "stopper" and the "cap" (Figure 9a). The stopper was designed to stop the segments 10º before reaching full extension. The geared segments connect with the brace cuffs through the "thigh attachment" and "calf attachment" parts. The attachments were merged to the brace cuffs during the lofting procedure described in the Digital Alignment & Brace Cuff Design section.

The Fusion 360 "SpurGear" Python script was used to generate the gears and their teeth (Figure 10). Once the gears were generated two "extrude" operations were used to design the segments. The first extrude was used to add the rectangular shape of the segments. The second extrude was used to cut off unnecessary teeth.

The stopper has two cylinders which hold the geared segments (Figure 9b). A pair of holes which go through the cap and the stopper cylinders were created for screws which hold all the parts together. When assembled the gear teeth are interlocking therefore one segment drives the motion of the other segment. Another four holes which go through the geared

segments and the cuff attachments were created for screws used to assemble the hinges with the brace cuffs. For this design the region close to the screws will likely be the first to fail under stress due to assembly stress concentrations [121].

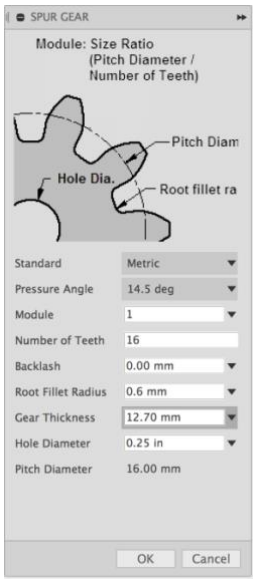

Figure 10 - Spur gear script parameters

3.3.3 Digital Alignment & Brace Cuff Design

Fusion 360 from Autodesk is a cloud-based CAD software which can manipulate mesh data and was used for the CAD procedure. The free educational version was used for the entirety of the workflow.

Mesh1 (Mesh Processing) was imported first and positioned to have the A4 paper parallel to the top plane with the top plane cutting through the ankle at a height between the lateral and medial malleoli. Mesh1's scale was validated with a 2D sketch on the top plane containing a rectangle with the A4 paper dimensions (Figure 11).

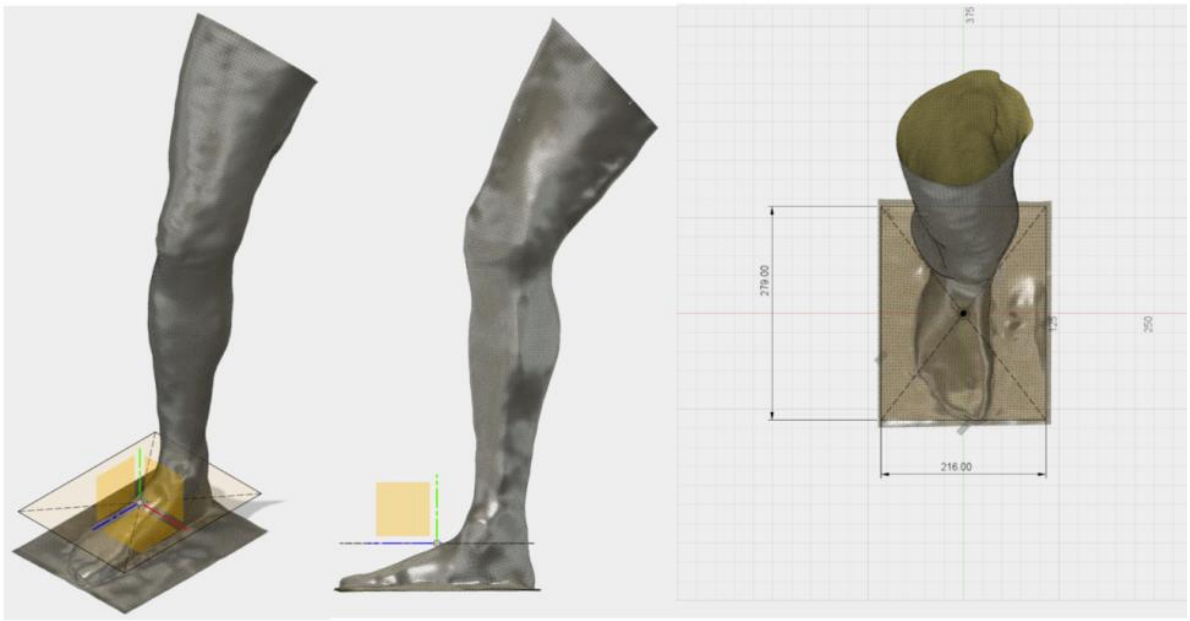

Figure 11 - Mesh1 position in Fusion 360. Left shows the origin (0,0,0) with the 3D axes (blue, red, and green), the three planes (top, front, side), the A4 paper sketch and Mesh1. Middle shows the top plane cutting through Mesh1 at the height between the lateral and medial malleolus. Right shows that Mesh1's scale matches the A4 paper dimension sketch (units are in mm).

Next, mesh3 was imported, its scale was validated with mesh1, and then was manually aligned to mesh1. Mesh3 was used to create a T-spline body (T1) by converting mesh3 from a quad mesh to a T-spline surface with the "convert" tool in the sculpt workspace of Fusion 360 (Figure 12a). The T-spline thicken tool with soft edges was used on T1 with a 3mm inward direction (Figure 12b-c). T1 was converted to a B-rep body (B1) with the "Finish Form" button (Figure 12d). Another T-spline body (T2) was generated with mesh3 and a 10mm outward direction was used for the thickening creating a solid body which was then converted into a B-rep body as well (B2).

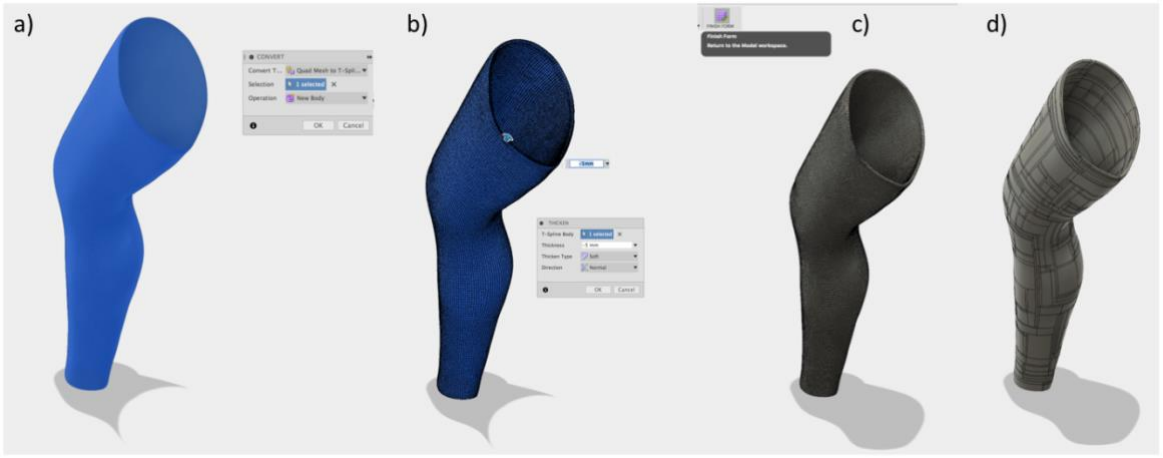

Figure 12 – a) Creation of T1 by converting mesh3 from quad mesh to T-spline surface. b) Inward thickening of T1 by 5mm with soft edges. c) Finish form button. d) Resulting body B1.

Once B1 and B2 were completed a series of 2D sketches on the left plane were created (Figure 13). The first (sketch1) was to determine the knee joint's center of rotation (Figure 13a), by drawing a 2-line segment representing the leg. The lines were positioned to visually approximate the central axis of the shank, the central axis of the thigh and the knee angle.

Before drawing the second sketch the hinges were imported and positioned. To position them the "move and rotate" tool was used. The left hinge was placed first, aligned with the point connecting the 2-line segments (i.e. knee joint's center of rotation from sagittal view) and aligned with the angle between the 2-line segment from sketch1 (Figure 14a). The left hinge was then translated as close as possible to mesh1 without touching it (Figure 14b). The "mirror" tool with the side plane (YZ) was used on the left hinge to create the right hinge. Due to the mirroring tool, the right hinge was already properly aligned with sketch1. The right hinge was translated as close as possible to mesh1 without touching mesh1 surfaces (Figure 14c).

The second sketch was used as a 2D template of the knee brace (Figure 13 b) which was depended on the first sketch and the hinge positions. The side bars in the sketch were parallel to their corresponding line segment from sketch1. They stopped before the joint center leaving a gap to properly connect them to the hinges in a subsequent step. The height of the cuffs was manually positioned to assure that it covered the EMG locations of the rectus femoris, gastrocnemius medialis and gastrocnemius lateralis. To minimize sharp edges and stress concentrations four corners on the sketch were rounded, two with 20mm radius and two

with 50mm radius. Using this final sketch2, an “extrude-include” was applied on B1 and B2 (Figure 13 c).

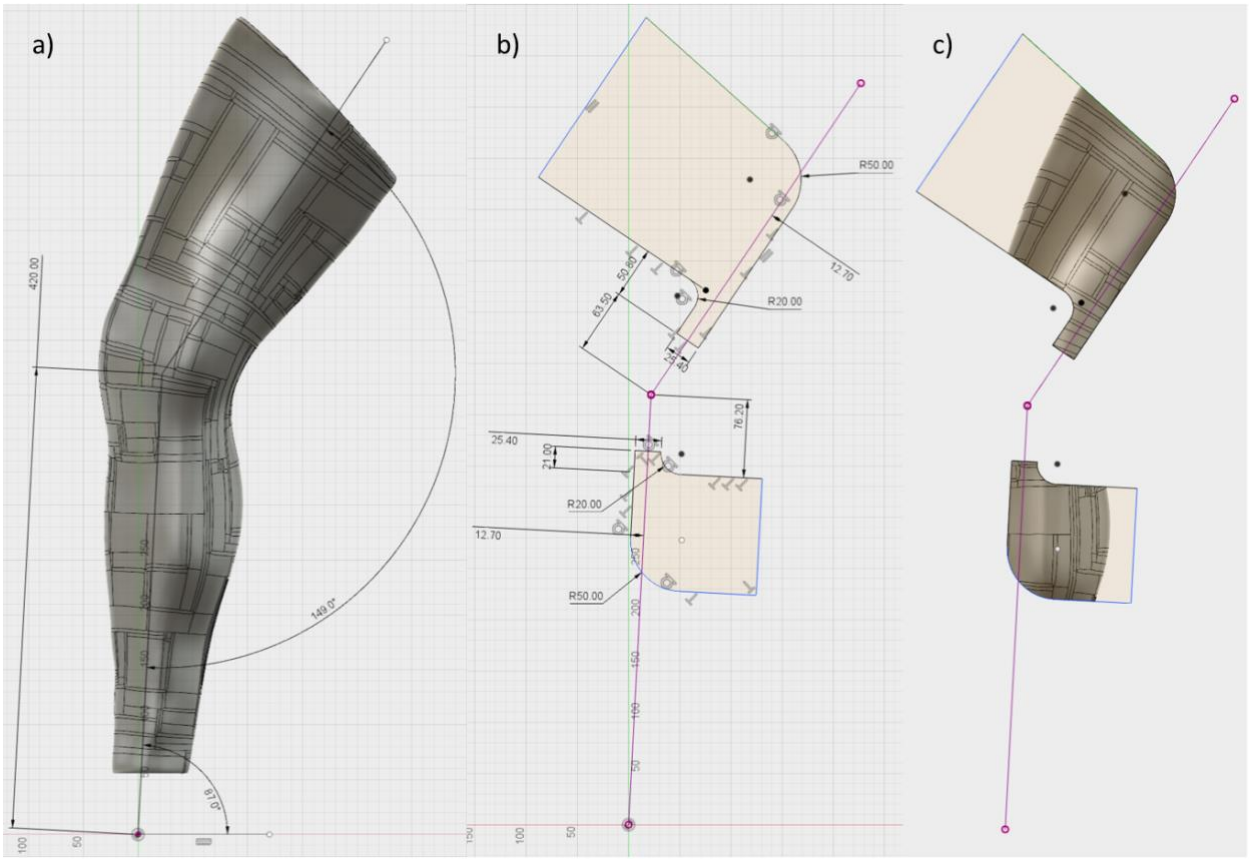

Figure 13 – a) Sketch determining the knee joint center. b) Knee brace side sketch template. c) Result of the extrude include operation. All units are in mm.

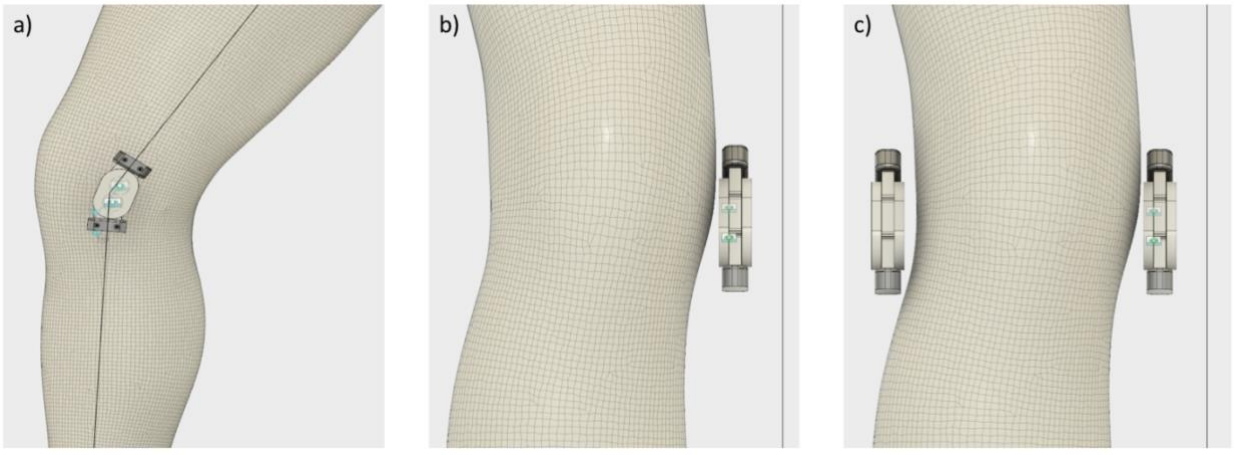

Figure 14 - a) Left hinge alignment with sketch1 line segments b) Left hinge distance from mesh1 c) Right hinge distance from mesh1

The “combine” tool was then used on the extruded bodies to join the 5mm inward thickness with the 8mm outward thickness. This created two new bodies with a 13mm thickness representing the thigh cuff (TC) and calf cuff (CC) (Figure 15a). The total thickness of 13mm was determined with an initial intuitive guesstimate of 0.5in thickness, for the brace cuffs, which was rounded up in mm. A thickness of 5mm was chosen for the inward direction to ensure that the resulting knee brace had a tight fit on the participant’s leg. A 5mm fillet radius was applied on the 4 longest edges of TC and CC to reduce sharp edges (Figure 15b).

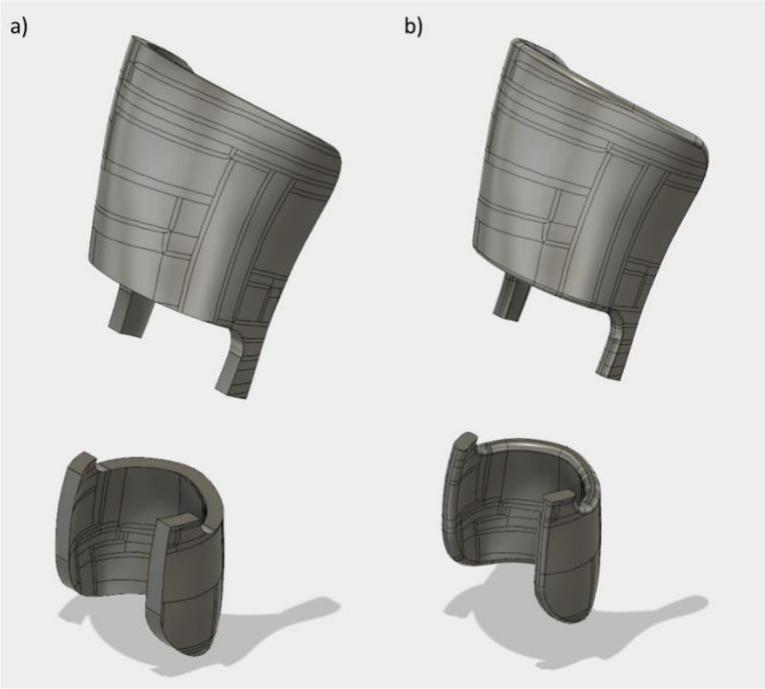

Figure 15 – a) Thigh cuff (top) and calf cuff (bottom) before fillets. b) After fillets

Four lofts on eight faces with guide curves were used to connect TC and CC to the hinge attachments. The guide curves were created in a 3D sketch with three lines per curve and 5mm fillet corners to minimize sharp edges (Figure 16). The four lofts created four new bodies, two of them were joined with the thigh cuff and the other two with the calf cuff (Figure 17).

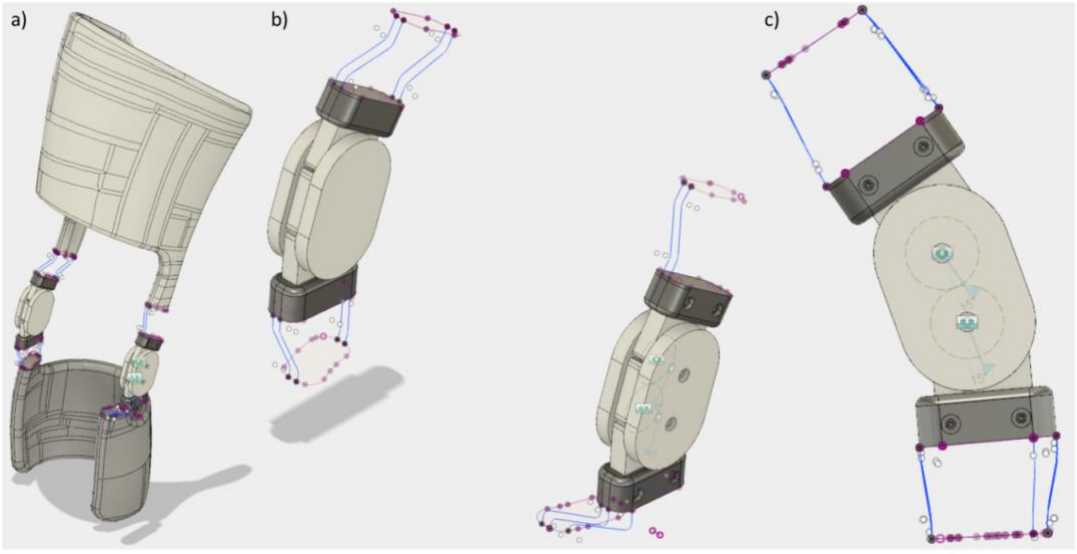

Figure 16 - Eight faces used to make the four lofts are outlined in magenta and the 3D sketch guide curves are in blue.

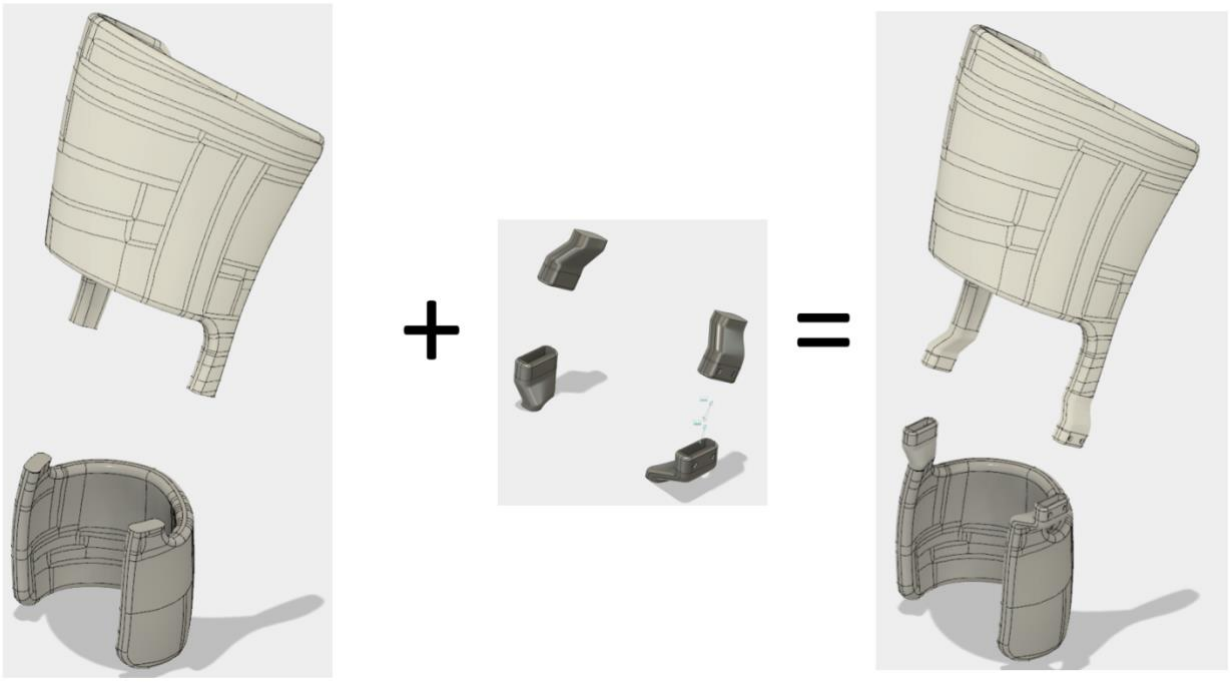

Figure 17 – Brace cuffs combined with the 4 bodies created by the lofts gives the cuffs with complete sidebars

After the cuffs were completed, the slots needed to attach the straps were created. A side sketch was created, and the outline of the knee brace template was included. The slots were 5mm wide and 35mm long. They were oriented parallel to the line segments (sketch1) and positioned 7mm from the edge of the template (Figure 18). The “extrude-cut” tool was used on the slot sketch creating the slots in the cuffs.

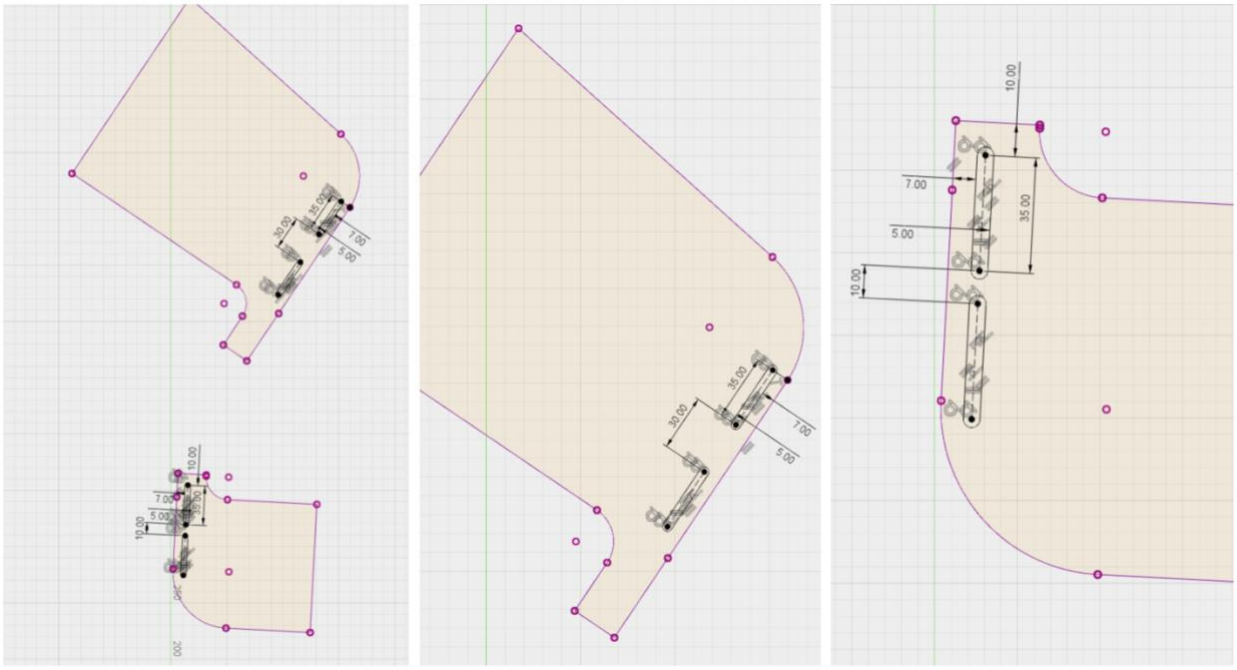

Figure 18 - Side sketch of slot holes. All dimensions are in mm.

Next, holes in the cuffs needed to be cut out at the EMG sensor locations in accordance with the SENIAM guidelines [165]. The rectus femoris EMG was located at 50% on the line from the anterior spina iliaca superior of the pelvis to the superior aspect of the patella. The gastrocnemius medialis EMG was placed on the most prominent bulge of the muscle. The gastrocnemius lateralis EMG was placed at 1/3 of the line between the head of the fibula and the calcaneus. For the thigh cuff, there was only one hole created for the rectus femoris quadriceps muscle. A plane was created using the "Plane at Angle" tool on the thigh line segment (sketch1) with an angle of 0º. A sketch was created on the plane, and a rectangle was drawn. The rectangle dimensions were based on the size of wireless, bipolar surface EMG electrodes (16-channel Trigno, Delsys, Boston, USA). Sketch fillets (10mm radius) were created on the rectangle's corners to minimize sharp edges. The "extrude-cut" tool was used on the sketch to create a hole (Figure 19). For the calf cuff one hole for each gastrocnemius muscle belly was created. To create the gastrocnemius holes, the shank segment line was projected on the side plane. Then the "Plane at Angle" tool was used on the projected line to create two planes. An angle of -30º was used for the gastrocnemius medialis plane and an

angle of 45º was used for the gastrocnemius lateralis plane. These plane angles guide the hole's sketch cutting directions and were determined visually by trial and error. A rectangle sketch with corner fillets was created on each plane. The "extrude-cut" tool was used on the sketches to cut through the calf cuff and create the holes (Figure 20).

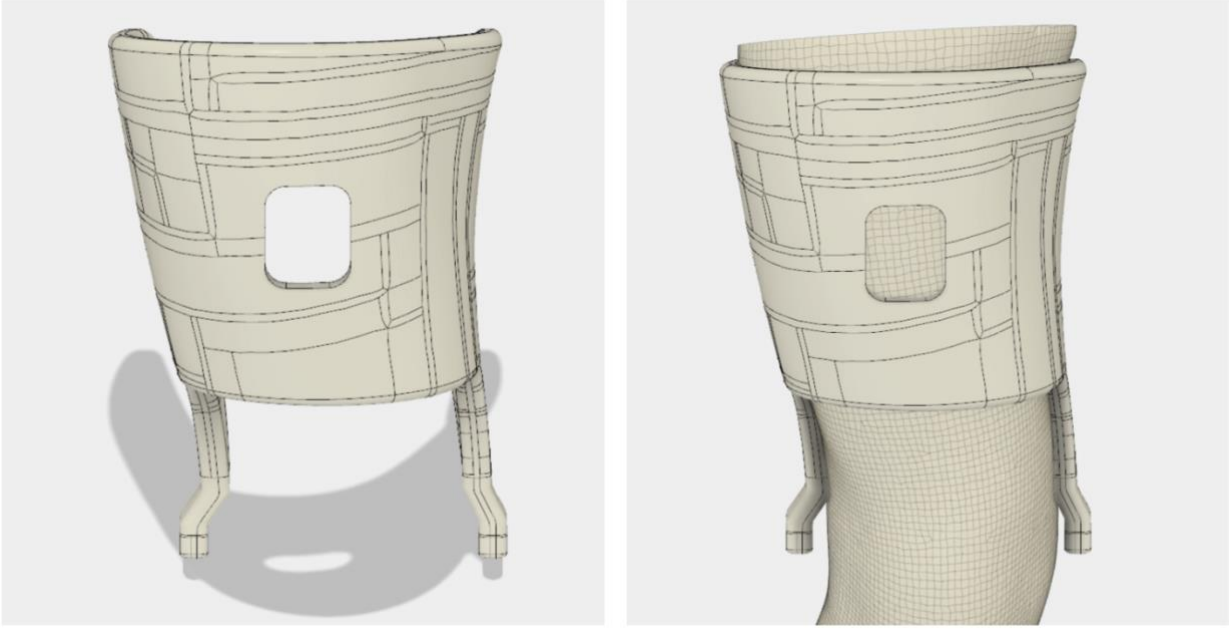

Figure 19 - Rectus femoris EMG hole

Figure 20 - Gastrocnemius medialis and lateralis EMG holes

Once the necessary holes were created the finishing step was to fillet all remaining sharp corners and edges. For the strap slots, a 2mm edge fillet was used. For the sensor holes edge fillets of 5mm were used. Once the last fillets were completed the brace cuffs were ready to be printed (Figure 21).

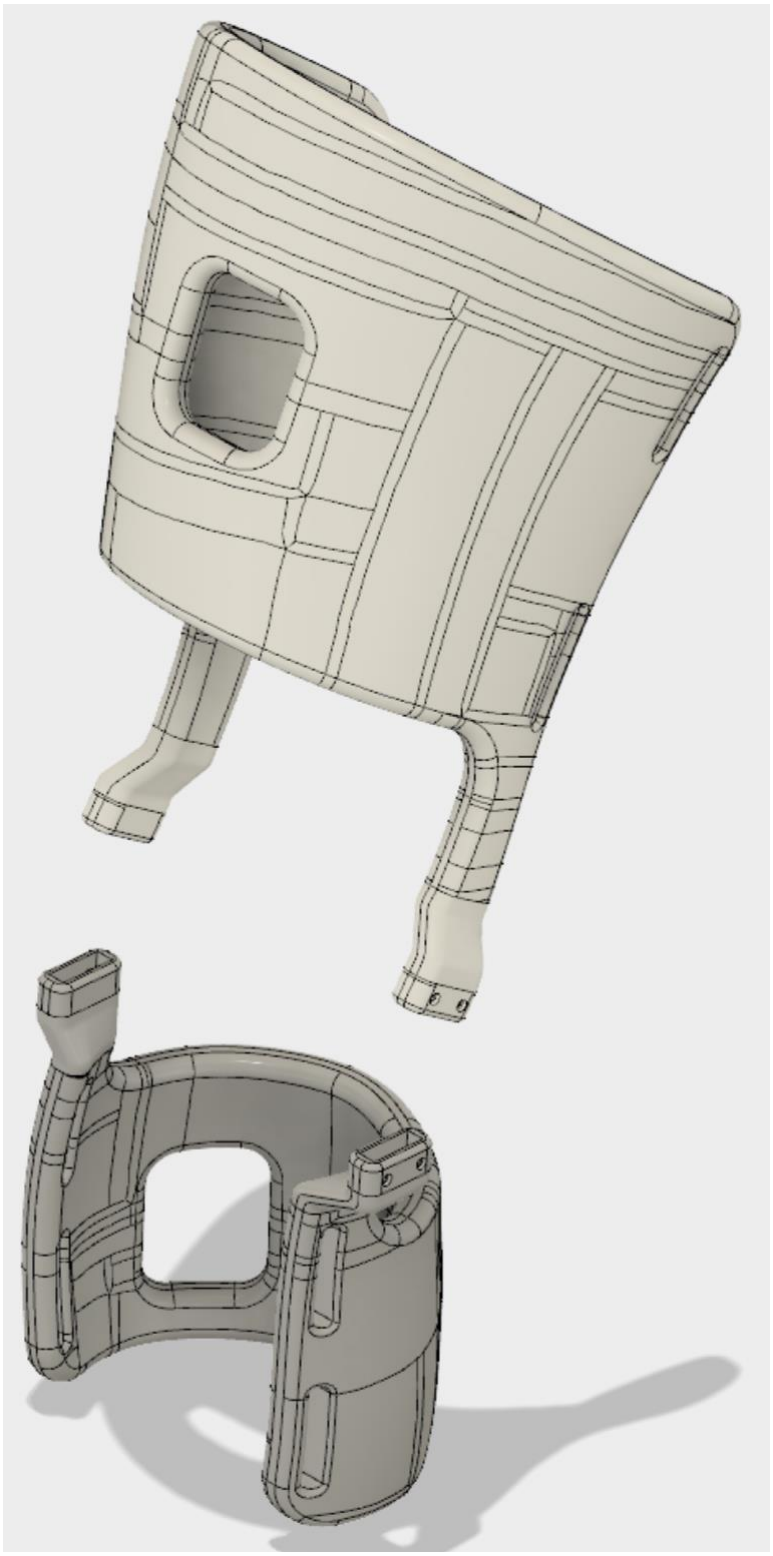

Figure 21 - Brace cuffs ready for additive manufacturing

3.4 3D Printing Method

Once the knee brace design was completed the parts were exported as STL files. An Ultimaker Extended 2+ was used for 3D printing and the Cura software generated the GCODE file. As the current knee brace design cannot be printed in one print job, there were four separate print jobs to print the full brace. There was one print job for each hinge (right and left), one for the TC and one for the CC. For each print job the STL files were imported into the Cura software.

3.4.1 Orientation

The TC and CC were oriented to have the side bars pointing up and the bottom face flat on the printer bed (Figure 22). To print the hinges, one STL file for each part was imported and all the parts were oriented flat on the bed with the smallest bounding box dimension in the Z direction (Figure 23).

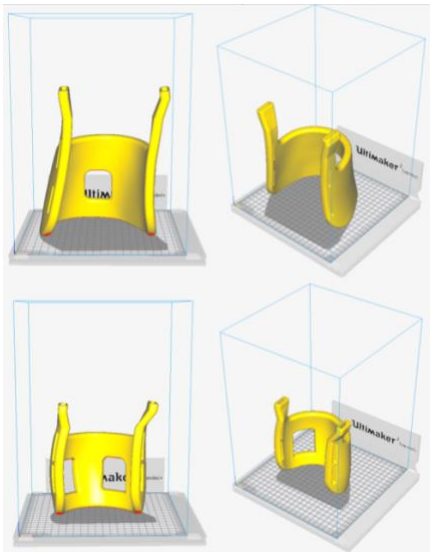

Figure 22 - Top, thigh cuff orientation. Bottom, calf cuff orientation

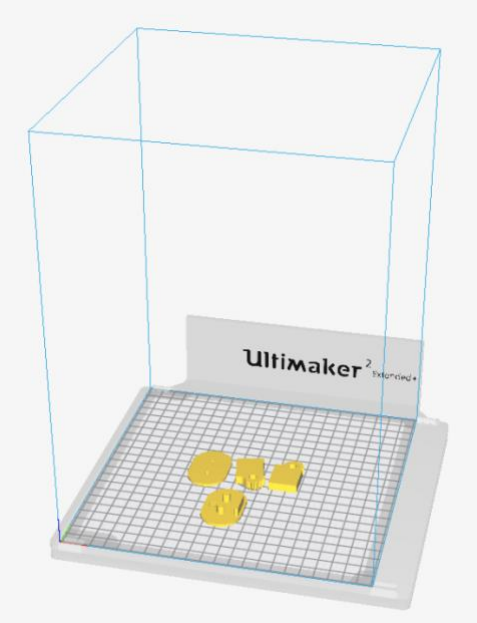

Figure 23 - Right hinge print orientation

These orientations minimized the use of support material. For the hinges, this orientation also corresponded to the layer orientation which should produce the strongest gear teeth profile (primary axis of anisotropy). Due to size constraints, the TC and CC print layer orientation was not optimal for mechanical strength. The layers are close to their weakest orientation to resist bending stress on the sidebars. To account for this deficit other parameters were changed.

3.4.2 Printing Parameters

All parts had the following parameter settings: wall thickness of 3.2mm, top/bottom thickness of 2mm, and a layer height of 0.1mm. The hinges were printed with a 100% infill parameter. TC and CC were printed with a 90% 5-step gradual infill. The gradual infill is implemented for high infill density in the side bars and low infill density in the band section. All other parameters were left at default. The wall and top/bottom thickness were higher than default settings to increase the strength of the model. The infill parameters were higher to increase the rigidity of the model. The 2nd smallest layer height was selected because the smallest one (0.06mm) increased printing times impractically.

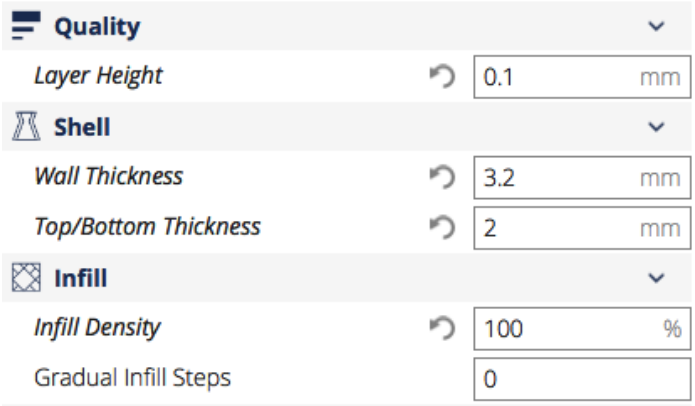

Figure 24 – Cura hinge print job parameter settings

The printed parts were removed once printing was completed and the printer bed was cooled. The support structures were broken off with pliers. If small sharp edges remained after removing the support structures, a file was used to smooth out any remaining sharp edges.

3.4.3 Material

The material used for the functional prototypes was a reinforced polylactic acid (PLA) plastic named APLA+ [171]. It was chosen because it was advertised as having higher impact and tensile strength than ABS making it appropriate for functional prototyping.

3.4.4 Assembly

To assemble the brace 12 screws (Phillips Rounded Head Thread-Forming Screws for Plastic, 18-8 Stainless Steel, Number 0 Size, ¼" Long) were used. Each hinge required two screws for assembly and another four screws per hinge were required to assemble the hinges with the cuffs. Small holes in the design marked the location for the screws as described in a previous section (see Design 2: Polycentric 1 – Spur Gears). Velcro brace straps were then added to the 3D printed knee brace. The fitting of the knee brace was done by simply placing the brace on the leg, with the curvature of the cuffs making the fitting intuitive. However, it is important to check that the hinges do not restrain proper movement of the leg. A few sitting

knee flexion/extensions cycles and gait cycles were done with the brace on to confirm that the fit is proper.

3.5 Prototyping

Custom functional prototypes were manufactured for 2 participants: 1) (age 46, weight 82kg, height 180cm) and 2) a female (age 24, weight 53.5kg, height 163cm). For the male and female participants total print time and material costs were 142hrs38mins, 37.61 CAD and 107hrs50mins, 31.00 CAD respectively. The participants were asked to self-fit their custom brace. Minor fitting adjustments were required based on verbal feedback on comfort and skin pressure.

3.5.1 Prototype 1

The male participant wore the brace over pants for a full day with no reported discomfort or skin irritation. Unfortunately, the thigh cuff was not properly staying in place. During full extensions, the superior region of the thigh cuff was falling anteriorly creating a gap between the thigh and the brace. The weight of the thigh cuff was not held properly because the top strap was placed too low on the thigh cuff which allowed it to fall anteriorly. To correct this design flaw, the top strap hole needed to move superiorly. This change was implemented in the second prototype (female) and as a result, the second prototype did not fall anteriorly and stayed in place properly.

Another prototype experiment was performed by designing the first prototype custom brace with a mechanical handicap; the hinges were positioned at different frontal plane angles. This misalignment put the mechanism under higher (tension, bending, shear, torsion) loads resulting in an accelerated failure (fatigue). This eventually (~6 months) revealed mechanical weaknesses of the printed hinge. The first signs of failure were noted at 1 month. After ~100 cycles (one full day + intermittently/sporadically up to 3 months) of wearing, subsequent flex/ext cycles were applied by hand on the prototype. The manual cycles consisted of swinging the thigh cuff to swing the shank cuff in a pendulum motion. The shank cuff swung until impact with the hinge occurred at the flex/ext brace limit (10 degrees from full extension). These cycles started with low intensity and increased until complete mechanical

failure occurred (>1000 cycles). The hinge design failed before any apparent damage to the cuffs occurred. The failure happened on the stopper at the base of the cylindrical pin and appears to be caused by bending stress (fatigue). The misalignment caused frontal plane bending and the thread forming screws caused assembly pretension. The printed layers were pulled apart by the pre-tension and bending stress which accelerated the failure.

To fix the design flaws discussed above, another hinge was designed which incorporated self-locking snap-fit features [172] removing the need for thread forming screws. An undergraduate student (Hilal Erdogan; Faculty of Engineering, University of Copenhagen) was tasked to create it and implemented another improvement (idea originating from Dr. Daniel Benoit) which was to change to a herringbone gear design. It was hypothesized that it would make the assembled hinge stronger by distributing the frontal and transverse bending stress to the gear teeth.

The same Ultimaker Extended 2+ desktop 3D printer with the same thermoplastic material (3D Printing Method) was used to print the parts. Print time and material cost were 8hrs41mins and 2 CAD. Thermoplastic material softens with temperature therefore the hinges were placed in hot water to facilitate the snap fit assembly (reduce assembly forces). A possible positive effect of the water heating process is a reheating of the layers which can create a better bond between the printed layers therefore improving the mechanical strength/behavior of the parts (i.e.: the plastic is annealed with hot water) [169]. The assembled hinge was then cooled in room temperature which takes about 2mins. After assembly these hinges were placed under manual bending load (Figure 25). Several individuals from inside and outside of the lab were asked to break the hinge using the manual bending method (Figure 25) and none were successful. Mechanical bending tests with a material testing machine (i.e.: Instron) are needed to better assess the mechanical strength of this new and improved design.

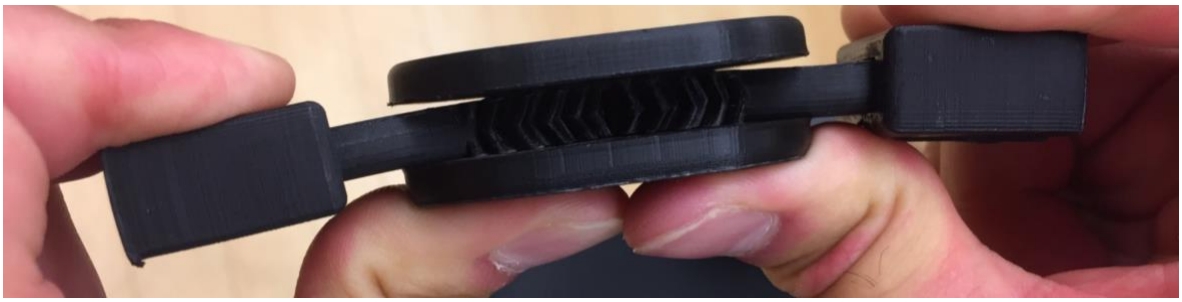

Figure 25 - Manual bending method. Thumbs are placed in the center of the hinge and the hands are pulling down on the ends of the geared segments

3.5.2 Prototype 2

The custom brace for the female participant was designed with hinges properly aligned and was instrumented with EMG sensors. An electronic prototype was created by an undergraduate coop student (Ahmed Jaber) and comprised a processor (Lilypad, Arduino), Bluetooth module (Bluetooth HM-10), EMG (MyoWare Muscle Sensor, SparkFun, Electronics, Boulder, Colorado, United States) and breadboard. 3D printed cases were made to encase the electronic prototype and attach it to the brace. The bottom of the EMG case was merged in the cuff designs (Figure 26) using Fusion 360 CAD software. This step added complexity to the design however it was necessary for the EMG sensors to be in contact with skin and encased in the brace. The coop student also developed an android app to collect data from the prototype. The electronic prototype was first tested on a bicep brachii confirming the app successfully receives data (Figure 27). Data collections with the instrumented knee brace prototype were attempted but unsuccessful. The collected signal was a flat line therefore connection issues occurred. The EMG electrodes seemed to be placed under tension and shear forces by the brace which was moving relative to the muscles during contractions. This could have caused poor contact between the electrodes (stuck on the skin) and the EMG hardware (encased in the brace), preventing it from measuring a proper signal. A different EMG case design could fix this problem.

Figure 26 - Computer assisted-design of Prototype 2. The EMG sensor case is merged with the brace cuffs.

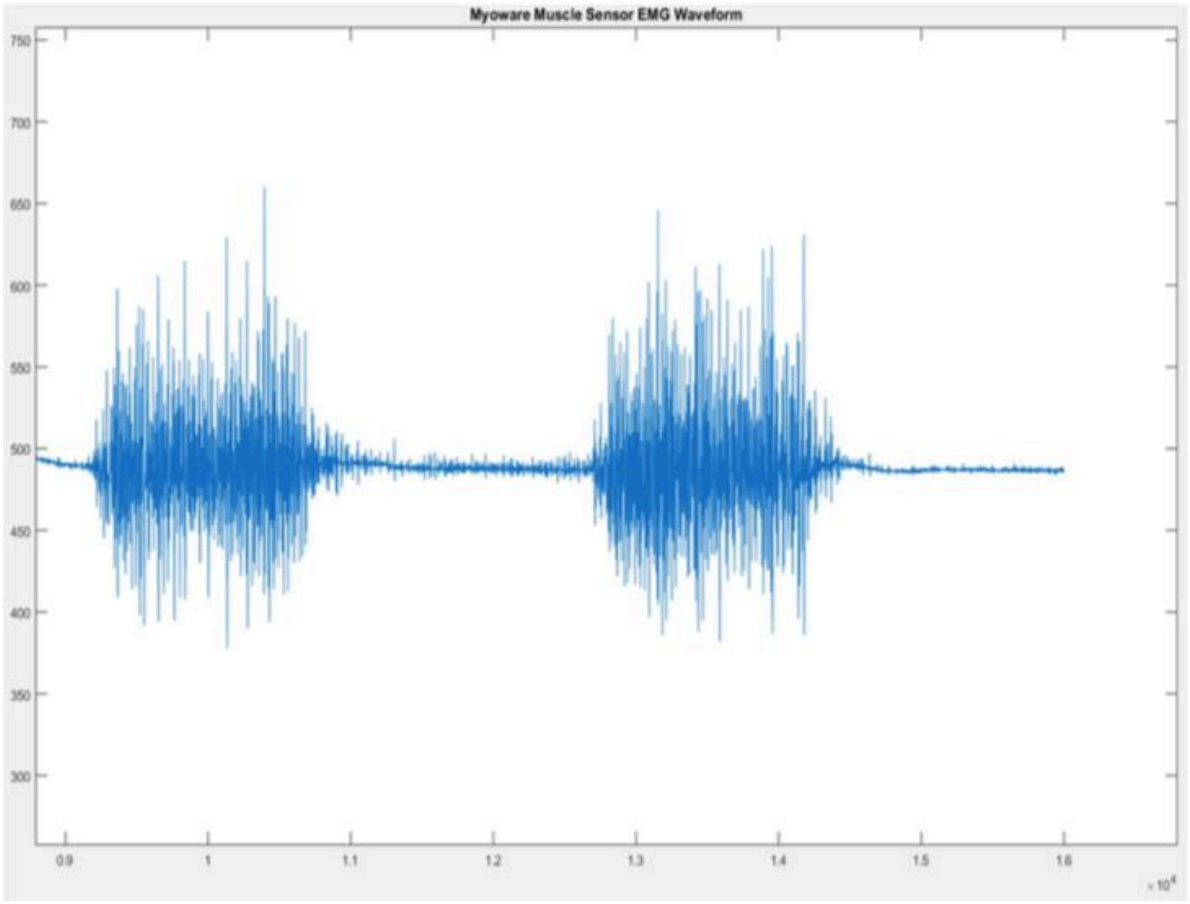

Figure 27 - Bicep brachii muscle EMG signals collected with the electronic prototype.

4 Validation Study – Smartphone Photogrammetry

4.1 Methods

4.1.1 Experimental Design and Data Collection

Two males (age: [26, 25], weight: [70, 118] kg, height: [175, 208] cm, BMI: [22.9, 27.3]) and two females (age: [21, 24], weight: [50, 53] kg, height: [163, 163] cm, BMI: [18.8, 19.9]) who previously suffered a knee injury were recruited via convenience sampling method (male 2 and female 2 were ACL injuries). The participants were chosen to represent the demographic of young adult athletes who suffered from sport-related knee injuries across a large range of body sizes (BMI: 18.8 – 27.3).

Before scanning, four clusters of three plastic coins were placed on the limb of interest; one distal cluster and one proximal cluster for both the thigh and the shank (Figure 28). Each cluster defined a plane used to facilitate precise cropping of the 3D scans. The proximal thigh cluster consisted of three coins placed on the anterior, medial and lateral proximal regions of the thigh at 20% of the thigh length (greater trochanter to distal lateral femoral condyle). The distal thigh cluster consisted of two coins on the femoral epicondyle landmarks and one marker on the patella. The proximal shank cluster consists of coins on the fibula head and anterior and medial tibia plateau landmarks. The distal shank cluster consists of two markers on the lateral and medial malleoli and one above the heel on the Achilles tendon.

Scans of the injured legs were created using two methods. The first method used the low-cost 3D scanner (iSense; criterion) and the second used the developed smartphone photogrammetry procedure. An iPhone 6S was used which has a 12 mega-pixel (MP) camera. Three researchers (observers/raters), were graduate students from the University of Ottawa, were trained to perform the data collection. The individual training consisted of three practice scans with instructions and feedback with corrections for each researcher. Each participant was scanned during separate sessions. Each researcher performed three scans of each participant with each device. This resulted in 18 scans per session for a total of 72 scans (4 participants x 3 researchers x 3 repetitions x 2 devices). The researcher sequence and the device sequence were performed in a randomised order with minimal break between each scan.

Figure 28 – Frame extracted from the video recording. Plastic coins on the leg were used to aid in mesh reconstruction and processing

4.1.2 Data Processing

The 3D scans we're manually cropped using Autodesk Recap (see Mesh Processing). The proximal and distal plane used for cropping passed by the edges of the three markers in their respective cluster (Figure 29). Next, the 3D mesh was transformed into a 3D body by closing all remaining holes. The resulting body was exported as a PLY file which was then imported into the open source software MeshLab (Istituto di Scienza e Tecnologie

dell'Informazione, Pisa, Italy). All the scans from one participant were imported into one Meshlab project and were aligned with the rigid point cloud registration filter before extracting measurements.

Figure 29 – Cropped leg showing the proximal (thigh) and distal (ankle) clusters used for cropping.

The following measurements were extracted for all scans: Hausdorff Distances between each pair of repeated scans, total limb volume, limb bounding box size (BBox), knee joint center (KJC) coordinates and 15 cross-sectional areas (CSA) for the thigh and the shank. The knee joint center was defined as the midpoint of the line connecting the femoral epicondyle markers [173] and serves as a critical landmark used in the digital orthopedic alignment process of the custom knee brace design (see Digital Alignment & Brace Cuff Design). The coordinates of both femoral epicondyle landmarks were extracted manually for all scans by selecting the surface point closest to the center of the plastic coins (determined visually based on the color texture of the 3D body) and saving the x,y,z coordinates in Meshlab log files. The rest of the measurements were extracted using a custom Python script which also computed the statistical analysis (see Python Scripts). The CSA for the shanks were spaced equidistantly starting from the anterior tibia plateau over the gastrocnemius muscle belly and stopping

before the ankle malleoli landmarks. The thigh CSA were also spaced equidistantly starting from the femoral epicondyle landmarks and covering the entire thigh. The limb bounding box was defined as the smallest box that contains the whole limb geometry in the x,y and z axes.

4.1.3 Statistical Analysis

Accuracy and precision (validity and reliability) of the smartphone scanning procedure were assessed using the statistical approach suggested by Hopkins [174]. This well-established analysis is used to quantify measurement agreement between two measurement methods. It consists of calculating the measurement differences between the two methods, calculating the mean bias and 95% limits of agreement (LoA) of the differences. For the accuracy assessment, the iSense sensor was considered the criterion and the smartphone was considered as the practical measurement system. For the precision assessment inter-rater and intra-rater analyses were performed. The data were organized in three groups (one for each scan repetition) for the intra-rater analysis. For the inter-rater analysis the data were organized in another three groups (one for each rater). The following variables were calculated with a 95% Confidence Interval (CI) for all variables: change in the mean (the mean difference between the repeated scan results), typical error of the measurements (TEMs) and Intra-class Correlation Coefficients (ICC(3,1)) [175]. The intra and inter-rater variability was calculated as $1.96\sqrt{2}\,TEMs$ following the Bland-Altman method [176] and as reported in reliability studies for residual limb geometry [176]–[178]. ICC values between 0.75 and 0.9 were considered good reliability and values greater than 0.9 were considered excellent reliability [179]. HD mean and BBox values for change in the mean, TEMs and intra/inter-rater variability below 20mm were considered good and above were considered bad (see Design Requirements). KJC values for change in the mean, TEMs and intra/inter-rater variability below 5mm were considered good and above were considered bad (see Design Requirements).

4.2 Results

The measured limb volumes ranged from 4088 ml to 11378 ml (Table 1). The maximum Hausdorff Distance ranged from 30.2 mm to 73.9 mm or 4.37 % to 8.79 % of their mesh' bounding box diagonal. The largest mean Hausdorff Distances ranged from 6.8 mm to 11.2 mm (0.98 % to 1.61 %).

Table 1 - Participant overall measurements. HD = Hausdorff Distance

	Female 1	Female 2	Male 1	Male 2
BMI [kg/m^2]	18.8	19.9	22.9	27.3
Mean Volume [ml]	4762.5±565.6	6713.8±571.0	6394.7±477.4	10005.8±669.7
Max HDMax [mm]	47.3	30.2	41.0	73.9
Max HDMax [%]	6.73	4.37	5.68	8.79
Mean HDMax [mm]	11.2	6.8	7.7	10.9
Mean HDMax[%]	1.61	0.98	1.07	1.29

4.2.1 Validity

Bland-Altman plots show that the smartphone photogrammetry method underestimated the limb volume by approximately 600 ml compared to the iSense sensor (Figure 30). This bias corresponded to 11% of the actual volumes. A clear separation of the data showed that the four chosen participants cover a large range of body sizes (BMI range: 18.8 – 27.3). The cluster on the right side of the graph represents the participant "Male 2" with a mean volume of 10005.8 ± 669.7 ml. The participants "Female 2" and "Male 1" have similar volumes (6713.8 ± 571.0 ml and 6394.7 ± 477.4 ml respectively) and are clustered together in the middle. The "Female 1" participant has a mean volume of 4762.5 ± 565.6 ml and is also clearly separated from the other participants.

The participant "Male 2" has the largest spread (absolute and percentage) and is the only one with overestimated values. This outlier ultimately affected the 95% limits of agreement to be large (around 1.5L). The other three participants have similar absolute spread however the percentage(relative) spread for "Female 1" is more pronounced due to a smaller volume average.

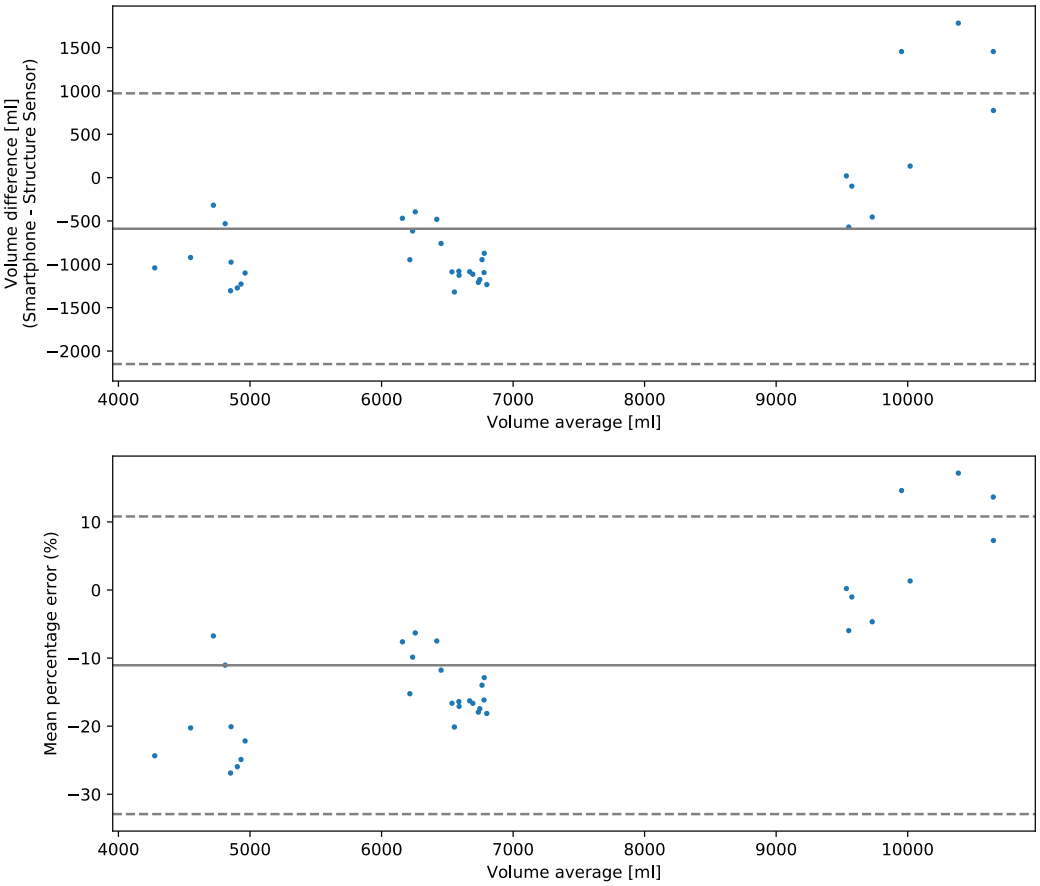

Figure 30 - Bland-Altman plot of the volume measurements. Top is the absolute difference between the smartphone photogrammetry and the iSense sensor. Bottom is the error of the smartphone volume measurements expressed as a percentage of the volume average. A negative value represents that the smartphone underestimates the volume with respect to the iSense sensor. The solid lines represent the mean of the differences and the mean of the errors. The dashed lines represent the upper and lower 95% limits of agreement.

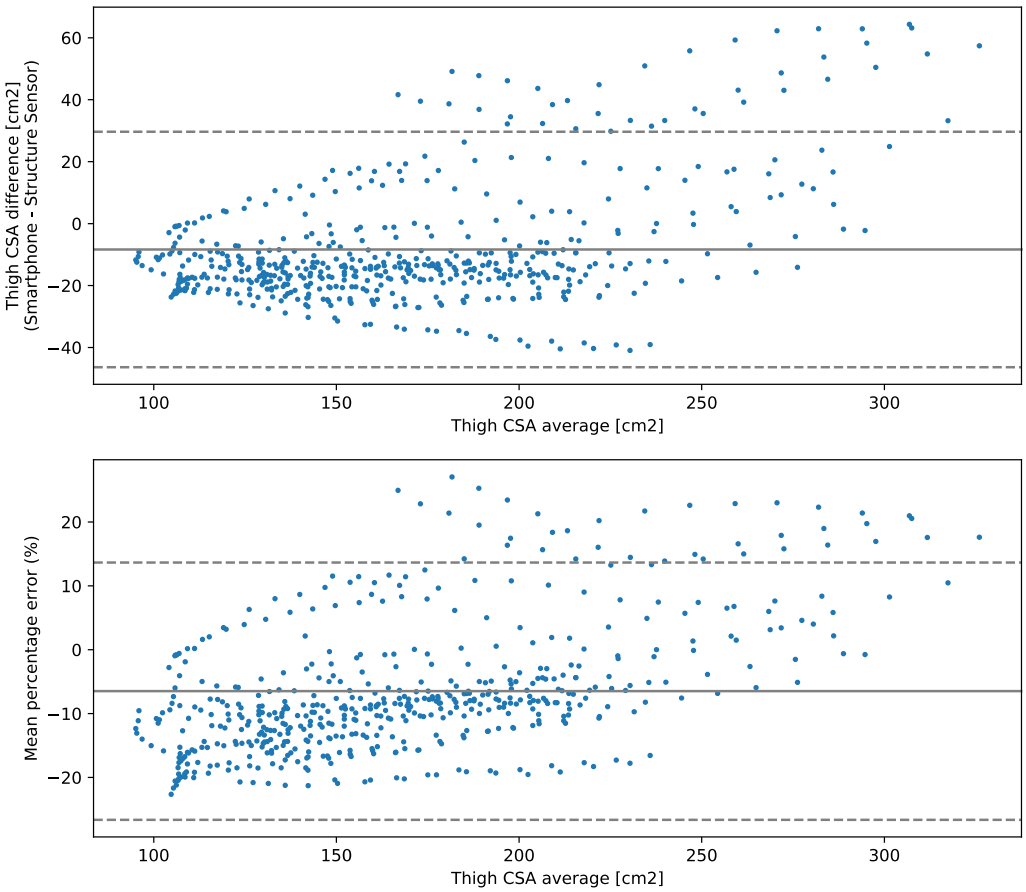

Figure 31 – Bland-Altman plots for the cross-sectional area (CSA) measurements of the thigh. Top is the absolute difference between the smartphone photogrammetry and the iSense sensor. Bottom is the error of the smartphone measurements expressed as a percentage of the average. A negative value represents that the smartphone underestimates the CSA with respect to the iSense sensor. The solid lines represent the mean of the differences and the mean of the errors. The dashed lines represent the upper and lower 95% limits of agreement.

The Bland-Altman plots for the cross-sectional areas (CSA) also revealed that the smartphone method underestimated the limb geometry. For the thigh portion, the magnitude of the absolute difference was around -9 cm^2 or around -8% of the CSA average (Figure 31). For the shank portion the magnitude of the absolute difference was around -11 cm^2 or around -15% of the CSA average (Figure 32). Additionally, for both the thigh and shank CSA the difference increased with the average. The larger CSA were mostly overestimated which was reflective of the "Male 2" volume overestimations.

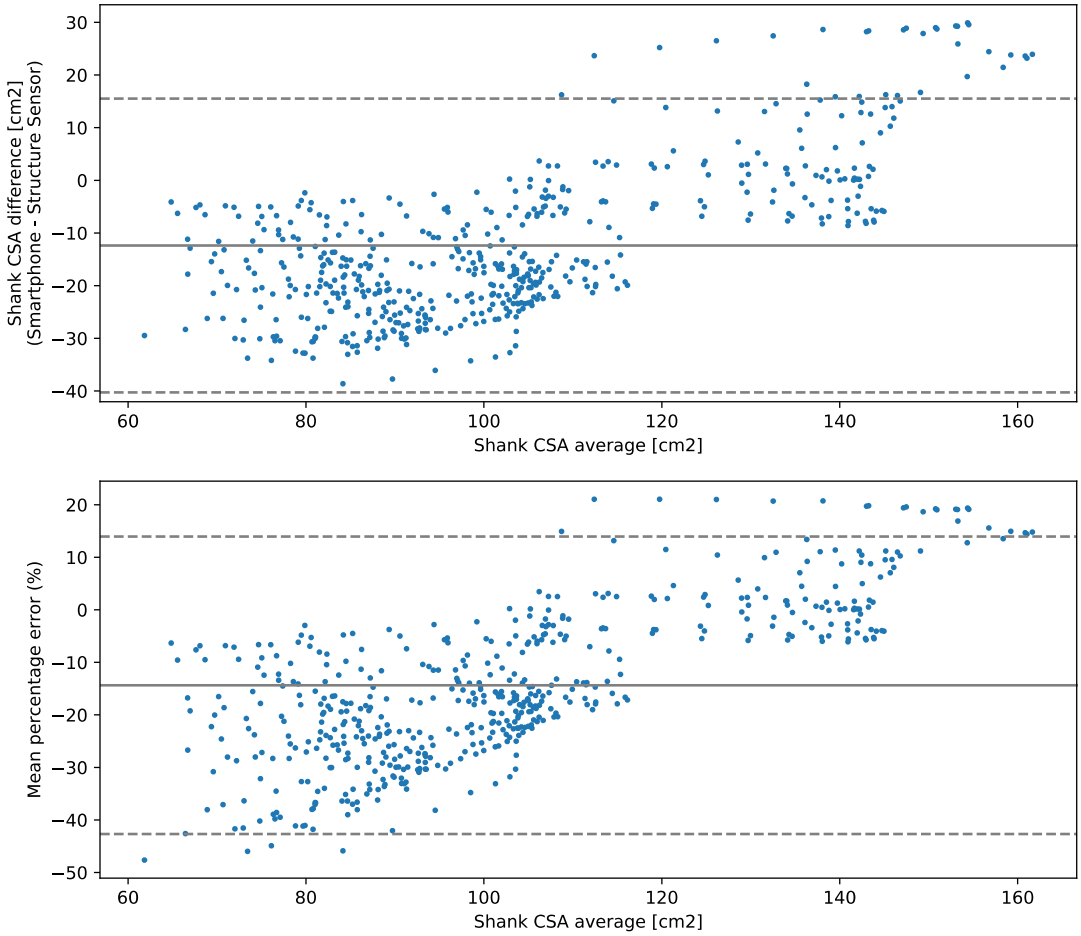

Figure 32 - Bland-Altman plots for the cross-sectional area (CSA) measurements of the shank. Top is the absolute difference between the smartphone photogrammetry and the iSense sensor. Bottom is the error of the smartphone measurements expressed as a percentage of the average. A negative value represents that the smartphone underestimates the CSA with respect to the iSense sensor. The solid lines represent the mean of the differences and the mean of the errors. The dashed lines represent the upper and lower 95% limits of agreement.

The bounding box size measurements (i.e. anterior-posterior, medial-lateral and proximal-distal) also confirmed the underestimation of the smartphone method relative to the iSense sensor with the largest bias of -7.4 mm in the anterior-posterior axis. The KJC coordinates had bias values < 5mm for the anterior-posterior and medial-lateral axis however for the proximal-distal the bias was 6.8 mm (Table 2).

Table 2 - Validity Results. BBox = Bounding Box measurements, Ant-Post = anterior-posterior axis, Med-Lat = medial-lateral axis, Prox-Dist = proximal-distal axis, KJC = knee joint center coordinates.

	Overall Bias		Limits of Agreement			
	Absolute	**Relative (%)**	**Absolute**	**Relative (%)**	**Pearson CC**	**CV (%)**
BBox						
Ant-Post (x)	-7.4 (-10.9; -3.9) mm	0.97 (0.69; 1.38)	20.3 mm	7.52	0.90	3.59
Med-Lat (y)	-3.4 (-7.3; 0.5) mm	0.98 (0.68; 1.40)	22.8 mm	7.91	0.86	4.08
Prox-Dist (z)	-0.5 (-2.8; 1.7) mm	1.00 (0.71; 1.40)	13.2 mm	7.11	1.00	1.00
KJC						
Ant-Post (x)	-3.3 (-5.2; -1.3) mm	-	11.5 mm	-	0.99	-
Med-Lat (y)	2.0 (0.8; 3.1) mm	-	6.8 mm	-	0.94	-
Prox-Dist (z)	6.8 (4.2; 9.3) mm	-	14.9 mm	-	1.00	-
Volume	-589.0 (-858.5; -319.5) ml	0.90 (0.62; 1.30)	1561.4 ml	8.78	0.96	5.82

4.2.2 Reliability

The smartphone photogrammetry method showed good levels of intra- and inter-rater reliability with ICCs greater than 0.90 (Table 3 and Table 4). The TEMs were below 5% for the bounding box and volume measurements and < 3mm for the KJC coordinates. The KJC coordinates showed the best inter- and intra-rater reliability coefficients which were < 5mm for the anterior-posterior and medial-lateral axis however for the proximal-distal axis they were over 6mm similar to the overall bias from the validity analysis.

Table 3 - Intra-rater reliability results. BBox = Bounding Box measurements, Ant-Post = anterior-posterior axis, Med-Lat = medial-lateral axis, Prox-Dist = proximal-distal axis, KJC = knee joint center coordinates.

		Typical Error of Measurement			
	Change In Mean	**Absolute**	**Relative (%)**	**Reliability**	**ICC**
BBox					
Ant-Post (x)	-2.1 (-9.6; 5.3) mm	8.3 (6.2; 12.4) mm	3.07 (2.30; 4.63)	22.9 mm	0.90
Med-Lat (y)	-0.9 (-6.7; 4.9) mm	6.5 (4.9; 9.7) mm	3.39 (2.54; 5.12)	18.0 mm	0.92
Prox-Dist (z)	-1.7 (-5.8; 2.3) mm	4.7 (3.5; 7.0) mm	0.79 (0.59; 1.18)	13.0 mm	1.00
KJC					
Ant-Post (x)	-0.6 (-2.1; 0.9) mm	1.7 (1.3; 2.6) mm	-	4.8 mm	1.00
Med-Lat (y)	-0.4 (-1.5; 0.7) mm	1.2 (0.9; 1.8) mm	-	3.4 mm	0.96
Prox-Dist (z)	-0.2 (-2.3; 1.8) mm	2.2 (1.7; 3.4) mm	-	6.2 mm	1.00
Volume	-228.9 (-565.3; 107.5) ml	375.3 (281.9; 561.3) ml	4.77 (3.56; 7.21)	1040.2 ml	0.98

Table 4 - Inter-rater reliability results. BBox = Bounding Box measurements, Ant-Post = anterior-posterior axis, Med-Lat = medial-lateral axis, Prox-Dist = proximal-distal axis, KJC = knee joint center coordinates.

		Typical Error of Measurement			
	Change In Mean	**Absolute**	**Relative (%)**	**Reliability**	**ICC**
BBox					
Ant-Post (x)	1.0 (-5.4; 7.3) mm	7.4 (5.6; 11.1) mm	2.74 (2.05; 4.12)	20.6 mm	0.92
Med-Lat (y)	0.4 (-4.9; 5.8) mm	5.9 (4.5; 8.9) mm	3.07 (2.30; 4.63)	16.5 mm	0.94
Prox-Dist (z)	0.8 (-2.8; 4.3) mm	4.0 (3.0; 5.9) mm	0.66 (0.5; 0.99)	11.0 mm	1.00
KJC					
Ant-Post (x)	-0.5 (-2.1; 1.1) mm	1.7 (1.3; 2.6) mm	-	4.8 mm	1.00

Med-Lat (y)	0.2 (-1.0; 1.4) mm	1.3 (1.0; 2.0) mm	-	3.7 mm	0.95
Prox-Dist (z)	0.4 (-1.7; 2.5) mm	2.3 (1.7; 3.5) mm	-	6.4 mm	1.00
Volume	48.6 (-238.7; 335.9) ml	320.8 (241.0; 479.8) ml	3.56 (2.66; 5.37)	889.14 ml	0.98

4.3 Discussion

This study assessed the validity and reliability of a novel low-cost 3D scanning method (versus the previously validated iSense sensor [38]) for the leg with a wide range of body sizes. This investigation was the first to provide validity, intra-rater and inter-rater reliability analysis for smartphone photogrammetry of human body leg geometry. Validity and reliability are important to determine the accuracy of new measurement methods, the quality of the data and if they are appropriate for clinical applications [180].

The study was designed to reflect sub-optimal but realistic results obtained with the developed smartphone photogrammetry procedure. As such, an iPhone 6S smartphone with a 12MP camera was used as the data collecting device. This was far from being the best smartphone camera available for the same price [181]. A higher MP count provides more data for the reconstruction algorithms and could drastically improve the results.

Dessery and Pallari [38] investigated the measurement agreement between the iSense sensor and a high-level 3D scanner (Artec EVA) for knee geometry. The iSense sensor showed to overestimate the circumference with a mean bias of 13mm (0.88%) and LoA from 1.4 to 24.8mm (-0.1% to 1.86%). Interestingly, the results from the smartphone photogrammetry method underestimated the iSense sensor for the volume and bounding box size measurements by 0.90 to 1.0 % and LoA from 7.11 to 8.78%. The larger LoA were a result of "Male 2" significantly affecting the analysis and therefore was representative of an outlier from large body sizes. The weight and height of Male 2 was 118kg and 208cm respectively while the average weight and height for US males between 20-29 years old is 84.7kg (90^{th} percentile = 113.3kg, 95^{th} percentile = 124.9kg) and 176.4cm (95^{th} percentile = 188.8cm) respectively [182]. In practice, such body sizes would require adding an additional step to the smartphone photogrammetry method such as taking the mean of multiple scans or performing a different regression prediction. Unfortunately, this study did not report any circumference measurement

since the chosen free software did not reveal to have the necessary tools. However, the CSA measurements are a similar measurement and were also showing underestimation.

Additionally, the low participant sample size is a limitation of this study. The developed workflow is targeted to late-teen pediatric populations and early adult populations. These populations were found to have a higher number of ACL knee injuries than mid-teens [183]. In this study, the sample population comprised of four young adult athletes of which Female 1 was considered to be representative of the late-teens pediatric populations and the other three were representative of the early adult populations. Although only four participants were recorded, two of the body sizes reported (female 1 BMI: 18.8, male 2 BMI: 27.3) represented close to the 5^{th} and 95^{th} percentiles for 20-29 year old US athletes (males: 18.29 and 28.96, females: 17.58 and 25.67) [184]. This could explain the relatively large LoA and it is reasonable to expect that a study with a larger sample size would show LoA closer to what was previously reported [38], [39]. Nonetheless the underestimation of the smartphone photogrammetry method suggests that it could reveal to be closer to the Artec EVA than the iSense sensor. With a 15.1 MP camera, the theoretical accuracy of a photogrammetry system is thought to be around 0.05 mm [151]. In practice reaching such measurement accuracy also relies on the 3D reconstruction algorithm and proper lighting. For this study, the free version of Autodesk Recap is the photogrammetry software used which limited the number of photos to 100. The paid version which allows up to 1000 photos would likely reveal to have better results.

The data collection location for the study was indoors where the only lighting came from ceiling lights. Figure 33 shows the HD as a color map (red means 0 and blue means > 5mm) for the two 3D meshes with the smallest mean HD obtained using the smartphone method (Male 1). The frontal view shows mostly red and yellow colors (0 – 1.5mm) while the rear view has a lot of green and some blue (2mm – 5mm). This clear contrast was very similar to the lighting contrast that was present during the smartphone photogrammetry procedure (Figure 3). It shows that the sub-optimal lighting clearly affected even the best results therefore it was likely a large contributor to measurement error. This was a good example that supports the necessity to have good, even and consistent lighting for successful photogrammetry as previously reported [150], [162]–[164].

Despite these sub-optimal conditions for the photogrammetry method, the anterior-posterior and medial-lateral KJC coordinates revealed to have overall absolute bias and reliability coefficients below the 5mm design requirement (Design Requirements). This requirement comes from a study [45] which showed large changes in the mechanics (forces and joint contact errors) due to only 5mm of anterior misplacement. The study also showed that anterior-posterior misplacement had the highest change and the proximal-distal misplacement is attributed with the least change.

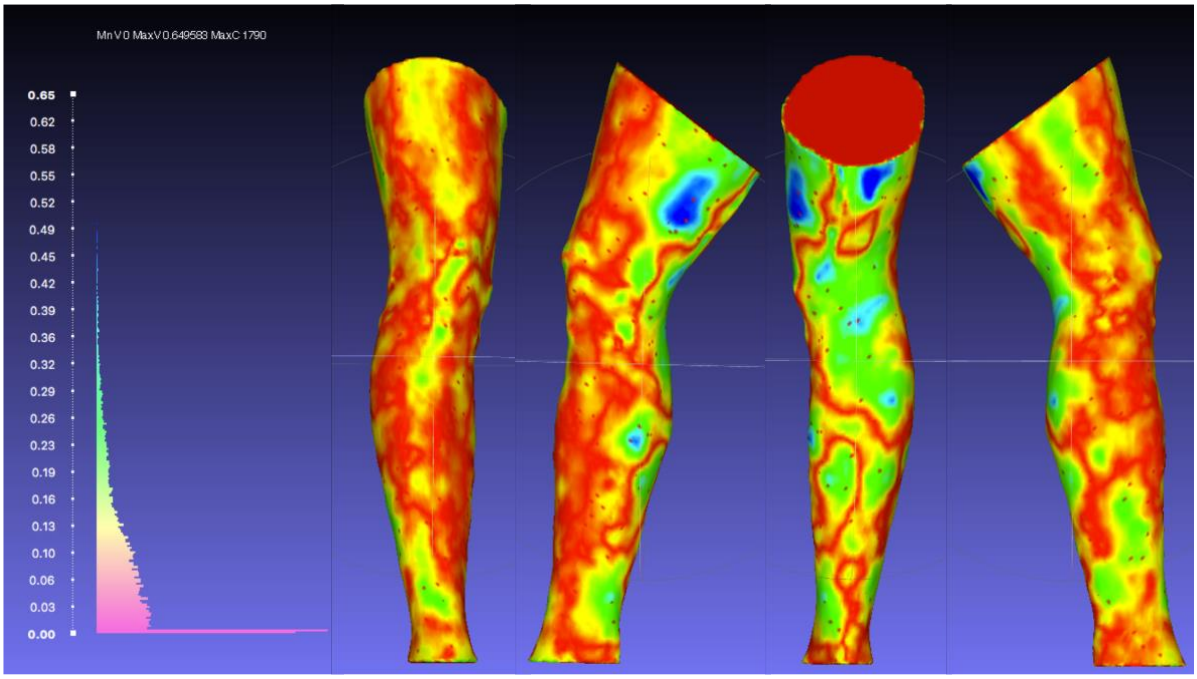

Figure 33 - Hausdorff distance color map of the two best scans obtained with the smartphone photogrammetry method. The left side shows the Hausdorff distance distribution in cm. Red means 0 distance and blue means the distance is > 5mm.

5 Conclusion and Future Work

5.1 Summary

This thesis provided the foundational work for a low-cost 3D printed custom knee brace. Specifically, the research, development and implementation of a novel workflow aimed to be easy to use and available to anyone who has access to a smartphone camera and 3D printing services. Our scanning method provides limb geometry results that are suitable for this application. The validation study was an explorative pilot study and the results can be used to guide the design of a larger study. This study should be repeated on a larger sample size with late-teens and early adults [183]. This sample could reveal to have a body size mean distribution closer to "Female 2" and "Male 1" which were the body sizes with the best results. The results could impact the decision regarding clinical use of the smartphone photogrammetry method.

The developed workflow was used to manufacture two prototypes which helped in the design iterations. As a result, an improved hinge was created which could reveal to have sufficient mechanical strength for a fully 3D printed custom knee brace. The second prototype suggested that a more conforming brace design could be more appropriate for successful EMG data collection.

This novel methodology required little training which could be provided through video instructions posted online. It would enable the patient to collect their own "3D scan" with the help of a friend or family member, effectively removing the need to book an appointment simply for collecting custom measurements. Additionally, it would allow the clinician to focus all their time on clinically relevant design tasks such as checking alignment, fit and comfort which could all potentially be improved by adopting digital methods. The ultimate vision is to make better custom knee braces which are easily accessible at a reduce cost.

5.2 Recommendations/Future Work

This thesis served as a critical initial step in the development of a low-cost custom knee brace. The smartphone photogrammetry method showed good early validation results and supports future investigation with a larger sample size. The larger study should perform data

collection outside during cloudy days to reduce error from bad lighting and to investigate the feasibility of a weather dependent method. Additionally, better accuracy and precision results can be obtained by using a smartphone with more megapixel, the full version of Autodesk Recap or another software such as a custom Maltab or Python script.

Regarding the design of the brace, future work should investigate optimal 3D printing parameters including material choice, printer type and build orientation of the cuffs. A dual-nozzle 3D printer which can use water-soluble support material would allow a wider range of printing orientation and could be used to determine optimal mechanical strength for the brace cuffs. Furthermore, mechanical testing of the improved hinge is needed. An Instron machine could be used for 3-point bend testing of the hinge for medial-lateral and flexion-extension loading scenarios. Impact testing would also be necessary before such a brace could be worn during sports activities. Ultimately, a hinge design which has patient-specific motion (dynamic customization) should be investigated.

While beyond the scope of this thesis, the workflow itself could be improved by automating mesh processing and design generation. Mesh processing and landmark detection/extraction could be automated with a machine learning algorithm that uses the 3D shape of the leg as input. A challenging step would be to collect real-time MRI and/or X-ray video to label the precise path of the knee joint center with respect to the exterior surface geometry. Instead, something possibly achievable within 1-2 years would be to collect a large number of 3D scans with the smartphone photogrammetry method and the KJC labelled (see Data Processing). Another could use two simultaneous video recordings (i.e: sagittal and frontal) to estimate the path of the KJC through frameworks such as OpenPose (https://github.com/CMU-Perceptual-Computing-Lab/openpose/blob/master/doc/output.md).

The current CAD workflow uses free software which are controllable with the Python programming language making it ideally suited for open-source community contributions. Making such a project open-source could bring significantly more contributions in a short amount of time allowing automation of the CAD much sooner and the impact becoming real. Many companies have certain operations that follow open-source models (i.e. Google, Facebook and Amazon) therefore the various types of open-source licenses should be investigated.

6 Appendix

6.1 Python Scripts

6.1.1 meshlabserverPyAuto.py

```
import os
import time
import numpy as np
import pandas as pd
import scipy.stats
import matplotlib.pyplot as plt
from importKJCdata import importKJCdata

start = time.time()
print("hello")

def bland_altman_plot(data1, data2, varname, units):
        data1 = np.asarray(data1)
        data2 = np.asarray(data2)
        mean = np.mean([data1, data2], axis=0)
        diff = data1 - data2                # Difference between data1 and data2
        md = np.mean(diff)                  # Mean of the difference
        sd = np.std(diff, axis=0)           # Standard deviation of the difference


        diffperc = 100*np.divide(diff, mean)
        mdperc = np.mean(diffperc)
        sdperc = np.std(diffperc, axis=0)

        fig=plt.figure(figsize=(10,9))

        ax1=plt.subplot2grid((2,1),(0,0),rowspan=1,colspan=1)
        ax1.scatter(mean, diff,s=5)
        ax1.axhline(md,           color='gray', linestyle='-')
        ax1.axhline(md + 1.96*sd, color='gray', linestyle='--')
        ax1.axhline(md - 1.96*sd, color='gray', linestyle='--')
        xlabel=varname+' average '+units
        ylabel= varname+' difference '+units+'\n(Smartphone - Structure Sensor)'
        ax1.set_xlabel(xlabel)
        ax1.set_ylabel(ylabel)

        ax2=plt.subplot2grid((2,1),(1,0),rowspan=1,colspan=1)
        ax2.scatter(mean, diffperc,s=5)
        ax2.axhline(mdperc,           color='gray', linestyle='-')
        ax2.axhline(mdperc + 1.96*sdperc, color='gray', linestyle='--')
```

```
        ax2.axhline(mdperc - 1.96*sdperc, color='gray', linestyle='--')
        xlabel=varname+' average '+units
        ylabel= 'Mean percentage error (%)'
        ax2.set_xlabel(xlabel)
        ax2.set_ylabel(ylabel)

        figname=varname+'_BlandAltman.pdf'

#       plt.show()

        fig.savefig(figname)

def validity (pract, crit):

        cl=95 # confidence limit is 95%
        mpract=np.mean(pract)
        mcrit=np.mean(crit)
        stdpract=np.std(pract)
        stdcrit=np.std(crit)
        N=len(pract)

        slope, intercept, r_value, p_value, std_err=scipy.stats.linregress(pract,crit)

        bias=pract-crit
        mbias=np.mean(bias)
        stdbias=np.std(bias)

        devsqpract= np.sum(np.square(pract - mpract)) # see definition of DEVSQ() in Excel

        tinv=-1*scipy.stats.t.ppf(((1-(cl/100))*0.5),N-1)
        biasLCL=mbias - tinv*stdbias/np.sqrt(N)
        biasUCL=mbias + tinv*stdbias/np.sqrt(N)

        LOA=1.96*stdbias
        r,p=scipy.stats.pearsonr(pract,crit)

        # relative stats
        logpract=100*np.log(pract)
        logcrit=100*np.log(crit)
        mlogcrit=np.mean(logcrit)
        mlogpract=np.mean(logpract)

        logbias=logpract-logcrit
        mlogbias=np.mean(logbias)
        stdlogbias=100*np.exp((1/100)*np.std(logbias))-1
```

```
        relbias=np.exp(mlogbias/100)
        tinv=-1*scipy.stats.t.ppf(((1-(cl/100))*0.5),N-1)
        relbiasLCL=np.exp((mlogbias - tinv*stdlogbias/np.sqrt(N))/100)
        relbiasUCL=np.exp((mlogbias + tinv*stdlogbias/np.sqrt(N))/100)
        relLOA=np.exp(1.96*stdlogbias/100)

        y2=np.sum(np.square(logcrit-mlogcrit))
        x2=np.sum(np.square(logpract-mlogpract))
        xy2=np.square(np.sum(np.multiply((logcrit-mlogcrit),(logpract-mlogpract))))
        steyx=np.sqrt((1/(N-2))*(y2 - xy2/x2)) # see Excel STEYX() documentation for
equation

        typicalerrorofestimate_factor=np.exp(steyx/100)
        CV_perc=(typicalerrorofestimate_factor-1)*100

        statsout=[mbias, biasLCL, biasUCL, relbias, relbiasLCL, relbiasUCL, LOA,
relLOA, r, CV_perc]

        return statsout


def reliability (dataset):

        dim=list(np.shape(dataset))
        N=dim[0]
        nrow=dim[0]
        ncol=dim[1]
        df=N-1
        cl=95

        # Changes in Score
        changescores=np.zeros((N,ncol-1))
        for i in range(ncol-1):
                changescores[:,i]=dataset[:,i+1]-dataset[:,i]

        # Change in Mean
        MeanOfChange=np.mean(changescores,axis=0)
        StdOfChange=np.std(changescores,axis=0)

        tinv=-1*scipy.stats.t.ppf(((1-(cl/100))*0.5),df)
        MeanOfChangeLCL=MeanOfChange - tinv*StdOfChange/np.sqrt(N)
        MeanOfChangeUCL=MeanOfChange + tinv*StdOfChange/np.sqrt(N)

        ChangeInMean=np.mean(MeanOfChange)
        ChangeInMeanLCL=np.mean(MeanOfChangeLCL)
        ChangeInMeanUCL=np.mean(MeanOfChangeUCL)
```

```
        # Mean of the typical error with lower and upper confidence levels
        TypicalError=np.std(changescores, axis=0)/np.sqrt(2)
        sumproduct=np.sum(df*(np.multiply(TypicalError,TypicalError)))
        mTypicalError=np.sqrt(sumproduct/(df*(ncol-1)))

        meanDF=(1-0.22*N*ncol/(ncol*N))*df*(ncol-1)
        Q67=meanDF
        Q56=mTypicalError
        probability=(1-cl/100)/2
        CHIINV=scipy.stats.chi2.ppf(1-probability, Q67)
        mTypicalErrorLCL=np.sqrt(Q67*np.power(Q56,2)/CHIINV)

        CHIINV=scipy.stats.chi2.ppf(1-(1-probability), Q67)
        mTypicalErrorUCL=np.sqrt(Q67*np.power(Q56,2)/CHIINV)

        #Reliability Coefficient
        ReliabilityC=1.96*np.sqrt(2)*mTypicalError

        #ICC raw data
        mdataset=np.mean(dataset, axis=0)
        stddataset=np.std(dataset, axis=0)
        sumproduct=np.sum(df*(np.multiply(stddataset,stddataset)))
        J43=np.sqrt(sumproduct/(df*ncol))
        R42=nrow
        mICC=(1-np.power(Q56,2)/np.power(J43,2))*(1+(1-np.power((1-
np.power(Q56,2)/np.power(J43,2)),2))/(R42-3))

        # Relative stats
        logdataset=100*np.log(dataset)
        changescoreslog=np.zeros((N,ncol-1))
        for i in range(ncol-1):
                changescoreslog[:,i]=logdataset[:,i+1]-logdataset[:,i]
        logTypicalError=np.std(changescoreslog, axis=0)/np.sqrt(2)
        sumproduct=np.sum(df*(np.multiply(logTypicalError,logTypicalError)))
        mlogTypicalError=np.sqrt(sumproduct/(df*(ncol-1)))
        mpercTypicalError=100*np.exp(mlogTypicalError/100) - 100

        AI119=meanDF
        AI109=mlogTypicalError
        CHIINV=scipy.stats.chi2.ppf(1-probability, AI119)
        mlogTypicalErrorLCL=np.sqrt(AI119*np.power(AI109,2)/CHIINV)
        mpercTypicalErrorLCL=100*np.exp(mlogTypicalErrorLCL/100) - 100

        CHIINV=scipy.stats.chi2.ppf(1-(1-probability), AI119)
        mlogTypicalErrorUCL=np.sqrt(AI119*np.power(AI109,2)/CHIINV)
```

```
        mpercTypicalErrorUCL=100*np.exp(mlogTypicalErrorUCL/100) - 100

        statsout=[ChangeInMean, ChangeInMeanLCL, ChangeInMeanUCL, mTypicalError,
mTypicalErrorLCL, mTypicalErrorUCL, ReliabilityC, mpercTypicalError,
mpercTypicalErrorLCL, mpercTypicalErrorUCL, mICC, MeanOfChange,
MeanOfChangeLCL, MeanOfChangeUCL]

        return statsout

# Example of meshlab command to run
"""
meshlabserver command example

meshlabserver -l
C:/Users/omigu094/Desktop/MeshLabScripting/Celi/ComparisonResults/log_CPB1vsCPB2.
txt -i C:/Users/omigu094/Desktop/MeshLabScripting/Celi/CPB1.ply -i
C:/Users/omigu094/Desktop/MeshLabScripting/Celi/CPB2.ply -s
C:/Users/omigu094/Desktop/MeshLabScripting/Hausdorff_Distance.mlx -o
C:/Users/omigu094/Desktop/MeshLabScripting/Celi/ComparisonResults/CPB1vsCPB2.ply
-m vc vf vq vn vt fc ff fq fn wc wn wt

-i C:/Users/omigu094/Desktop/MeshLabScripting/Celi/CPB1.ply

-i C:/Users/omigu094/Desktop/MeshLabScripting/Celi/CPB2.ply

-o
C:/Users/omigu094/Desktop/MeshLabScripting/Celi/ComparisonResults/CPB1vsCPB2.ply
-m vc vf vq vn vt fc ff fq fn wc wn wt

-s C:/Users/omigu094/Desktop/MeshLabScripting/Hausdorff_Distance.mlx

-l
C:/Users/omigu094/Desktop/MeshLabScripting/Celi/ComparisonResults/log_CPB1vsCPB2.
txt
"""


# Define project path

# Lab computer
# projectfolder= "C:/Users/omigu094/Desktop/MeshLabScripting/"
# meshlabservercall="meshlabserver"

# Olivier Macbook Pro
projectfolder= "/Users/Olivier/3DAnalysisSession1/"
meshlabservercall="/Applications/meshlab.app/Contents/MacOS/meshlabserver"
```

```
outputfolder= projectfolder+"MeshLabLogResults/"
filterfolder=projectfolder+"Filters/"
inputfolder=projectfolder+'MeshesSolid/'


# Define scripts to be used
hausmlxscriptfilename = filterfolder+"HausdorffDistance_ColorizebyVertexQuality.mlx"
geomlxscriptfilename = filterfolder+"GeoMeasures.mlx"

# full lists of file categories
subjectList = ["Lisa","Celi","Mike","Nick"]
deviceID = ["P", "S"]
partList = ["B", "La","Lu"]

# test lists
# subjectList = ["Lisa"]
# partList = ["B"]
# deviceID = ["P"]

trials=[1,2,3]

# Scans metadata
nscans=len(partList)*len(deviceID)*len(trials)
nsub=len(subjectList)
fileIDList=[[None]*nscans for i in range(nsub)]

# List of variables that are outputted. Currently only works with the Hausdorff Distance
variable
dataoutlist=["HauDisMaxCent","HauDisMaxPerc","HauDisMeanCent","HauDisMeanPerc"]

# Trying to use "dictionary" to define the variables. This way to whole code can be looped
through the dictionary and run the same stuff for all variables in the dictionary
"""
vardict={}


for item in dataoutlist:
        vardict[item]=np.zeros(shape=(nsub,nscans,nscans))
"""

# Mesh variables
HauDisMaxCent=np.zeros(shape=(nsub,nscans,nscans))
HauDisMaxPerc=np.zeros(shape=(nsub,nscans,nscans))
HauDisMeanCent=np.zeros(shape=(nsub,nscans,nscans))
HauDisMeanPerc=np.zeros(shape=(nsub,nscans,nscans))
BBoxSize=np.zeros(shape=(nsub,nscans,3))
```

```
SurfArea=np.zeros(shape=(nscans,nsub))
Volume=np.zeros(shape=(nscans,nsub))

# Cross section surface area variables
planeZsections=[np.arange(25,40),np.arange(25,40),np.arange(-10,5),np.arange(35,50)]
planeCsections=[np.arange(33,48),np.arange(30,45),np.arange(9,24),np.arange(58,73)]
nsect=30
CrossSurfArea=np.zeros(shape=(nsub,nscans,nsect))


list_trialID=[]
# Creates a list containing the mesh file names without the extension
for s,subject in enumerate(subjectList):
        n=0
        for device in deviceID:
                for participant in partList:
                        for trial in trials:
                                fileIDList[s][n] = subject[0]+device+participant+str(trial)

                                if s==0:
                                        list_trialID=list_trialID+[device+participant+str(trial)]

                                n=n+1

# Runs through all the files and extracts the values for the variables defined above

for s,subject in enumerate(subjectList):

        for t,targetFileID in enumerate(fileIDList[s]):
                targetfilename = inputfolder+targetFileID+".ply" # target file
                targetfileinputcmd = " -i "+targetfilename

                # This block runs "Compute Planar Section" and "Compute Geometric
Measures" filters to extract the CrossSurfArea from 15 slices of the tibia and thigh for each
file
                for z,sect in enumerate(planeZsections[s]):
                        logfilename =
outputfolder+targetFileID+"LOG_PlanarSectionGeoMeasuresZ"+str(sect)+".txt"
                        logfilecmd = " -l "+logfilename

        planesectmlxscriptname=filterfolder+'PlanarSection_GeoMeasure_Z_'+str(sect)+'_m
esh.mlx'
                        mlxscriptcmd = " -s "+planesectmlxscriptname
                        meshlabservercmd=meshlabservercall + logfilecmd +
targetfileinputcmd + mlxscriptcmd
                        #os.system(meshlabservercmd)
```

```
                    with open(logfilename) as file:
                        data = file.readlines()
                        CrossSurfAreaLine=data[8].split()
                        CrossSurfArea[s][t][z]=float(CrossSurfAreaLine[4])

                for c,sect in enumerate(planeCsections[s]):

                    if s==2:
                        caxes="(-0d7_0_1)_"
                    elif s==3:
                        caxes="(-0d5_0_1)_"
                    else:
                        caxes="(1_0_1)_"

                    logfilename =
outputfolder+targetFileID+"LOG_PlanarSectionGeoMeasuresC"+caxes+str(sect)+".txt"
                    logfilecmd = " -l "+logfilename

        planesectmlxscriptname=filterfolder+"PlanarSection_GeoMeasure_C"+caxes+str(se
ct)+"_mesh.mlx"
                    mlxscriptcmd = " -s "+planesectmlxscriptname
                    meshlabservercmd=meshlabservercall + logfilecmd +
targetfileinputcmd + mlxscriptcmd
                    #print(meshlabservercmd)
#                   os.system(meshlabservercmd)

                    with open(logfilename) as file:
                        data = file.readlines()
                        CrossSurfAreaLine=data[8].split()
                        CrossSurfArea[s][t][z+c+1]=float(CrossSurfAreaLine[4])

                # This block runs the "Compute Geometric Measures" filter on all the scans
                logfilename = outputfolder+targetFileID+"_GeoMeasures.txt"
                logfilecmd = " -l "+logfilename
                mlxscriptcmd = " -s "+geomlxscriptfilename
                meshlabservercmd=meshlabservercall + logfilecmd + targetfileinputcmd +
mlxscriptcmd
                # run the command
#               os.system(meshlabservercmd)

                with open(logfilename) as file:
                    data = file.readlines()
                    BBoxSizeLine=data[3].split() # line containing BBoxSize data in cm
                    BBoxSize[s][t]=[float(BBoxSizeLine[4]),
float(BBoxSizeLine[5]),float(BBoxSizeLine[6])]
```

```
                    SurfAreaLine=data[7].split()
                    SurfArea[t][s]=float(SurfAreaLine[4])
                    VolumeLine=data[12].split()
                    Volume[t][s]=float(VolumeLine[3])

                # temporary block to remove colors
                '''
                outputfolder=projectfolder+'MeshesNoColor/'
                outputfilecmd=" -o " + outputfolder + targetFileID + ".ply"
                meshlabservercmd=meshlabservercall + targetfileinputcmd + outputfilecmd
                os.system(meshlabservercmd)
                '''

                # This loop computes the Hausdorff distance filter between all the files for
each subject
                for sam,sampledFileID in enumerate(fileIDList[s]):
                        mlxscriptcmd = " -s "+hausmlxscriptfilename
                        sampledfilename = inputfolder+sampledFileID+".ply" #sampled file
                        sampledfileinputcmd = " -i "+sampledfilename
                        logfilename =
outputfolder+"log_"+targetFileID+"vs"+sampledFileID+".txt"
                        logfilecmd = " -l "+logfilename
                        outputfilecmd=" -o " + outputfolder + targetFileID + "vs" +
sampledFileID + ".ply -m vc vf vq vn vt"

                        # full command
                        #print('sam='+sampledfilename)
                        #print('t='+targetfilename)
                        meshlabservercmd=meshlabservercall + logfilecmd +
sampledfileinputcmd + targetfileinputcmd + mlxscriptcmd + outputfilecmd

                        # run the command
#                       os.system(meshlabservercmd)

                        with open(logfilename) as file:
                                data = file.readlines()
                                cmLine=data[7].split() # line containing data in cm
                                HauDisMaxCent[s][t][sam]=float(cmLine[4])
                                HauDisMeanCent[s][t][sam]=float(cmLine[7])

                                percLine=data[9].split() # line containing data in perc
                                HauDisMaxPerc[s][t][sam]=float(percLine[4])
                                HauDisMeanPerc[s][t][sam]=float(percLine[7])

# # testing command outside looping
# os.system(meshlabservercmd)
```

```
# print(type(meshlabservercmd), len(meshlabservercmd))
# print(meshlabservercmd)
# print(data)

# Calculate min and max values for Hausdorff Distances for each subject
for s in range(len(subjectList)):
        a=HauDisMeanCent[s][:][:]
        minval = np.min(a[np.nonzero(a)])
        maxval = np.max(a[np.nonzero(a)])

# Here the data in the variables are written in text files for human verification

#Write CrossSurfArea (CSA) data into txt file
outfilename=outputfolder+'CSA.txt'
with open(outfilename, 'wb') as outfile:
        data=CrossSurfArea
        outfile.write(b'# CrossSurfArea Size Array shape: %a \n' % np.array(np.shape))
#       print('CrossSurfArea Size Array shape: '+str(data.shape))
        for data_slice in data:
                np.savetxt(outfile, data_slice, fmt='%-7.6f')
                outfile.write(b'# New slice\n')

#Write GeoMeasures data into txt file
outfilename=outputfolder+'GeoMeasures.txt'
with open(outfilename, 'wb') as outfile:
        data=BBoxSize
        outfile.write(b'# BBox Size Array shape: %a \n' % np.array(np.shape))
        for data_slice in data:
                np.savetxt(outfile, data_slice, fmt='%-7.6f')
                outfile.write(b'# New slice\n')

        data=SurfArea
        outfile.write(b'# SurfArea Array shape: %a \n' % np.array(np.shape))
        np.savetxt(outfile, data, fmt='%-7.6f')

        data=Volume
        outfile.write(b'# Volume Array shape: %a \n' % np.array(np.shape))
        np.savetxt(outfile, data, fmt='%-7.6f')

# Write Hausdorff_Distance to txt file
for i in range(len(dataoutlist)):
# Generate some test data

        if i==0:
                data = HauDisMaxCent
                outfilename=outputfolder+'HauDisMaxCent.txt'
```

```
        if i==1:
                data = HauDisMaxPerc
                outfilename=outputfolder+'HauDisMaxPerc.txt'
        if i==2:
                data = HauDisMeanCent
                outfilename=outputfolder+'HauDisMeanCent.txt'
        if i==3:
                data = HauDisMeanPerc
                outfilename=outputfolder+'HauDisMeanPerc.txt'

        # Write the array to disk
        with open(outfilename, 'wb') as outfile:
                # I'm writing a header here just for the sake of readability
                # Any line starting with "#" will be ignored by numpy.loadtxt
                outfile.write(b'# Array shape: %a \n' % np.array(np.shape))

                # Iterating through a ndimensional array produces slices along
                # the last axis. This is equivalent to data[i,:,:] in this case
                for data_slice in data:

                        minval = np.min(data_slice[np.nonzero(data_slice)])
                        maxval = np.max(data_slice[np.nonzero(data_slice)])
                        maxindex = np.where(data_slice==maxval)
                        minindex = np.where(data_slice==minval)
                        maxline='# Max: '+str(maxval)+' @ '+str(maxindex)+'\n'
                        minline='# Min: '+str(minval)+' @ '+str(minindex)+'\n'
                        # The formatting string indicates that I'm writing out
                        # the values in left-justified columns 7 characters in width
                        # with 2 decimal places.
                        np.savetxt(outfile, data_slice, fmt='%-7.6f')

                        outfile.write(maxline.encode())
                        outfile.write(minline.encode())

                        # Writing out a break to indicate different slices...
                        outfile.write(b'# New slice\n')

# print(HauDisMaxCent)
# print(BBoxSize)
# print(SurfArea)
# print(CrossSurfArea)


#### Statistics
```

```
### Measurement variables
list_measr=['Volume_ml','BoundingBox_x_cm','BoundingBox_y_cm','BoundingBox_z_cm',
'KJC_x_cm','KJC_y_cm','KJC_z_cm']

### Setting the DataFrames

## Validity
list_validstats=['mbias', 'biasLCL', 'biasUCL', 'relbias', 'relbiasLCL', 'relbiasUCL', 'LOA',
'relLOA', 'PearCC', 'CV_perc']
nvar=len(list_validstats)
dict_validstats={'Stats':list_validstats, list_measr[0]:np.zeros(nvar),
list_measr[1]:np.zeros(nvar), list_measr[2]:np.zeros(nvar), list_measr[3]:np.zeros(nvar),
list_measr[4]: np.zeros(nvar), list_measr[5]:np.zeros(nvar),list_measr[6]:np.zeros(nvar)}
df_valid=pd.DataFrame(dict_validstats)
df_valid.set_index('Stats',inplace=True)

## Reliability
list_relistats=['ChangeInMean', 'ChangeInMeanLCL', 'ChangeInMeanUCL',
'mTypicalError', 'mTypicalErrorLCL', 'mTypicalErrorUCL', 'ReliabilityC',
'mpercTypicalError', 'mpercTypicalErrorLCL', 'mpercTypicalErrorUCL', 'mICC',
'MeanOfChange', 'MeanOfChangeLCL', 'MeanOfChangeUCL']

df_interreliP=pd.DataFrame(index=list_relistats, columns=list_measr)
# print(df_interreli)
df_intrareliP=pd.DataFrame(index=list_relistats, columns=list_measr)


### Volume Statistics
# print(Volume)
# print(type(Volume))
# print(fileIDList)

df_vol=pd.DataFrame(data=Volume,index=list_trialID, columns=subjectList)
# print(df_vol)

# Used for a quick fix in excel.
# writer = pd.ExcelWriter('Volume.xlsx')
# df_vol.to_excel(writer,'Sheet1')
# writer.save()

# Import Volume2.xlsx
df_relivol=pd.read_excel('Volume2.xlsx')
# print(df_relivol)

## Reliability
df_relivolP=df_relivol.stack(level=0)
```

```
# print(df_relivolP)
df_relivolP=df_relivolP.unstack(level=0)
# print(df_relivolP)
df_relivolP=df_relivolP.P
# print(df_relivolP)

# Intra-rater
df_intrarelivolP=df_relivolP.unstack(level=1)
# print(df_intrarelivolP)
df_intrareliP.Volume_ml=reliability(np.array(df_intrarelivolP))
# print(df_intrareliP)

# Inter-rater

df_interrelivolP=df_relivolP.unstack(level=0)
# print(df_interrelivolP)
df_interreliP.Volume_ml=reliability(np.array(df_interrelivolP))
# print(df_interreliP)

## Validity
pract=df_vol[:]['PB1':'PLu3']
pract=np.array(pract.T.stack())
# print(pract)
# print(np.shape(pract))

crit=df_vol[:]['SB1':'SLu3']
crit=np.array(crit.T.stack())

df_valid.Volume_ml=validity(pract,crit)

# bland_altman_plot(pract, crit, 'Volume', '[ml]')


### BBox Statistics

## Validity
dim=list(np.shape(BBoxSize))
pract=np.zeros(((len(subjectList)*len(partList)*len(trials)),dim[2]))
crit=np.zeros(((len(subjectList)*len(partList)*len(trials)),dim[2]))

BBoxSizeArr=np.asarray(BBoxSize)
for i in range(dim[2]):
        for p in range(dim[0]):
                pract[p*9:(p+1)*9,i]=BBoxSizeArr[p,0:9,i]
                crit[p*9:(p+1)*9,i]=BBoxSizeArr[p,9:18,i]
```

```
df_valid.BoundingBox_x_cm=validity(pract[:,0],crit[:,0])
df_valid.BoundingBox_y_cm=validity(pract[:,1],crit[:,1])
df_valid.BoundingBox_z_cm=validity(pract[:,2],crit[:,2])

## Reliability
# print(BBoxSizeArr)
concat_BBoxArr=np.concatenate((BBoxSizeArr[0,:,:],BBoxSizeArr[1,:,:],BBoxSizeArr[2,:,:
],BBoxSizeArr[3,:,:]),axis=1)
# print(concat_BBoxArr)
df_BBox=pd.DataFrame(data=concat_BBoxArr)
# print(df_BBox)

# Used for a quick fix in excel.
# writer = pd.ExcelWriter('BBox.xlsx')
# df_BBox.to_excel(writer,'Sheet1')
# writer.save()

# Import BBox2.xlsx
df_reliBBox=pd.read_excel('BBox2.xlsx')

## Reliability X

df_reliBBoxx=df_reliBBox[['Lisax','Celix','Mikex','Nickx']]
df_reliBBoxx.columns=['Lisa','Celi','Mike','Nick']
df_reliBBoxx=df_reliBBoxx.stack(level=0)
df_reliBBoxx=df_reliBBoxx.unstack(level=0)
df_reliBBoxxP=df_reliBBoxx.P

# Inter-Rater Reliability

df_interreliBBoxxP=df_reliBBoxxP.unstack(level=0)
df_interreliP.BoundingBox_x_cm=reliability(np.array(df_interreliBBoxxP))

# Intra-Rater Reliability

df_intrareliBBoxxP=df_reliBBoxxP.unstack(level=1)
df_intrareliP.BoundingBox_x_cm=reliability(np.array(df_intrareliBBoxxP))

## Reliability Y

df_reliBBoxy=df_reliBBox[['Lisay','Celiy','Mikey','Nicky']]
df_reliBBoxy.columns=['Lisa','Celi','Mike','Nick']
df_reliBBoxy=df_reliBBoxy.stack(level=0)
df_reliBBoxy=df_reliBBoxy.unstack(level=0)
df_reliBBoxyP=df_reliBBoxy.P
```

```
# Inter-Rater Reliability

df_interreliBBoxyP=df_reliBBoxyP.unstack(level=0)
df_interreliP.BoundingBox_y_cm=reliability(np.array(df_interreliBBoxyP))

# Intra-Rater Reliability

df_intrareliBBoxyP=df_reliBBoxyP.unstack(level=1)
df_intrareliP.BoundingBox_y_cm=reliability(np.array(df_intrareliBBoxyP))

## Reliability Z

df_reliBBoxz=df_reliBBox[['Lisaz','Celiz','Mikez','Nickz']]
df_reliBBoxz.columns=['Lisa','Celi','Mike','Nick']
df_reliBBoxz=df_reliBBoxz.stack(level=0)
df_reliBBoxz=df_reliBBoxz.unstack(level=0)
df_reliBBoxzP=df_reliBBoxz.P

# Inter-Rater Reliability

df_interreliBBoxzP=df_reliBBoxzP.unstack(level=0)
df_interreliP.BoundingBox_z_cm=reliability(np.array(df_interreliBBoxzP))

# Intra-Rater Reliability

df_intrareliBBoxzP=df_reliBBoxzP.unstack(level=1)
df_intrareliP.BoundingBox_z_cm=reliability(np.array(df_intrareliBBoxzP))

### KJC stats

## import data
df_KJCvalid, df_KJCreli = importKJCdata()
# print(df_KJCvalid)
# print(df_KJCreli)

## Reliability X

df_reliKJCx=df_KJCreli[['Lisa_x','Celi_x','Mike_x','Nick_x']]
# print(df_reliKJCx)
df_reliKJCx.columns=['Lisa','Celi','Mike','Nick']
# print(df_reliKJCx)

# Intra-Rater Reliability

df_intrareliKJCx=df_reliKJCx.stack(level=0)
```

```
# print(df_intrareliKJCx)
df_intrareliKJCx=df_intrareliKJCx.unstack(level=0)
# print(df_intrareliKJCx)
df_intrareliKJCxP=df_intrareliKJCx.P
# print(df_intrareliKJCxP)
df_intrareliKJCxP=df_intrareliKJCxP.unstack(level=0)
# print(df_intrareliKJCxP)
df_intrareliP.KJC_x_cm=reliability(np.array(df_intrareliKJCxP))
# print(df_intrareliP)

# Inter-Rater Reliability

df_interreliKJCx=df_reliKJCx.stack(level=0)
# print(df_interreliKJCx)
df_interreliKJCx=df_interreliKJCx.unstack(level=0)
# print(df_interreliKJCx)
df_interreliKJCxP=df_interreliKJCx.P
# print(df_interreliKJCxP)
df_interreliKJCxP=df_interreliKJCxP.unstack(level=1)
# print(df_interreliKJCxP)
df_interreliP.KJC_x_cm=reliability(np.array(df_interreliKJCxP))
# print(df_interreliP)

## Reliability Y

df_reliKJCy=df_KJCreli[['Lisa_y','Celi_y','Mike_y','Nick_y']]
df_reliKJCy.columns=['Lisa','Celi','Mike','Nick']

# Intra-Rater Reliability

df_intrareliKJCy=df_reliKJCy.stack(level=0)
df_intrareliKJCy=df_intrareliKJCy.unstack(level=0)
df_intrareliKJCyP=df_intrareliKJCy.P
df_intrareliKJCyP=df_intrareliKJCyP.unstack(level=0)
df_intrareliP.KJC_y_cm=reliability(np.array(df_intrareliKJCyP))

# Inter-Rater Reliability

df_interreliKJCy=df_reliKJCy.stack(level=0)
df_interreliKJCy=df_interreliKJCy.unstack(level=0)
df_interreliKJCyP=df_interreliKJCy.P
df_interreliKJCyP=df_interreliKJCyP.unstack(level=1)
df_interreliP.KJC_y_cm=reliability(np.array(df_interreliKJCyP))

## Reliability Z
```

```
df_reliKJCz=df_KJCreli[['Lisa_z','Celi_z','Mike_z','Nick_z']]
df_reliKJCz.columns=['Lisa','Celi','Mike','Nick']

# Intra-Rater Reliability

df_intrareliKJCz=df_reliKJCz.stack(level=0)
df_intrareliKJCz=df_intrareliKJCz.unstack(level=0)
df_intrareliKJCzP=df_intrareliKJCz.P
df_intrareliKJCzP=df_intrareliKJCzP.unstack(level=0)
df_intrareliP.KJC_z_cm=reliability(np.array(df_intrareliKJCzP))

# Inter-Rater Reliability

df_interreliKJCz=df_reliKJCz.stack(level=0)
df_interreliKJCz=df_interreliKJCz.unstack(level=0)
df_interreliKJCzP=df_interreliKJCz.P
df_interreliKJCzP=df_interreliKJCzP.unstack(level=1)
df_interreliP.KJC_z_cm=reliability(np.array(df_interreliKJCzP))

## Validity x,y,z

df_valid.KJC_x_cm=validity(np.array(df_KJCvalid.xP),np.array(df_KJCvalid.xS))
df_valid.KJC_y_cm=validity(np.array(df_KJCvalid.yP),np.array(df_KJCvalid.yS))
df_valid.KJC_z_cm=validity(np.array(df_KJCvalid.zP),np.array(df_KJCvalid.zS))

print(df_valid)
# print(df_interreliP)
# print(df_intrareliP)

### CSA

concat_CSA=np.concatenate((CrossSurfArea[0,:,:],CrossSurfArea[1,:,:],CrossSurfArea[2,:,:
],CrossSurfArea[3,:,:]), axis=1)

rowtrial=6*('1','2','3')
rowpart=2*(3*('B',)+3*('La',)+3*('Lu',))
rowdev=9*('P',)+9*('S',)
rowmultiInd=[np.array(rowdev),np.array(rowpart),np.array(rowtrial)]

limbcol=4*(15*('Shank',) + 15*('Thigh',))
subcol=30*('Lisa',) + 30*('Celi',)+30*('Mike',)+30*('Nick',)
sectcol=8*('1','2','3','4','5','6','7','8','9','10','11','12','13','14','15')
colmultiInd=[np.array(subcol),np.array(limbcol),np.array(sectcol)]

df_CSA=pd.DataFrame(data=concat_CSA,index=rowmultiInd,columns=colmultiInd)
df_validCSA=df_CSA.stack(level=0)
```

```
## Shank
df_validCSASh=df_validCSA.Shank
df_validCSASh=df_validCSASh.stack(level=0)
df_validCSASh=df_validCSASh.unstack(level=0)
# print(df_validCSASh)

df_validCSAShP=df_validCSASh.P
df_validCSAShP=df_validCSAShP.unstack(level=3)
df_validCSAShS=df_validCSASh.S
df_validCSAShS=df_validCSAShS.unstack(level=3)
# print(df_validCSAShS[str(1)])

## Thigh
df_validCSATh=df_validCSA.Thigh
df_validCSATh=df_validCSATh.stack(level=0)
df_validCSATh=df_validCSATh.unstack(level=0)

df_validCSAThP=df_validCSATh.P
df_validCSAThP=df_validCSAThP.unstack(level=3)
df_validCSAThS=df_validCSATh.S
df_validCSAThS=df_validCSAThS.unstack(level=3)
# print(df_validCSAThS[str(1)])


## Validity Stats
bias_CSASh=np.zeros((15,6))
bias_CSATh=np.zeros((15,6))

for i in range(1,16):

        practSh=np.array(df_validCSAShP[str(i)])
        critSh=np.array(df_validCSAShS[str(i)])
        statsSh=validity(practSh,critSh)

        practTh=np.array(df_validCSAThP[str(i)])
        critTh=np.array(df_validCSAThS[str(i)])
        statsTh=validity(practTh,critTh)

        for j in range(6):
                bias_CSASh[i-1,j]=statsSh[j]
                bias_CSATh[i-1,j]=statsTh[j]

## Create dataframe from stats
rows=np.array(range(0,100,7))
cols=np.array(['mbias','mbiasLCL','mbiasUCL','relmbias','relmbiasLCL','relmbiasUCL'])
```

```
df_biasCSASh=pd.DataFrame(data=bias_CSASh,index=rows, columns=cols)
df_biasCSATh=pd.DataFrame(data=bias_CSATh,index=rows, columns=cols)
# print(df_biasCSASh)
# print(df_biasCSATh)

# Bland-Altman Plot
data1=np.array(df_validCSASh.P)
data2=np.array(df_validCSASh.S)
bland_altman_plot(data1, data2, 'Shank CSA', '[cm2]')

data1=np.array(df_validCSATh.P)
data2=np.array(df_validCSATh.S)
bland_altman_plot(data1, data2, 'Thigh CSA', '[cm2]')

###
df_valid=df_valid.T
df_interreliP=df_interreliP.T
df_intrareliP=df_intrareliP.T

writer = pd.ExcelWriter('StatsTable.xlsx')
df_valid.to_excel(writer,'Validity')
df_interreliP.to_excel(writer,'Intra-Rater Reliability')
df_intrareliP.to_excel(writer,'Inter-Rater Reliability')
writer.save()

end = time.time()
print(end - start)
```

6.1.2 importKJCdata.py

```
import pandas as pd
import numpy as np

def importKJCdata():

        folder='/Users/Olivier/3DAnalysisSession1/'
        filename='KJC data - PandaImport.xlsx'
        filepath=folder+filename

        df_out=pd.read_excel(filepath)

        filename='KJC data - PandaImport2.xlsx'
        filepath=folder+filename
        df_KJCreli=pd.read_excel(filepath)

        df_out.set_index('Trial', inplace=True)
```

```
        # Get x values
        df_KJCx=df_out[['Lisa_x','Celi_x','Mike_x','Nick_x']]

        # print(df_KJCx)

        #
df_KJCxP=pd.concat([df_KJCx.Lisa_x['BP1':'LuP3'],df_KJCx.Celi_x['BP1':'LuP3'],df_KJC
x.Mike_x['BP1':'LuP3'],df_KJCx.Nick_x['BP1':'LuP3']]

        df_KJCxS=df_KJCx.Lisa_x['BS1':'LuS3']
        df_KJCxS=df_KJCxS.append(df_KJCx.Celi_x['BS1':'LuS3'])
        df_KJCxS=df_KJCxS.append(df_KJCx.Mike_x['BS1':'LuS3'])
        df_KJCxS=df_KJCxS.append(df_KJCx.Nick_x['BS1':'LuS3'])

        df_KJCxP=df_KJCx.Lisa_x['BP1':'LuP3']
        df_KJCxP=df_KJCxP.append(df_KJCx.Celi_x['BP1':'LuP3'])
        df_KJCxP=df_KJCxP.append(df_KJCx.Mike_x['BP1':'LuP3'])
        df_KJCxP=df_KJCxP.append(df_KJCx.Nick_x['BP1':'LuP3'])

        # print(df_KJCxP)
        # print(df_KJCxS)
        #
df_KJCxS=pd.concat([df_KJCx.Lisa_x['BS1':'LuS3'],df_KJCx.Celi_x['BS1':'LuS3'],df_KJC
x.Mike_x['BS1':'LuS3'],df_KJCx.Nick_x['BS1':'LuS3']])

        # Get y values

        df_KJCy=df_out[['Lisa_y','Celi_y','Mike_y','Nick_y']]

        df_KJCyS=df_KJCy.Lisa_y['BS1':'LuS3']
        df_KJCyS=df_KJCyS.append(df_KJCy.Celi_y['BS1':'LuS3'])
        df_KJCyS=df_KJCyS.append(df_KJCy.Mike_y['BS1':'LuS3'])
        df_KJCyS=df_KJCyS.append(df_KJCy.Nick_y['BS1':'LuS3'])

        df_KJCyP=df_KJCy.Lisa_y['BP1':'LuP3']
        df_KJCyP=df_KJCyP.append(df_KJCy.Celi_y['BP1':'LuP3'])
        df_KJCyP=df_KJCyP.append(df_KJCy.Mike_y['BP1':'LuP3'])
        df_KJCyP=df_KJCyP.append(df_KJCy.Nick_y['BP1':'LuP3'])

        # Get x values

        df_KJCz=df_out[['Lisa_z','Celi_z','Mike_z','Nick_z']]

        df_KJCzS=df_KJCz.Lisa_z['BS1':'LuS3']
```

```
        df_KJCzS=df_KJCzS.append(df_KJCz.Celi_z['BS1':'LuS3'])
        df_KJCzS=df_KJCzS.append(df_KJCz.Mike_z['BS1':'LuS3'])
        df_KJCzS=df_KJCzS.append(df_KJCz.Nick_z['BS1':'LuS3'])

        df_KJCzP=df_KJCz.Lisa_z['BP1':'LuP3']
        df_KJCzP=df_KJCzP.append(df_KJCz.Celi_z['BP1':'LuP3'])
        df_KJCzP=df_KJCzP.append(df_KJCz.Mike_z['BP1':'LuP3'])
        df_KJCzP=df_KJCzP.append(df_KJCz.Nick_z['BP1':'LuP3'])


        # write to a DataFrame for all validity values
        dict_valid={'xP':np.array(df_KJCxP),'xS':np.array(df_KJCxS),'yP':np.array(df_KJCy
P),'yS':np.array(df_KJCyS),'zP':np.array(df_KJCzP),'zS':np.array(df_KJCzS)}

        # df_valid=pd.concat([df_KJCxP,df_KJCxS],axis=1,ignore_index=True)

        df_valid=pd.DataFrame(dict_valid)

        # print(df_valid)
#       print(df_valid.xP)
#       print(df_valid.xS)

        return df_valid, df_KJCreli
```

6.2 Smartphone camera scanning procedure step-by-step

1. Stand in an area with even lighting and no shade (diffused lighting).
    a. Find a location on the ceiling that is symmetrically located between lights.
2. The participant should stand with one leg forward, in a semi-lunge position, with the foot on a white piece of A4 paper. The leg that will be scanned is the forward leg.
3. Flex the forward leg to have a 90º ankle angle and approximately 50-degree knee angle. The shank should be perpendicular to the ground.
4. The participant should remain completely still until scanning is complete. If any movement from the participant or in the background occurs, the scan may not be successful.
5. The scanner should start in a crouched position aiming the phone's camera on the left of the knee joint (medial for the right limb and lateral for the left limb). The camera should be set to capture in portrait view. This allows capturing the whole leg in the picture including the A4 paper. The leg should be taking as much space as possible in the camera view.

6. Start recording and wait 3 seconds. This will capture the left view of the leg.
7. Slowly stand up keeping the whole leg in the video and wait 1 second
8. Walk slowly around the leg until you reach the front view. Wait 1 second.
9. Crouch down to capture a perpendicular view of the front leg. Wait 3 seconds while capturing this front view.
10. Still in the same recording, repeat steps 7-10 for the right view, back view and a second left view.
11. The video recording should be 1-1.5 minutes in length. If the video is less than 1 minute the mesh reconstruction may fail due to insufficient and blurred video frames. Blurry frames occur when the motion is too fast/jerky. It is better to take a longer video with better image quality than a faster video with too much motion blur.

6.3 Mesh Processing step-by-step

1) Import 360 video into a "video to JPG converter" software and extract 100 images
2) Open Autodesk Recap and click "create new model"
3) Click "add photos" and open all images obtained in step 1
4) Click "create model". Keep all settings to default values
5) The images will be uploaded to the Autodesk Recap servers where the 3D reconstruction will occur. An email notification will be sent to the account email once the reconstruction is complete and ready to be downloaded
6) Once the reconstruction is complete click on the download button of the new file at the bottom of the Autodesk Recap window
7) Open the downloaded file to see the full 3D mesh generated.
8) Visually inspect the model with the drag, zoom and rotate tools to ensure no significant deformations are present (i.e:
9) Use the orbit and zoom view tools to visually inspect for mesh imperfections i.e: holes, bumps and surface deformations.
10) Crop the mesh to the geometry of interest: the A4 paper, the foot and as much of the test leg as possible.
    a. This can be done with five plane cuts: one plane cut for each side of the A4 paper and one plane cut at the top of the thigh.

b. The exact location of the thigh's plane cut is visually perpendicular to the thigh axis and immediately distal to where the femur inserts on the pelvis.

11) Scale the mesh with the A4 paper as reference.
    a. Measure the longest side of the A4 paper was and then apply the appropriate scaling factor using the scaling tool.
    b. After scaling, measure both sides of the A4 paper to verify that the scale is now correct (Figure 6).
12) Once the mesh is properly scaled export it as an OBJ (quads) mesh and append "mesh1" to the file name.
13) Working on the same Autodesk file crop the mesh once more with a plane cut parallel to the ground and located above the medial malleoli at the smallest circumference of the shank. This removes the foot and A4 paper from the mesh.
14) Export this new mesh as an OBJ (quads) and append "mesh2" to the name
15) Import "mesh2" into the software Blender and create a duplicate for the following steps.
    a. To reduce noise apply a laplacian smoothing modifier with the following parameters (Repeat=20, Factor=1, Border=1). The resulting mesh should have a smooth surface (Factor=1) and borders that curve inwards (Border=1). If this step mesh is not done prior to designing, then computational issues occur in future operations (i.e.: mesh conversions and the thickening) which cause software crashes.
16) Export to smoothed mesh as an OBJ file and append "mesh3" to the file name.
17) It is important that mesh1, mesh2 and mesh3 are saved as OBJ files since this file type can be converted into T-Spline bodies in Fusion 360. Once these three meshes are saved the Fusion 360 step-by-step guide can be started

6.4 Fusion 360 step-by-step

1) Create A4 paper representing sketch (sketch1)
    a. Create top plane sketch.
    b. Draw rectangle with A4 paper dimension
    c. Exit sketch
2) Import mesh with A4 paper (mesh1)

    a. Ensure scale is appropriate by comparing with sketch1
3) Align mesh1 so that the A4 is parallel to the top plane and the top plane cuts through at the shortest circumference above the medial malleolus
4) Import mesh without A4 paper (mesh3)
    a. Ensure scale is same as mesh1
    b. Align mesh2 with mesh1
5) Convert mesh3 from quads to T-spline (T1)
6) Create leg cast
    a. Thicken T-Spline surface T1 to create a T-spline body
        i. Settings
            1. round
            2. 5mm inwards
            3. 8mm outwards
            4. total = 13mm ~ 0.5in
    b. Convert T-spline body to B-rep body (B1)
7) Determine center of rotation
    a. Create sagittal sketch
    b. Draw 2-lines representing the leg in 2D (sagittal view)
    c. 1 line approximates the main axis of the thigh
    d. 1 line approximates the main axis of the shank
    e. where the 2 lines connect is the approximated center of rotation of the knee
    f. position is determined manually/visually
8) Import hinges and align with center of rotation and knee angle
9) Cut out the knee brace cuffs from the leg cast
    a. Create side sketch
    b. Draw side view template of knee brace
        i. From sagittal view, brace side bars end 2-3 inches away orthogonally from hinges
        ii. Round the open corners of the brace
    c. Extrude cut knee brace sketch from leg cast
10) Fillet edges of brace cuffs

    a. 5mm radius
11) Connect hinges to knee brace cuffs
    a. Loft faces of side bars to the corresponding hinges connection
12) Extrude cut slots for straps
13) Extrude cut EMG sensor locations
    a. Follow SENIAM guide
14) Fillet all remaining sharp edges
15) Export to STL
16) 3D print
    a. 4 mm top/bottom thickness
    b. 4 mm shell thickness
    c. Gradual infill steps

7 References

[1] K. G. Shea, R. Pfeiffer, J. H. Wang, M. Curtin, and P. J. Apel, "Anterior Cruciate Ligament Injury in Pediatric and Adolescent Soccer Players : An Analysis of Insurance Data," *J. Pediatr. Orthop.*, vol. 24, no. 6, pp. 623–628, 2004.

[2] "ACL injuries in young female athletes now an epidemic | Orthopaedics | Loyola Medicine." [Online]. Available: https://www.loyolamedicine.org/news/acl-injuries-young-female-athletes-now-epidemic-04302014. [Accessed: 14-May-2017].

[3] Q. A. Louw, J. Manilall, and K. A. Grimmer, "Epidemiology of knee injuries among adolescents: a systematic review.," *Br. J. Sports Med.*, vol. 42, no. 1, pp. 2–10, Jan. 2008.

[4] P. A. Harmer, "Basketball injuries.," *Med. Sport Sci.*, vol. 49, pp. 31–61, 2005.

[5] S. Colby, A. Francisco, B. Yu, D. Kirkendall, M. Finch, and W. Garrett, "Electromyographic and Kinematic Analysis of Cutting Maneuvers Implications for Anterior Cruciate Ligament Injury."

[6] B. E. Oiestad, I. Holm, L. Engebretsen, and M. A. Risberg, "The association between radiographic knee osteoarthritis and knee symptoms, function and quality of life 10-15 years after anterior cruciate ligament reconstruction.," *Br. J. Sports Med.*, vol. 45, no. 7, pp. 583–8, Jun. 2011.

[7] H. Roos, T. Adalberth, L. Dahlberg, and L. S. Lohmander, "Osteoarthritis of the knee after injury to the anterior cruciate ligament or meniscus: the influence of time and age," *Osteoarthr. Cartil.*, vol. 3, no. 4, pp. 261–267, Dec. 1995.

[8] L. S. Lohmander, A. Östenberg, M. Englund, and H. Roos, "High prevalence of knee osteoarthritis, pain, and functional limitations in female soccer players twelve years after anterior cruciate ligament injury," *Arthritis Rheum.*, vol. 50, no. 10, pp. 3145–3152, Oct. 2004.

[9] L. S. Lohmander, P. M. Englund, L. L. Dahl, and E. M. Roos, "The Long-term Consequence of Anterior Cruciate Ligament and Meniscus Injuries," *Am. J. Sports Med.*, vol. 35, no. 10, pp. 1756–1769, Oct. 2007.

[10] M. V. Paterno, L. C. Schmitt, K. R. Ford, M. J. Rauh, G. D. Myer, B. Huang, and T. E. Hewett, "Biomechanical Measures during Landing and Postural Stability Predict

Second Anterior Cruciate Ligament Injury after Anterior Cruciate Ligament Reconstruction and Return to Sport," *Am. J. Sports Med.*, vol. 38, no. 10, pp. 1968–1978, Oct. 2010.

[11] M. Goddard, L. Salmon, A. Waller, E. Papapetros, and L. A. Pinczewski, "Incidence of graft rupture 15 years after bilateral anterior cruciate ligament reconstructions," *Bone Joint J.*, vol. 95–B, no. 6, pp. 798–802, Jun. 2013.

[12] T. Leys, L. Salmon, A. Waller, J. Linklater, and L. Pinczewski, "Clinical Results and Risk Factors for Reinjury 15 Years After Anterior Cruciate Ligament Reconstruction," *Am. J. Sports Med.*, vol. 40, no. 3, pp. 595–605, Mar. 2012.

[13] E. Laboute, L. Savalli, P. Puig, P. Trouve, G. Sabot, G. Monnier, and B. Dubroca, "Analysis of return to competition and repeat rupture for 298 anterior cruciate ligament reconstructions with patellar or hamstring tendon autograft in sportspeople," *Ann. Phys. Rehabil. Med.*, vol. 53, no. 10, pp. 598–614, Dec. 2010.

[14] H. Grindem, L. Snyder-Mackler, H. Moksnes, L. Engebretsen, and M. A. Risberg, "Simple decision rules can reduce reinjury risk by 84% after ACL reconstruction: the Delaware-Oslo ACL cohort study," *Br. J. Sports Med.*, May 2016.

[15] L. C. Decoster and J. C. Vailas, "Functional anterior cruciate ligament bracing: a survey of current brace prescription patterns.," *Orthopedics*, vol. 26, no. 7, p. 701–6; discussion 706, 2003.

[16] D. Théoret and M. Lamontagne, "Study on three-dimensional kinematics and electromyography of ACL deficient knee participants wearing a functional knee brace during running," *Knee Surgery, Sport. Traumatol. Arthrosc.*, vol. 14, no. 6, pp. 555–563, 2006.

[17] M. A. Risberg, "The Effect of Knee Bracing After Anterior Cruciate Ligament Reconstruction," *Am. J. Sports Med.*, vol. 27, no. 1, 1999.

[18] E. M. Wojtys, S. U. Kothari, and L. J. Huston, "Anterior cruciate ligament functional brace use in sports.," *Am. J. Sports Med.*, 1994.

[19] J. Styf, "The effects of functional knee bracing on muscle function and performance," *Sport. Med.*, vol. 28, no. 2, pp. 77–81, 1999.

[20] M. Jalali, F. Farahmand, T. Rezaeian, D. K. Ramsey, and S. M. E. Mousavi, "Electromyographic analysis of anterior cruciate deficient knees with and without

functional bracing during lunge exercise," *Prosthet. Orthot. Int.*, vol. 40, no. 2, pp. 270–276, Apr. 2016.

[21] H. Hart, N. Collins, D. Ackland, and K. Crossley, "Individuals with osteoarthritis after ACL reconstruction experience immediate improvements in knee pain and confidence with an unloader knee brace," *J. Sci. Med. Sport*, vol. 15, p. S355, Dec. 2012.

[22] E. M. Wojtys, S. U. Kothari, and L. J. Huston, "Anterior Cruciate Ligament Functional Brace Use in Sports*."

[23] P. J. Mcnair, S. N. Stanley, and G. R. Strauss, "Knee Bracing: Effects on Proprioception," 1996.

[24] K. E. Wilk, L. C. Macrina, and C. Arrigo, "Shoulder Rehabilitation," 2012.

[25] "Custom Knee Brace Cost." [Online]. Available: https://www.orthomed.ca/store/knee-braces?type=113&gclid=CjwKCAjw06LZBRBNEiwA2vgMVfhBTyUvjozBBMiKhQKEE8KePnk6UzbI2A7j0nERB6crROEEhfn2ZhoCOcUQAvD_BwE. [Accessed: 19-Jun-2018].

[26] A. E. Rankin, "A Survey of Functional Knee Brace Usage Following Anterior Cruciate Ligament Reconstruction -A Pilot Study," University of Western Ontario, 1997.

[27] How It's Made Show, "How Its Made Custom Knee Braces," 2016. [Online]. Available: https://www.youtube.com/watch?v=o-any6WJNPg. [Accessed: 07-Aug-2018].

[28] D. Mourtzis and M. Doukas, "Decentralized Manufacturing Systems Review: Challenges and Outlook," Springer, Berlin, Heidelberg, 2013, pp. 355–369.

[29] P. Garrehy, "Centralized vs Decentralized Manufacturing," *Industry Today*, 2014.

[30] J.-C. Andre, A. Le Mehaute, and O. De Witte, "Fr 2567668." p. 15, 1984.

[31] Total 3D Printing, "How Much Do 3D Printers Cost? - Price Ranges and Categories," 2017. [Online]. Available: https://total3dprinting.org/much-3d-printers-cost-price-ranges-categories/. [Accessed: 07-Aug-2018].

[32] Ultimaker, "Ultimaker S5 specifications," 2018. [Online]. Available: https://ultimaker.com/en/products/ultimaker-s5/specifications. [Accessed: 20-Jul-2018].

[33] R. K. Chen, Y.-A. Jin, J. Wensman, and A. Shih, "Additive manufacturing of custom orthoses and prostheses—A review," *Addit. Manuf.*, vol. 12, pp. 77–89, 2016.

[34] Nia Technologies, “Nia Technologies.” [Online]. Available: https://niatech.org/. [Accessed: 07-Aug-2018].

[35] “Enabling The Future – A Global Network Of Passionate Volunteers Using 3D Printing To Give The World A "Helping Hand."” [Online]. Available: http://enablingthefuture.org/. [Accessed: 16-Jul-2018].

[36] C.-W. Tan, F. Coutts, and C. Bulley, “Measurement of lower limb volume: Agreement between the vertically oriented perometer and a tape measure method,” *Physiotherapy*, vol. 99, pp. 247–251, 2013.

[37] Enabling The Future, “e-NABLE DEVICE SIZING,” 2018. [Online]. Available: http://enablingthefuture.org/resources-2/e-nable-device-sizing/. [Accessed: 07-Aug-2018].

[38] Y. Dessery and J. Pallari, “Measurements agreement between low-cost and high-level handheld 3D scanners to scan the knee for designing a 3D printed knee brace.,” *PLoS One*, vol. 13, no. 1, p. e0190585, 2018.

[39] E. Seminati, D. C. Talamas, M. Young, M. Twiste, V. Dhokia, and J. L. J. Bilzon, “Validity and reliability of a novel 3D scanner for assessment of the shape and volume of amputees’ residual limb models.”

[40] G. E. Armin and E. Armin Gruen, “Digital Photogrammetric Imaging Past Present Digital Photogrammetric Imaging-Past, Present and Future.”

[41] O. CTI, “How to measure for a CTi?” [Online]. Available: https://www.ctikneebraces.co.uk/guide-to-cti/how-to-measure.html. [Accessed: 13-Sep-2018].

[42] Ossur, “Ossur OA Unloader One,” 2013.

[43] New Options Sports, “Fitting Chart.” [Online]. Available: http://www.newoptionssports.com/Fitting-Chart.html. [Accessed: 13-Sep-2018].

[44] I. Breg, “Fusion® Knee Brace.” [Online]. Available: https://www.breg.com/products/knee-bracing/functional-ligament/fusion-knee-brace/. [Accessed: 13-Sep-2018].

[45] P. S. Walker, J. S. Rovick, and D. D. Robertson, “The effects of knee brace hinge design and placement on joint mechanics,” *J. Biomech.*, vol. 21, pp. 965–974, 1988.

[46] F. H. Gunston, “Polycentric Knee Arthroplasty,” *Bone Jt.*, vol. 53–B, no. 2, pp. 272–

277, 1971.

[47] R. M. Lazaro and K. L. Dec, *25 – Knee Orthoses for Sports-Related Issues*, Fifth Edit. Elsevier Inc., 2019.

[48] L. G. Hallén and O. Lindahl, "The Screw-Home Movement in the Knee-Joint," *Acta Orthop. Scand.*, vol. 37, no. 1, pp. 97–106, 2009.

[49] K. Rajendran, "Mechanism of locking at the knee joint.," *J. Anat.*, vol. 143, pp. 189–94, Dec. 1985.

[50] R. F. Escamilla, "Knee biomechanics of the dynamic squat exercise," *Med. Sci. Sports Exerc.*, vol. 33, no. 1, pp. 127–141, 2001.

[51] B. RR, "Knee Braces," in *The Hughston Clinic Sport Medicine Book*, B. CL, F. F, and H. JM, Eds. Baltimore: Williams & Wilkins, 1995, pp. 551–558.

[52] M. J. Salata, A. E. Gibbs, and J. K. Sekiya, "The effectiveness of prophylactic knee bracing in american football: a systematic review.," *Sports Health*, vol. 2, no. 5, pp. 375–9, Sep. 2010.

[53] E. P. France and L. E. Paulos, "In vitro assessment of prophylactic knee brace function.," *Clin. Sports Med.*, vol. 9, no. 4, pp. 823–41, Oct. 1990.

[54] J. C. Vailas and M. Pink, "Biomechanical Effects of Functional Knee Bracing," *Sport. Med.*, vol. 15, no. 3, pp. 210–218, Mar. 1993.

[55] T. P. Branch and R. E. Hunter, "Functional analysis of anterior cruciate ligament braces.," *Clin. Sports Med.*, vol. 9, no. 4, pp. 771–97, Oct. 1990.

[56] P. W. Cawley, E. Paul France, and L. E. Paulos, "The current state of functional knee bracing research A review of the literature."

[57] N. Rishiraj, J. E. Taunton, R. Lloyd-Smith, R. Woollard, W. Regan, and D. B. Clement, "The Potential Role of Prophylactic/Functional Knee Bracing in Preventing Knee Ligament Injury," *Sport. Med.*, vol. 39, no. 11, pp. 937–960, Nov. 2009.

[58] S. H. Liu and R. Mirzayan, "Current review. Functional knee bracing.," *Clin. Orthop. Relat. Res.*, no. 317, pp. 273–81, Aug. 1995.

[59] France and Paulos, "Knee Bracing.," *J. Am. Acad. Orthop. Surg.*, vol. 2, no. 5, pp. 281–287, Oct. 1994.

[60] S. A. Paluska and D. B. McKeag, "Knee braces: current evidence and clinical recommendations for their use.," *Am. Fam. Physician*, vol. 61, no. 2, pp. 411–8, 423–

4, Jan. 2000.

[61] “Knee Braces – Breg, Inc.” [Online]. Available: https://www.breg.com/products/knee-bracing/. [Accessed: 16-Jul-2018].

[62] “DonJoy Products.” [Online]. Available: https://www.djoglobal.com/products/brand?f%5B0%5D=im_field_brand%3A10&f%5B1%5D=im_field_anatomy%3A51. [Accessed: 16-Jul-2018].

[63] E. L. Castillo, J. D. Castillo, and M. S. Castillo, “Knee brace with cammed stop lever,” US4886054A, 1989.

[64] E. S. Grood, D. L. Butler, D. M. Ledyard, and S. D. Hoffman, “Knee brace,” US5018514A, 1991.

[65] J. K. Rasmusson, “Knee brace,” US5060640A, 1991.

[66] D. P. Harris, M. E. Berkeley, and W. L. McCune, “Floating pivot hinge and knee brace,” US5074290A, 1990.

[67] “Products | Osskin.” [Online]. Available: http://www.osskin.com/index.php/products/. [Accessed: 16-Jul-2018].

[68] M. P. Greene, “Four Bar Linkage Knee Analysis.”

[69] R. Shenoy, P. Pastides, and D. Nathwani, “(iii) Biomechanics of the knee and TKR,” 2013.

[70] Fong S. Yang, “Knee brace,” US20180021160A1, 2016.

[71] Brett Owen Bledsoe, “Orthopedic knee brace with dynamically changing medial and lateral hinges,” US20120271211A1, 2012.

[72] A. Bosshard and S. Kohl, “Knee brace for supporting a knee joint,” EP2959868B1, 2014.

[73] B. D. Beynnon, M. H. Pope, C. M. Wertheimer, R. J. Johnson, B. C. Fleming, C. E. Nichols, and J. G. Howe, “The effect of functional knee-braces on strain on the anterior cruciate ligament in vivo,” *J. Bone Jt. Surg.*, vol. 74A, no. 9, pp. 1298–1312, Oct. 1992.

[74] C. A. Soma, P. W. Cawley, S. Liu, and C. T. Vangsness, “Custom-Fit Versus Premanufactured Braces,” 2004.

[75] E. M. Wojtys and L. J. Huston, “Custom-fit versus off-the-shelf ACL functional braces.,” *Am. J. Knee Surg.*, vol. 14, no. 3, pp. 157–62, 2001.

[76] G. M. Berke, J. Fergason, J. R. Milani, J. Hattingh, M. McDowell, V. Nguyen, and G.

E. Reiber, “Comparison of satisfaction with current prosthetic care in veterans and servicemembers from Vietnam and OIF/OEF conflicts with major traumatic limb loss,” *J. Rehabil. Res. Dev.*, vol. 47, no. 4, pp. 361–372, 2010.

[77] R. Gailey, K. Allen, J. Castles, J. Kucharik, and M. Roeder, “Review of secondary physical conditions associated with lower-limb amputation and long-term prosthesis use,” vol. 45, no. 1, 2008.

[78] S. Santos, B. Soares, M. Leite, and J. Jacinto, “Design and development of a customised knee positioning orthosis using low cost 3D printers,” *Virtual Phys. Prototyp.*, vol. 12, pp. 322–332, 2017.

[79] S. Steiner, “אור שטיינר| סד לרגל - פרויקט גמר.” [Online]. Available: http://orsteiner-splintkafo.blogspot.com/. [Accessed: 29-Jul-2018].

[80] fcubed, “Modular Knee Brace - Thingiverse,” 2016. [Online]. Available: https://www.thingiverse.com/thing:1509833. [Accessed: 24-Jun-2018].

[81] “3D Printed PEEK Bionic Knee Brace | INTAMSYS.” [Online]. Available: https://www.intamsys.com/case-study-bioneek/. [Accessed: 09-Jul-2018].

[82] “Osskin | The World’s First 3D Printed Custom Knee Brace.” [Online]. Available: http://www.osskin.com/. [Accessed: 09-Jul-2018].

[83] J. Saleh and K. Dalgarno, “Cost and benefit analysis of fused deposition modelling (FDM) technique and selective laser sintering (SLS) for fabrication of customised foot orthoses,” *Proc. 4th Int. Conf. Adv. Res. Virtual Rapid Manuf., …*, pp. 705–710, 2009.

[84] J. H. P. Pallari, K. W. Dalgarno, and J. Woodburn, “Mass customization of foot orthoses for rheumatoid arthritis using selective laser sintering,” *IEEE Trans. Biomed. Eng.*, vol. 57, no. 7, pp. 1750–1756, Jul. 2010.

[85] A. S. Salles and D. E. Gyi, “Delivering personalised insoles to the high street using additive manufacturing.”

[86] A. S. Salles and D. E. Gyi, “An evaluation of personalised insoles developed using additive manufacturing.”

[87] C. E. Dombroski, M. E. R. Balsdon, and A. Froats, “The use of a low cost 3D scanning and printing tool in the manufacture of custom-made foot orthoses: a preliminary study,” *BMC Res. Notes*, 2014.

[88] R. Chen, L. Chen, B. Tai, Y. Wang, A. Shih, and J. Wensman, “Additive manufacturing

of personalized ankle-foot orthosis," *Proc. NAMRI/SME*, vol. 42, no. April 2017, pp. 381–389, 2014.

[89] M. Alam, I. Ahmed Choudhury, A. Bin Mamat, and S. Hussain, "Computer Aided Design and Fabrication of a Custom Articulated Ankle Foot Orthosis," *J. Mech. Med. Biol.*, vol. 15, no. 4, 2015.

[90] F. Gao, W. Carlton, and S. Kapp, "Effects of joint alignment and type on mechanical properties of thermoplastic articulated ankle-foot orthosis," *Prosthet. Orthot. Int.*, vol. 35, no. 2, pp. 181–189, Jun. 2011.

[91] W. E. Rogers, R. H. Crawford, J. J. Beaman, and N. E. Walsh, "Fabrication of prosthetic sockets by selective laser sintering," in *Solid Freeform Fabrication Symposium Proceedings*, 1991, p. Volume 6, Pages 158-163.

[92] J. C. H. Goh, P. V. S. Lee, and P. Ng, "Structural integrity of polypropylene prosthetic sockets manufactured using the polymer deposition technique," *Proc. Inst. Mech. Eng. Part H J. Eng. Med.*, vol. 216, no. 6, pp. 359–368, Jun. 2002.

[93] B. Rogers, A. Gitter, G. Bosker, M. Faustini, M. Lokhande, and R. Crawford, "Clinical evaluation of prosthetic sockets manufactured by selective laser sintering," *2001 Solid Free. Fabr. Symp. Proc.*, no. March 2015, pp. 505–512, 2001.

[94] J. Y. H. Fuh, W. Feng, and Y. S. Wong, "Modelling, Analysis and Fabrication of Below-knee Prosthetic Sockets Using Rapid Prototyping," in *Advanced Manufacturing Technology for Medical Applications*, Chichester, UK: John Wiley & Sons, Ltd, 2006, pp. 207–226.

[95] F. E. H. Tay, M. A. Manna, and L. X. Liu, "Case study A CASD/CASM method for prosthetic socket fabrication using the FDM technology."

[96] N. Herbert, D. Simpson, W. D. Spence, and W. Ion, "A preliminary investigation into the development of 3-D printing of prosthetic sockets," *J. Rehabil. Res. Dev.*, vol. 42, no. 2, p. 141, 2005.

[97] D. Freeman and L. Wontorcik, "Stereolithography and prosthetic test socket manufacture: a cost/benefit analysis," *J. Prosthetics Orthot.*, vol. 10, no. 1, pp. 17–20, 1998.

[98] B. Rogers, S. Stephens, A. Gitter, G. Bosker, and R. Crawford, "Double-wall, transtibial prosthetic socket fabricated using selective laser sintering: a case study," *J.*

Prosthetics Orthot., vol. 12, no. 3, pp. 97–103, 2000.

[99] M. C. Faustini, R. R. Neptune, R. H. Crawford, W. E. Rogers, and G. Bosker, "An experimental and theoretical framework for manufacturing prosthetic sockets for transtibial amputees," *IEEE Trans. Neural Syst. Rehabil. Eng.*, vol. 14, no. 3, pp. 304–310, 2006.

[100] M. C. Faustini, R. H. Crawford, R. R. Neptune, W. E. Rogers, and G. Bosker, "Design and Analysis of Orthogonally Compliant Features for Local Contact Pressure Relief in Transtibial Prostheses," *J. Biomech. Eng.*, vol. 127, no. 6, p. 946, Nov. 2005.

[101] D. M. Sengeh and H. Herr, "A Variable-Impedance Prosthetic Socket for a Transtibial Amputee Designed from Magnetic Resonance Imaging Data."

[102] E. L. Doubrovski, E. Y. Tsai, D. Dikovsky, J. M. P. Geraedts, H. Herr, and N. Oxman, "Voxel-based fabrication through material property mapping: A design method for bitmap printing," *Comput. Des.*, vol. 60, pp. 3–13, 2015.

[103] A. M. Paterson, R. Bibb, R. I. Campbell, and G. Bingham, "Comparing additive manufacturing technologies for customised wrist splints," *Rapid Prototyp. J.*, vol. 21, no. 3, 2015.

[104] J. Evill and O. Evill, "CORTEX - EVILL," 2013. [Online]. Available: http://www.evilldesign.com/cortex. [Accessed: 20-Jul-2018].

[105] "ActivArmor | Custom 3D-Printed Casts and Splints." [Online]. Available: https://activarmor.com/. [Accessed: 20-Jul-2018].

[106] K. Subburaj, C. Nair, S. Rajesh, S. M. Meshram, and B. Ravi, "Rapid development of auricular prosthesis using CAD and rapid prototyping technologies Background information," *J. Oral Maxillofac. Surg*, vol. 36, pp. 938–943, 2007.

[107] P. Liacouras, J. Garnes, N. Roman, P. Anton, and G. Gerald T., "Designing and manufacturing an auricular prosthesis using computed tomography, 3-dimensional photographic imaging, and additive manufacturing: A clinical report," *J. Prosthet. Dent.*, vol. 105, pp. 78–82, 2011.

[108] S. A. Dalley, T. E. Wiste, T. J. Withrow, and M. Goldfarb, "Design of a Multifunctional Anthropomorphic Prosthetic Hand With Extrinsic Actuation," 2009.

[109] H. Atakan, "A Multigrasp Hand Prosthesis for Transradial Amputees," 2010.

[110] J. Zuniga, D. Katsavelis, J. Peck, J. Stollberg, M. Petrykowski, A. Carson, and C.

Fernandez, “Cyborg beast: a low-cost 3d-printed prosthetic hand for children with upper-limb differences,” *BMC Res. Notes*, vol. 8, no. 1, p. 10, Jan. 2015.

[111] B. J. South, N. P. Fey, G. Bosker, and R. R. Neptune, “Manufacture of Energy Storage and Return Prosthetic Feet Using Selective Laser Sintering,” *J. Biomech. Eng.*, vol. 132, no. 1, p. 015001, 2010.

[112] J. D. Ventura, G. K. Klute, and R. R. Neptune, “The effects of prosthetic ankle dorsiflexion and energy return on below-knee amputee leg loading,” *JCLB*, vol. 26, pp. 298–303, 2011.

[113] “Infill | Professional 3D printing made accessible | Ultimaker.” [Online]. Available: https://ultimaker.com/en/resources/20416-infill. [Accessed: 14-Jul-2018].

[114] Ultimaker, “Ultimaker 3: Unrivaled print quality.” [Online]. Available: https://ultimaker.com/en/products/ultimaker-3. [Accessed: 20-Jul-2018].

[115] P. Cain, “Selecting the optimal shell and infill parameters for FDM 3D Printing | 3D Hubs.” [Online]. Available: https://www.3dhubs.com/knowledge-base/selecting-optimal-shell-and-infill-parameters-fdm-3d-printing. [Accessed: 14-Jul-2018].

[116] A. B. Varotsis, “Introduction to SLA 3D Printing | 3D Hubs.” [Online]. Available: https://www.3dhubs.com/knowledge-base/introduction-sla-3d-printing. [Accessed: 20-Jul-2018].

[117] A. B. Varotsis, “Introduction to Metal 3D printing | 3D Hubs.” [Online]. Available: https://www.3dhubs.com/knowledge-base/introduction-metal-3d-printing. [Accessed: 20-Jul-2018].

[118] GE Additive, “What is Additive Manufacturing? | GE Additive.” [Online]. Available: https://www.ge.com/additive/additive-manufacturing. [Accessed: 20-Jul-2018].

[119] Wikipedians, “3D Printing,” *Wikipedia*. .

[120] C. Smyth, “Infill and Strength: Functional Design Doesn’t Stop at the CAD Desk | 3D Printing for Beginners.” [Online]. Available: http://3dprintingforbeginners.com/infill-strength/. [Accessed: 13-Jul-2018].

[121] R. G. Budynas and J. K. Nisbett, *Shigley’s Mechanical Engineering Design*, 9th ed. New York, NY: McGraw-Hill, 2011.

[122] Innofil3D, “Technical Data Sheet. ABS by Innofil3D BV.” Innofil3D, 2016.

[123] S. Hermann, “(9) INFILL pattern and SHELLS - How to get the maximum

STRENGTH out of your 3D prints? - YouTube." [Online]. Available: https://www.youtube.com/watch?v=AmEaNAwFSfI. [Accessed: 14-Jul-2018].

[124] K. Álvarez, R. F. Lagos, and M. Aizpun, "Investigating the influence of infill percentage on the mechanical properties of fused deposition modelled ABS parts," *Ing. e Investig.*, vol. 36, no. 3, p. 110, Dec. 2016.

[125] M. Fernandez-Vicente, W. Calle, S. Ferrandiz, and A. Conejero, "Effect of Infill Parameters on Tensile Mechanical Behavior in Desktop 3D Printing," *3D Print. Addit. Manuf.*, vol. 3, no. 3, pp. 183–192, Sep. 2016.

[126] M. Zens, M. J. Feucht, J. Ruhhammer, A. Bernstein, H. O. Mayr, N. P. Südkamp, P. Woias, and P. Niemeyer, "Mechanical tensile properties of the anterolateral ligament.," *J. Exp. Orthop.*, vol. 2, no. 1, p. 7, Dec. 2015.

[127] T. Spahiu and E. Piperi, "Extracting body dimensions from 3D body scanning," in *6th International Conference of Textile*, 2014, no. November.

[128] L. Jaeschke, A. Steinbrecher, and T. Pischon, "Measurement of Waist and Hip Circumference with a Body Surface Scanner: Feasibility, Validity, Reliability, and Correlations with Markers of the Metabolic Syndrome," *PLoS One*, vol. 10, no. 3, p. e0119430, Mar. 2015.

[129] R. E. Sims, R. Marshall, D. E. Gyi, S. J. Summerskill, and K. Case, "Collection of anthropometry from older and physically impaired persons: Traditional methods versus TC2 3-D body scanner," *Int. J. Ind. Ergon.*, vol. 42, no. 1, pp. 65–72, Jan. 2012.

[130] Z. Taha, MohdAzriAris, Zulkifli Ahmad, MohdHasnunArif Hassan, and Nina Nadia Sahim, "A Low Cost 3D Foot Scanner for Custom-Made Sport," *Appl. Mech. Mater.*, vol. 440, pp. 369–372, 2014.

[131] J. Rosicky, A. Grygar, P. Chapcak, T. Bouma, and J. Rosicky, "Application of 3D Scanning in Prosthetic & Orthotic Clinical Practice."

[132] S. Yamamoto, H. Miyachi, H. Fujii, S. Ochiai, S. Watanabe, and K. Shimozato, "Intuitive Facial Imaging Method for Evaluation of Postoperative Swelling: A Combination of 3-Dimensional Computed Tomography and Laser Surface Scanning in Orthognathic Surgery," *J. Oral Maxillofac. Surg.*, vol. 74, p. 2506.e1-2506.e10, 2016.

[133] C. E. Coltman, D. E. Mcghee, and J. R. Steele, "Three-dimensional scanning in women with large, ptotic breasts: implications for bra cup sizing and design," *Ergonomics*, vol.

60, no. 3, pp. 439–445, 2016.

[134] A. Modabber, F. Peters, K. Kniha, E. Goloborodko, A. Ghassemi, B. Lethaus, F. H. € Olzle, S. Christian, and M. € Ohlhenrich, "Evaluation of the accuracy of a mobile and a stationary system for three-dimensional facial scanning," *J. Cranio-Maxillofacial Surg.*, vol. 44, pp. 1719–1724, 2016.

[135] K. Khoshelham and S. O. Elberink, "Accuracy and Resolution of Kinect Depth Data for Indoor Mapping Applications," *Sensors*, vol. 12, no. 2, pp. 1437–1454, Feb. 2012.

[136] A. Tursi, G. Kurillo, and R. Bajcsy, "Automatic Detection of Body Landmarks in Human Body Scans Lower Limb Analysis for Biomedical and Footwear Applications."

[137] H. Oh and J. Kim, "Patella Shape Extraction from 3D Point Cloud Data for Personalized Knee Brace," Springer, Cham, 2017, pp. 160–168.

[138] T. Stoyanov, R. Mojtahedzadeh, H. Andreasson, and A. J. Lilienthal, "Comparative evaluation of range sensor accuracy for indoor mobile robotics and automated logistics applications," *Rob. Auton. Syst.*, 2012.

[139] K. D. Mankoff and T. A. Russo, "The Kinect: a low-cost, high-resolution, short-range 3D camera," *Earth Surf. Process. Landforms*, vol. 38, no. 9, pp. 926–936, Jul. 2013.

[140] J. Han, L. Shao, D. Xu, and J. Shotton, "Enhanced computer vision with Microsoft Kinect sensor: A review," *IEEE Trans. Cybern.*, vol. 43, no. 5, pp. 1318–1334, 2013.

[141] G. Percoco, "Digital Close Range Photogrammetry for 3D Body Scanning for Custom-Made Garments."

[142] "Scanlab Photogrammetry." [Online]. Available: https://scanlab.ca/. [Accessed: 18-Jun-2018].

[143] N. Summers, "The real-time motion capture behind 'Hellblade,'" 2017. [Online]. Available: https://www.engadget.com/2017/08/08/ninja-theory-hellblade-motion-capture-demo-video/. [Accessed: 18-Jun-2018].

[144] "How we used Photogrammetry to Capture Every Last Detail for Star Wars™ Battlefront™ - Star Wars - Official EA Site," 2015. [Online]. Available: http://starwars.ea.com/starwars/battlefront/news/how-we-used-photogrammetry. [Accessed: 18-Jun-2018].

[145] C. Goulding, "3D Printed Props Revolutionize the Film Industry Landscape | 3DPrint.com | The Voice of 3D Printing / Additive Manufacturing." [Online].

Available: https://3dprint.com/185871/3d-printed-props/. [Accessed: 20-Jul-2018].

[146] "Legacy Effects." [Online]. Available: http://www.legacyefx.com/. [Accessed: 20-Jul-2018].

[147] Weta Workshop, "Weta Workshop - conceptual design and physical manufacturing for creative industries » Weta Workshop." [Online]. Available: https://www.wetaworkshop.com/. [Accessed: 20-Jul-2018].

[148] N. Lievendag, "SCANN3D Android Photogrammetry App Review - 3D Scan Expert," 2018. [Online]. Available: https://3dscanexpert.com/scann3d-android-photogrammetry-app-review/. [Accessed: 18-Jun-2018].

[149] Mathworks, "Uncalibrated Stereo Image Rectification - MATLAB & Simulink," 2018. [Online]. Available: https://www.mathworks.com/help/vision/examples/uncalibrated-stereo-image-rectification.html. [Accessed: 18-Jun-2018].

[150] A. Hernandez and E. Lemaire, "A smartphone photogrammetry method for digitizing prosthetic socket interiors," *Prosthet. Orthot. Int.*, vol. 41, no. 2, pp. 210–214, 2017.

[151] Li, Guangkun, Gao, Fan, Wang, and Zhigang, "A Photogrammetry-Based System for 3D Surface Reconstruction of Prosthetics and Orthotics," 2011.

[152] C. Octavian and R. Mariana, "Photogrammetric Scanning and Applications in Medicine."

[153] C. L. Heike, K. Upson, E. Stuhaug, and S. M. Weinberg, "3D digital stereophotogrammetry: a practical guide to facial image acquisition."

[154] V. A. Knyaz and S. Yu Zheltov, "Photogrammetric Techniques for Dentisry Analysis, Planning and Visualisation."

[155] Z. Majid, A. K. Chong, A. Ahmad, H. Setan, and A. R. Samsudin, "Photogrammetry and 3D Laser Scanning as Spatial Data Capture Techniques for a National Craniofacial Database," *Photogramm. Rec.*, vol. 20, no. 109, pp. 48–68, 2005.

[156] N. Lievendag, "Free 3D Scanning from Video by using just a Smartphone - 3D Scan Expert," 2017. [Online]. Available: https://3dscanexpert.com/free-3d-scanning-video-smartphone/. [Accessed: 19-Jun-2018].

[157] L. G. Farkas, W. Bryson, and J. Klotz, "Is photogrammetry of the face reliable?," *Plastic and Reconstructive Surgery*, vol. 66, no. 3. pp. 346–355, 1980.

[158] D. V. Kratky, “Digital Modeling of Limbs in Orthopaedics,” *Photogramm. Eng. Remote Sensing*, vol. 41, no. 6, pp. 741–752, 1974.

[159] R. Tokarczyk and S. Mikrut, “Close Range Photogrammetry System For Medicine and Railways,” *Int. Arch. Photogramm. Remote Sens. Spat. Inf. Sci. - ISPRS Arch.*, vol. 33, no. B5, pp. 519–524, 2000.

[160] G. Baroni, G. Ferrigno, R. Orecchia, and A. Pedotti, “Real-time three-dimensional motion analysis for patient positioning veri®cation,” *Radiother. Oncol.*, vol. 54, no. 1, pp. 21–27, 2000.

[161] J. Fels and S. Fingerhuth, “Anthropometric Data Acquisition using Photogrammetric Techniques to obtain Acoustic Head-Related Transfer Functions of Children,” in *Proceedings of the CTU Conference*, 2004.

[162] B. Blizard, “The Art of Photogrammetry: How To Take Your Photos,” *Tested*, 2014. [Online]. Available: https://www.tested.com/art/makers/460142-art-photogrammetry-how-take-your-photos/. [Accessed: 13-Sep-2018].

[163] Sketchfab Team, “How to set up a successful photogrammetry project,” *Sketchfab Blog*, 2015. [Online]. Available: https://blog.sketchfab.com/how-to-set-up-a-successful-photogrammetry-project/. [Accessed: 13-Sep-2018].

[164] S. Lachambre, S. Lagarde, and C. Jover, “Photogrammetry Workflow,” 2017.

[165] “SENIAM.” [Online]. Available: http://www.seniam.org. [Accessed: 12-May-2017].

[166] E. L. Bukowski, A. Conway, L. A. Glentz, K. Kurland, and M. Lou Galantino, “The Effect of Iyengar Yoga and Strengthening Exercises for People Living With Osteoarthritis of The Knee: A Case Series,” *Int’l. Q. Community Heal. Educ.*, vol. 26, no. 3, pp. 287–305, 2006.

[167] S. L. Kolasinski, M. Garfinkel, A. G. Tsai, W. Matz, A. Van Dyke, and H. R. Schumacher, “Iyengar Yoga for Treating Symptoms of Osteoarthritis of the Knees: A Pilot Study,” *J. Altern. Complement. Med.*, vol. 11, no. 4, pp. 689–693, 2005.

[168] Blender, “Laplacian Smooth Modifier — Blender 2.79 Manual.” [Online]. Available: https://docs.blender.org/manual/en/dev/modeling/modifiers/deform/laplacian_smooth.html. [Accessed: 08-Feb-2018].

[169] 3D-Fuel, “4KG Engineering Pro PLA / APLA+,” *Filaments.ca*. [Online]. Available: https://filaments.ca/products/4kg-engineering-apla-fossil-fuel-black-1-75mm.

[Accessed: 13-Sep-2018].

[170] A. P, "TOP 12 PEEK and ULTEM 3D printers -," *3Dnatives*, 2018. [Online]. Available: https://www.3dnatives.com/en/ranking-3d-printers-peek-ultem020520184/. [Accessed: 13-Sep-2018].

[171] 3D-Fuel, "Advanced PLA 3D Printer Filament," *Workday PLA*. [Online]. Available: https://www.3dfuel.com/materials/workday-pla/. [Accessed: 13-Sep-2018].

[172] C. Klahn, D. Singer, and M. Meboldt, "Design Guidelines for Additive Manufactured Snap-Fit Joints," *Procedia CIRP*, vol. 50, pp. 264–269, Jan. 2016.

[173] G. Robertson, G. Caldwell, J. Hamill, G. Kamen, and S. Whittlesey, *Research methods in biomechanics*. 2004.

[174] "Spreadsheets for analysis of validity and reliability." [Online]. Available: http://sportsci.org/2015/ValidRely.htm. [Accessed: 14-Apr-2018].

[175] W. G. Hopkins, "Measures of Reliability in Sports Medicine and Science."

[176] J. M. Bland and D. G. Altman, "Measuring agreement in method comparison studies," *SM181RA Stat. Methods Med. Res.*, vol. 8, no. 99, pp. 962–2802, 1999.

[177] V. G. de Boer-Wilzing, A. Bolt, J. H. Geertzen, C. H. Emmelot, E. C. Baars, and P. U. Dijkstra, "Variation in Results of Volume Measurements of Stumps of Lower-Limb Amputees: A Comparison of 4 Methods," *Arch. Phys. Med. Rehabil.*, vol. 92, no. 6, pp. 941–946, Jun. 2011.

[178] A. Bolt, V. G. de Boer-Wilzing, J. H. B. Geertzen, C. H. Emmelot, E. C. T. Baars, and P. U. Dijkstra, "Variation in Measurements of Transtibial Stump Model Volume," *Am. J. Phys. Med. Rehabil.*, vol. 89, no. 5, pp. 376–384, May 2010.

[179] T. K. Koo and M. Y. Li, "A Guideline of Selecting and Reporting Intraclass Correlation Coefficients for Reliability Research," *J. Chiropr. Med.*, vol. 15, no. 2, pp. 155–163, 2016.

[180] A. Menditto, M. Patriarca, and B. Magnusson, "Understanding the meaning of accuracy, trueness and precision," *Accredit. Qual. Assur.*, vol. 12, no. 1, pp. 45–47, Jan. 2007.

[181] "Canada Computers: Samsung S5 5.1" 16MP Refurbished Smartphone - RedFlagDeals.com." [Online]. Available: https://www.redflagdeals.com/deal/cell-phones/samsung-s5-5-1-16-mp-refurbished-smartphone/. [Accessed: 13-Sep-2018].

[182] N. Center for Health Statistics, “Anthropometric Reference Data for Children and Adults: United States, 2011–2014,” 2016.

[183] G. D. Myer, D. Sugimoto, S. Thomas, and T. E. Hewett, “The influence of age on the effectiveness of neuromuscular training to reduce anterior cruciate ligament injury in female athletes: a meta-analysis.,” *Am. J. Sports Med.*, vol. 41, no. 1, pp. 203–15, Jan. 2013.

[184] D. A. Santos, J. A. Dawson, C. N. Matias, P. M. Rocha, C. S. Minderico, D. B. Allison, L. B. Sardinha, and A. M. Silva, “Reference values for body composition and anthropometric measurements in athletes.,” *PLoS One*, vol. 9, no. 5, p. e97846, 2014.